Dual Antibody Functionalized Polyvinyl Alcohol and Alginate Hydrogels for Synergistic Endothelial Cell Adhesion

PROFESSOR DEBRA T. AUGUSTE **MARJAN RAFAT**

DUAL ANTIBODY FUNCTIONALIZED POLYVINYL ALCOHOL AND ALGINATE HYDROGELS FOR SYNERGISTIC ENDOTHELIAL CELL ADHESION

ABSTRACT

Motivated by the need to design minimally-invasive treatments for wide-necked cerebral aneurysms, we used computational modeling to assess aneurysm hemodynamics, examined *in vitro* cellular responses arising from mechanical and chemical stresses, and designed novel materials that cooperatively adhere to the endothelium. We first hypothesized that because aneurysm geometry plays an important role in hemodynamics, changes in flow patterns may affect the shear stress experienced on the aneurysm wall. We defined flow regimes based on aneurysm hemodynamic and geometric parameters, which may correlate with aneurysm rupture. Because of the direct contact between endothelial cells (ECs) and blood flow, we then evaluated how changes in hemodynamics and inflammatory cytokines affect the expression of cell adhesion molecules (CAMs) and matrix remodeling factors on ECs. We subsequently designed biomaterials that complement the dynamic EC surface and have the ability to conform to any geometry through *in situ* crosslinking. Antibody-conjugated hydrogels facilitated synergistic EC adhesion using cooperativity as an adhesion strategy. We optimized the presentation of antibodies to inflammatory CAMs on polyvinyl alcohol (PVA) and alginate hydrogels to achieve strong adhesion to inflamed ECs. We synthesized photocrosslinkable, aminated PVA hydrogels and determined the effect of substrate stiffness on cell adhesion. We also evaluated the effects of antibody presentation on cell adhesion strength and dynamics using alginate hydrogels. Taken together, the results of this work may be used to design hydrogels for vascular remodeling applications under shear stress, including embolic agents for cerebral aneurysms.

TABLE OF CONTENTS

LIST OF FIGURES AND TABLES

Figures

Tables

ACKNOWLEDGMENTS

I truly appreciate the support I have received throughout my graduate studies. I would first like to thank my advisor, Professor Debra Auguste, for believing in me and giving me the necessary tools to become an independent scientist. I would also like to thank my former and present thesis committee members Professor Howard Stone, Professor David Mooney, and Professor William Bossert for their unique insights and for their valuable questions and advice. To Dr. Martin Heller, I appreciate your help with the COMSOL code. To Professor Efthimios Kaxiras and Amanda Peters Randles, thank you for your assistance with the 3D computational model. To Dr. James Rabinov, your clinical observations and important information about patients with aneurysms were invaluable to my thesis. To Professor ChoKyun Rha and T. G. "Sam" Sambandan, I am grateful for your guidance in my early career and for continuing to support me in my research endeavors.

Many thanks to former and present Auguste lab members Dr. Jin-Oh You, Dr. Rico Gunawan, Dr. Eleftherios Sachlos, Dr. Sotirios Banakos, Dr. Peng Guo, Renita Horton, Kyle Satterstrom, Dariela Almeda, George Ye, Joanna Deveau, Aazam Vahdatshoar, Lisa Rotenstein, Jennifer Hu, Yongtian Tan, Andrew Wong, Aikaterini Mantzavinou, Ted Ho, Derek Vigil, Danielle Raad, and Bib Yang for being not only wonderful labmates, mentors, and mentees but also amazing friends—I have learned so much from working with you all, and graduate school would not have been as enjoyable without you. I would especially like to thank my parents, Hassan and Soraya Rafat, and brother, Mehdi Rafat, for their unconditional love and support. Finally, I would like to thank my fiancé, Matthew Nielsen, for his constant understanding and encouragement.

This work was supported by the National Science Foundation (DMR-1055412) and the American Heart Association's Founders Affiliate Predoctoral Fellowship.

1 INTRODUCTION

1.1 Cerebral Aneurysms

Weak areas in the walls of vasculature can expand to form blood-filled sacs called aneurysms, which are characterized as saccular (berry-like) or fusiform (spindle-shaped) [1]. This dissertation focuses on intracranial saccular aneurysms. Approximately 400 million people worldwide and 10-15 million people in the United States harbor unruptured saccular aneurysms that could potentially rupture at any time [2, 3]. Aneurysm size usually ranges from 2 to 25 mm but can reach 50 mm [4, 5]. The mechanisms behind aneurysm growth and rupture are unknown, creating difficulties in decision-making for treatment. An increased understanding of hemodynamics, mechanical forces, and biological remodeling within aneurysms is necessary for the discovery of improved treatment methods.

Although the factors leading to aneurysm formation and growth are unidentified, it is speculated that genetics, hypertension, smoking, or biochemical disorders play an important role [1]. Each year approximately 30,000 aneurysms rupture in the United States, causing stroke, permanent nerve damage, or more commonly, subarachnoid hemorrhage (SAH). The mortality associated with SAH is 40% while less than 25% of the survivors recover fully from this disease [6]. The pathogenesis of saccular aneurysms is complex and involves the overlap of mechanical and biological factors that lead to the eventual rupture of the vessel. Finding a treatment that successfully prevents rupture is necessary for reducing the number of victims of this disease.

Cerebral arteries differ from other arteries in that they do not possess an external elastic lamina, which provides added mechanical support to vessels. The propensity for aneurysm formation at or near the apex of a bifurcation is well-established [7]. Irregularities in the media and internal elastic lamina at the bifurcations of vessels could be a factor in aneurysm

pathogenesis [8]. It is also known that hemodynamic stresses, including pressure and shear, have a major function in the development of aneurysms. The pathogenesis of saccular aneurysms is complex and involves the overlap of mechanical and biological factors that lead to the eventual rupture of the vessel.

1.2 Fluid Dynamics Studies

The hemodynamics of vasculature is of paramount importance in aneurysm formation. Because of this, many studies have tried to recreate fluid flow *in vitro* in order to understand aneurysm pathology. Imbesi and Kerber have created clear elastic silicone replicas of fresh human cadaver ruptured arterial aneurysms and subjected them to physiological pulsatile flow [9]. Fluid slipstreams were observed in regions of vessel curvature, which may interact with the arterial bifurcation and lead to aneurysm formation. This study showed unique flows in geometrically valid aneurysms, but the lack of resemblance of the vessel in mechanical properties such as elasticity casts doubt as to whether or not this model is accurate *in vivo*.

Wall shear stress is a key factor in aneurysm formation and expansion, so understanding how fluid shear stress impacts the vasculature walls is necessary. Shear stress has been evaluated in fully developed aneurysms with irregular shapes by constructing geometrically realistic acrylic models from three-dimensional (3D) computer tomographic (CT) angiography [10]. In addition, it was found that shear stress was not uniform in middle cerebral artery (MCA) aneurysm walls, and more realistic analysis of shear stress was attempted for comparison to the ideal spherical case. Another result from this study showed that the shear stress is highest in the tip of an aneurysm where blebs formed at 93% of the shear stress in the parent artery. However, a subsequent study used computational fluid dynamics (CFD) to create a mathematical model of

MCA aneurysms to quantify wall shear stress more accurately [11]. The research shows that the highest wall shear stress was found in the neck and not in the tip, where the shear stress was approximately 14 N/m^2, four times higher than the parent vessel region. These conflicting results show how neglecting mechanical parameters of vessels like compliance and elasticity can severely affect the outcome of quantitative results.

CFD is frequently used to analyze complex fluid behavior, which is especially significant to this research. We can no longer approximate shear stress using the Hagen-Poiseuille law because of the complex and dynamic nature of blood vessels. Accurate quantification of wall shear stress is critical for understanding the biological response of the vasculature to hemodynamics. Using Lagrangian interpolation functions and magnetic resonance imaging, Cheng et al. have created a blood vessel model to quantify wall shear stress to better account for physiological complexities [12]. Moreover, a CFD model has been developed to predict the flow structures in aneurysms comparable to traditional angiography [13]. Meng et al. reported that the initiation of aneurysm formation at the apices of bifurcations was caused by high wall shear stress and high shear stress gradients while Shojima et al. showed that low shear stresses in the sac may potentially contribute to the growth and eventual rupture of aneurysms [11, 14]. It is this complex dynamic that generates difficulties in understanding the pathologic mechanisms of aneurysms.

Though all of the studies mentioned have added new and important information to the field, the analyses they present are incomplete because of their oversight of biological and vascular remodeling events that could dictate changes in fluid dynamics. For example, assumptions such as a rigid wall model and blood as a Newtonian fluid limit the accuracy and

reliability of the previously mentioned CFD models. Biological factors that coincide with hemodynamics as well as aneurysm progression are discussed in the next section.

1.3 Using Hemodynamics to Understand Biology

The process of aneurysm growth and rupture is a combination of physical and biological phenomena. Much of the literature on cerebral aneurysms concerns biological aspects of their formation and growth. Complex vascular wall modeling events may contribute to aneurysm development. Many groups have surgically created fully-formed aneurysms in animal models [15-20]. Meng et al., however, attempted to recreate aneurysm initiation in a canine model to monitor aneurysm growth [14, 21]. Consistent with the fact that aneurysms usually occur in areas of bifurcation in the vasculature, this group surgically created a bifurcation in the carotid vasculature and performed histological and CFD analyses after two weeks or two months. They claimed evidence of aneurysm growth and wall remodeling events such as hyperplasia and the disruption of the internal elastic lamina and medial layer at the apex of the bifurcation. It would have been more interesting to confirm formation by allowing the so-called aneurysms to grow in the canines and to further analyze whether or not this result was the product of surgery. Another group used CFD and physiological data to understand aneurysm growth [22]. They explored the hypotheses of shear stress-mediated loss of vascular tone through smooth muscle cell apoptosis and subsequent rupture, degradation, and reconstruction of the medial collagen and elastin fibers. The authors claimed that their model was able to predict aneurysm growth and correlate aneurysm development. Although this study gave insight into observed remodeling events, the simplified assumptions and lack of a physical model correlating with their results leave many unanswered questions for future studies.

Another major area of interest in this field is the examination of cellular and biological factors in areas of aneurysm formation and growth. The studies presenting this type of analysis aim to determine the biochemical events that are involved in aneurysm growth. Sadamasa et al. analyzed the role of endothelin B receptors (ETBRs) in aneurysm progression in rat models [23]. In this study, ETBRs were found to be involved in mechanically induced smooth muscle cell apoptosis. After aneurysm induction in rats, substantial ETBR expression was found in smooth muscle cells after 3 months of aneurysm induction. The administration of K-8794, a selective ETBR inhibitor, significantly reduced apoptotic smooth muscle cells and prevented complete aneurysm formation. Although ETBR may be important in aneurysm pathology of rats, analysis in human vasculature is imperative for the validation of this conclusion. Hemodynamic evaluation in vessels has not been done, so the quantification of shear stress at certain points of ETBR expression will be beneficial for a more complete understanding of this phenomenon.

Additional studies exploring the biochemical basis of aneurysm formation have involved signaling molecules such as nitric oxide and interleukin-1β (IL-1β) [24, 25]. The role of inducible nitric oxide synthase (iNOS), a transcriptionally regulated nitric oxide producer that is expressed in humans and rat cerebral aneurysms, has been analyzed in a new iNOS knockout mouse model. After subjecting iNOS knockout mice to an aneurysm induction procedure, iNOS was not deemed necessary for aneurysm initiation; however, it was involved in aneurysm growth and smooth muscle cell apoptosis. Furthermore, IL-1β is a proinflammatory cytokine involved in iNOS activation. The production of IL-1β knockout mice showed that IL-1β is important in aneurysm progression but not initiation, similar to the effect seen with iNOS. Thus, iNOS and IL-1β molecules may be significant in the understanding of aneurysm pathological development. Matrix remodeling elements including matrix metalloproteinases (MMPs), which are involved in

the degradation of extracellular matrix (ECM) components, have also been studied in the aneurismal context because of their role in medial wall thinning and disruption of the internal elastic lamina. For example, Aoki et al. evaluated the effect of MMP2 and 9 expression in rats [26]. An inflammatory response in induced aneurysms caused macrophages to express MMP2 and 9, which contributed to aneurysm progression. Because this research was only conducted in mouse and rat models, it will be difficult to predict whether or not human aneurysm development is managed by the same factors. Another important consideration in this pathobiology is complement activation [27]. Tulamo et al. showed that membrane attack complex deposition is associated with wall degeneration and rupture in cerebral aneurysms in humans. This study determined that complement activation may be involved in both the progression and rupture of aneurysms and suggested that complement-mediated cell death may likely be independent of apoptotic mechanisms. Some complexities of aneurysm development have been elucidated here. Given the findings of the above studies, the use of anti-inflammatory agents to prevent destructive tissue remodeling may be important in aneurysm treatment.

Since endothelial cells (ECs) come in direct contact with blood flow, understanding their biochemical response to physical flows is essential. Malek et al. conducted extensive studies on the biological response of ECs due to fluid flow and shear [28-32]. In one study, they exposed monolayers of bovine aortic ECs to physiological fluid shear stresses of 4, 15, 20, or 36 dynes/cm^2 with a cone-plate viscometer, allowing the cells to experience steady laminar, turbulent, and pulsatile shear stresses. Thrombomodulin, a thrombin-binding EC surface receptor involved in thrombosis protection, was found to be downregulated by shear, while fibrinolytic tissue plasminogen activator was increased, demonstrating the dynamic response of ECs under flow conditions. Shear was shown to regulate EC expression of endothelin-1 (ET-1), basic

fibroblast growth factor (bFGF), and platelet-derived growth factor B (PDGF-B) mRNA. ET-1, a potent vasoconstrictor, was downregulated up to five fold in response to shear stress. PDGF-B, a mitogen and vasoconstrictor, was downregulated while bFGF, a growth and migration regulator, was upregulated due to shear. These studies showed that the morphology of vascular ECs was sensitive to shear since high shear stress resulted in spindle-like cell shape. In another study, endothelial nitric oxide synthase (eNOS), which synthesizes the vasodilator nitric oxide and is involved in vascular remodeling, was found to be modulated by physical and chemical factors. Steady shear stress increased eNOS levels while hydrostatic pressure, hypoxia, and high glucose decreased levels. These studies have not shown significant changes in trends of gene expression when comparing flow character (steady, pulsatile); rather, gene expression was dependent on shear stress magnitude and exposure time. This result is surprising, and it may be true for the specific factors analyzed under the conditions described. However, it should be noted that the experimental set-up used in these studies differs vastly from *in vivo* conditions. Because of this discrepancy, a more comprehensive study detailing other important factors in EC regulation and response to shear is necessary along with a more physiologically relevant method of inducing shear. Nevertheless, these results elucidate the complexities of EC biochemistry as well as vessel remodeling characteristics, which will be useful for understanding the development of aneurysms.

Many of the studies dealing with the biochemical responses implicated in vascular remodeling and aneurysm pathology are incomplete. Some studies only consider biochemical factors and gene expression with little emphasis on hemodynamic quantification whereas others look to CFD or *in vitro* results without sufficient *in vivo* validation. It is especially difficult to draw conclusions from studies based on animal experiments, as it is unclear whether human

vasculature differs. Further studies that involve adequate combinations of physical and biological analysis that closely correlate with *in vivo* conditions should be conducted so that the fundamental mechanisms of aneurysm formation and growth can be better understood.

1.4 Current Aneurysm Treatments and Limitations

There are two common methods of aneurysm treatment: microvascular clipping and endovascular embolization. Microvascular clipping involves a highly invasive craniotomy where the aneurysm neck is directly clipped to block blood flow. Although this technique is broadly used for preventing aneurysm rupture, its highly invasive nature poses risks for procedural complications and patient disability [33]. The less invasive technique of endovascular embolization utilizes the packing of platinum Guglielmi detachable coils directed through a catheter in the aneurysm in order to prevent rupture. Although this procedure has emerged as an acceptable alternative to surgery in many cases, the inability to treat wide-necked, large, or giant aneurysms via endovascular embolization is a major obstacle. The possibility of coil herniation into the parent vessel, incomplete aneurysm occlusion, and aneurysm recanalization creates difficulties in this treatment [34]. Both microvascular clipping and endovascular embolization have failure rates between 5-20% (from discussions with Dr. James Rabinov, Massachusetts General Hospital). Therefore, improvements upon these techniques or new minimally-invasive strategies need to be designed to enable treatment of a wide variety of aneurysm geometries.

Novel materials that can be used *in situ* for aneurysm occlusion via minimally-invasive strategies are highly desirable. Microvascular clipping or endovascular embolization are either too invasive or cannot be used for all aneurysm sizes and shapes [33, 34]. In a recent study, clipping has been found to be used more clinically than coiling despite the increased hospital

complications and mortality rates associated with clipping [35]; this is likely due to aneurysm geometries unfavorable for coiling [36]. A minimally-invasive endovascular method for aneurysm treatment that can be used for all aneurysm geometries is necessary to prevent the risks related to clipping.

There are many limitations to the endovascular embolization technique that uses bare platinum coils, including inability to fill the aneurysm completely and delayed thrombus and organized tissue formation, which leave the area susceptible to recanalization and rupture [37]. To address these obstacles, a variety of systems of coils are being investigated for improving the vascular embolization technique. The HydroCoil system, for example, increases the coil packing density through the pH sensitive polymethacrylic acid hydrogel that expands when released into the aneurysm [38]. Additionally, the matrix detachable coil uses the biodegradable copolymer poly(lactic-co-glycolic acid) in order to induce an inflammatory response for acceleration of aneurysm healing through smooth muscle cell migration and thrombus organization [39]. Other variations such as nylon fibered and polyglycolic acid coated coils have been used in the clinic [40, 41]. It was found, however, that none of the methods discussed provided a significant improvement over the bare coil technique and therefore are not warranted for use in the clinic due to increased costs and unknown long-term effects in general [42].

In more iterations of the original bare platinum coil, coatings that incorporate drug delivery methods and bioactivity have been investigated [37]. The idea here is an extension of the original goal: include a gel to fill the aneurysm space with an agent that promotes cell growth and healing. One such study used platinum coils with bFGF within a polyvinyl alcohol (PVA) core to encourage cell proliferation and increased wall thickness [43]. Another study used platinum coils embedded with fibroblast cells for fibrosis induction [44]. Despite the fact that

these methods increased packing and accelerated tissue organization, they provided no considerable advantage in practice. They had many of the same limitations as the current treatment methods, including potential for parent artery stenosis, induction of detrimental inflammatory responses, and precipitation of thromboembolic events [37].

To address the problem of not being able to use coils with large or wide-necked aneurysms, endovascular stent-assisted coiling technologies have emerged. The Neuroform stent can be placed in the intracranial aneurysm area to create a barrier for coils to be packed tightly within aneurysms [45]. Other advantages of this technique are that the stent can prevent blood flow from entering the aneurysm and that it can create a potential scaffold for cell in-growth, which may facilitate tissue organization events [37]. However, this technique is limited by technical challenges and is sometimes impossible to use for certain vessel geometries, and many thromboembolic complications have been reported [46]. More recently, the Cordis Enterprise stent system has been implemented with the characteristics of a closed-cell design, which may enable greater mobility and control within the vasculature during intraoperative procedures [47]. Further clinical research needs to be done to prove the efficacy of this technique, but its thrombogenic properties still remain a challenge.

Variations of coiling mechanisms are not the only avenues being explored for the treatment of aneurysms. For example, a recent study proposed the use of an endovascular clip system (eCLIPs) that combined the concepts of microvascular clipping and stent technology through a flexible device that is anchored at the aneurysm neck and can expand to occlude the aneurysm area and deflect blood flow [48]. No clinical trials have yet been done with this device. Liquid embolic agents are also being explored for treatment technologies. The Onyx liquid embolic system consists of ethylene vinyl alcohol in dimethyl sulfoxide and precipitates *in situ*

upon entering the vessel [49]. This technique is widely used in the treatment of arteriovenous malformations. The liquid can conform to any aneurysm shape and completely occlude the area. However, the agent is not bioactive and is difficult to administer; alternative ideas are needed to improve upon these limitations [37].

Many groups have tried to improve upon current aneurysm treatment techniques in incremental steps. Endovascular embolization is becoming the preferred method of aneurysm treatment over surgical clipping based on the International Subarachnoid Aneurysm Trial [50]. Furthermore, the Cerebral Aneurysm Rerupture After Treatment study concluded that complete aneurysm occlusion should be pursued to minimize risks of aneurysm rupture [51]. Considering the limitations of current technologies and the characteristics desired in an optimal aneurysm treatment, we can imagine a new treatment technology that uses a bioactive gel that forms *in situ* to conform to the aneurysm geometry, fills and adheres to the entire space, and diverts the blood flow away from the area to facilitate healing.

1.5 Inflammation and Endothelial Cells

Upon incitement of the inflammatory cascade due to infection or tissue damage, leukocytes adhere to the EC lining of the vessel wall via the presentation of specific surface molecules [52]. The expression of endothelial-leukocyte adhesion molecules, including endothelial leukocyte adhesion molecule-1 (E-selectin), vascular cell adhesion molecule-1 (VCAM1), and intercellular adhesion molecule-1 (ICAM1), indicates EC “activation” and mediates the progression of the inflammatory process. The inflammatory process has been elucidated: leukocytes are recruited to inflamed areas and proceed to roll and tether to the endothelium. They then adhere firmly and move to cell junctions where they finally transmigrate

across the endothelial barrier [53-59]. Several key cell adhesion molecules (CAMs) are involved in this process. E-selectin, an endothelial glycoprotein that supports adhesion of neutrophils, monocytes, and eosinophils, is expressed in response to inflammatory cytokines such as interleukin-1 (IL-1) and tumor necrosis factor (TNF). E-selectin is implicated in the tethering and rolling of leukocytes during the inflammatory cascade. In addition, VCAM1 and ICAM1 are both immunoglobulin (IgG) CAMs upregulated upon exposure to inflammatory stimuli [60, 61]. These CAMs are responsible for the firm adhesion of cells to the endothelium and their migration to cell junctions [62]. The enhanced expression of inflammatory cell adhesion molecules is a hallmark of many diseases, including atherosclerosis [63-65], ischemia and reperfusion injury due to myocardial infarction or stroke [66-68], and cerebral aneurysms [62, 69].

Because the innermost lining of blood vessels is comprised of ECs [70], materials implanted into the vasculature come into extensive contact with ECs [71]. Cellular adhesion, proliferation, migration, and differentiation are directly influenced by the interactions between cells and their external environment. Soluble and bound chemical molecules as well as physical cues can regulate this behavior [72]. Understanding the EC response in the inflammatory environment can improve the interactions of biomaterials with the vasculature, particularly with inflamed endothelium.

1.6 Cell Adhesion Strategies in Tissue Engineering

The field of tissue engineering seeks to design strategies for the improvement or replacement of biological function. One fundamental concern in designing tissue engineering scaffolds is the adhesion and recruitment of cells. The advent of the specific cellular recognition

sequence peptide arginine-glycine-aspartic acid (RGD) that comprises the adhesion domains of fibronectin and other ECM glycoproteins has facilitated cell adhesion on synthetic materials [73]. The ability of cells to adhere to materials and subsequently migrate is necessary for angiogenesis and regenerative processes [74]. The density of cell adhesion peptides has been examined: if there are too few ligands, cells cannot successfully adhere and integrate into the material; if surfaces are saturated with adhesion peptides, cells cannot migrate effectively [75]. Thus, the density of adhesive ligands must be balanced for optimal cell function within biomaterials.

Cell adhesion to materials can be enhanced through engineering of ligand presentation on synthetic materials. The cellular response to bound signals from the ECM has been explored extensively [76]. The ECM is composed of protein fibers integrated within a network of glycosaminoglycan chains that provide structural support. Cellular processes can be controlled by mimicking the structure of the ECM in biomaterials [77]. Peptides from larger proteins found in the ECM are commonly used as cell adhesion targets because transmembrane cellular receptors can interact with these ECM adhesion ligands to promote binding [78].

An alternative approach involves modifying materials with antibodies complementary to CAMs expressed during inflammation [79]. The upregulation by ECs of specific CAMs in response to inflammation has been well-characterized. While CAMs are usually used to mediate interactions between ECs and inflammatory cell subsets, it may be possible to exploit CAM expression for biomaterials design. Specifically, the EC expression responses of E-selectin, VCAM1, and ICAM1 during exposure to inflammation-mimicking stimulation are of interest. Each of these molecules is involved in cell adhesion, recruitment of leukocytes, or tissue remodeling [52, 80], and they are the CAMs most commonly expressed on activated

endothelium. Presentation of antibodies against E-selectin, VCAM1, and ICAM1 on materials surfaces could allow for engineering of preferential binding of activated ECs. Because antigen-antibody interactions are known to allow for firm adhesion under flow [81], such interactions could further provide for effective adhesion that resists weakening due to hemodynamic forces.

1.7 Cooperativity in Biology

Cooperativity observed in biology links individual molecular interactions to system level properties [82]. Cooperativity is a biophysical phenomenon in which the binding of one ligand increases the probability that other ligands will bind [83]. In cooperativity that is due to polyvalency, the binding of one ligand makes subsequent interactions more favorable by reducing the number of nonproductive configurations and the entropic penalty of binding each additional ligand. Thus, multiple receptor-ligand interactions yield an overall strong adhesion.

Cooperative binding is widely observed in biological systems. It is most highly evident among proteins and glycans and can occur in solution or on cell membrane surfaces. Numerous studies have also reported a decrease in the dissociation constant when a third molecule is used to enhance binding between two other molecules. For example, bFGF has bound cell surface receptors cooperatively with the help of heparin sulfate proteoglycans [84].

Mimicking cooperative interactions on synthetic matrices has only recently been employed in drug delivery [85-87]. Cooperative cell binding of receptors to molecules allows for enhanced adhesion strength, possibly due to the fact that multiple ligand-receptor bonds need to be broken simultaneously in contrast to independent adhesion where bonds rupture sequentially [88]. In this dissertation, we explored the conditions that would facilitate cooperative binding and promote strong, synergistic adhesion of cells to biomaterials.

1.8 Thesis Hypothesis and Experimental Strategy

We hypothesized that by understanding how hemodynamics and biological response are coupled in aneurysms, we may be able to design a new occlusion strategy. We have used computational modeling, evaluation of the response of EC surface markers, and the fabrication of novel biomaterials to explore new embolic materials. This dissertation is composed of three aims; an overview of each aim is described below. A list of publications resulting from the work described in this dissertation is shown in **Appendix A**.

Aim 1 is focused on defining flow regimes based on the hemodynamic and geometric parameters of aneurysms. We hypothesized that changes in flow patterns may affect the shear stress experienced on the aneurysm wall, which may correlate to rupture. Because aneurysm geometry plays an important role in hemodynamics, we used this idea to model changes in hemodynamics within varying aneurysm geometries computationally.

In aim 2, we coupled hemodynamics and biological response *in vitro*. Changes in shear stress and the inflammatory environment may alter EC expression of CAMs and matrix remodeling factors. We evaluated the effect of shear stress and inflammatory cytokines on EC gene and protein expression. We then used this information to design hydrogels that may adhere to the vascular endothelium, as detailed in the final aim.

Finally, we explored the use of hydrogels as aneurysm occlusion materials in aim 3. We showed that antibody-conjugated hydrogels may promote synergistic EC adhesion using cooperativity as an adhesion strategy. We built upon the existing idea of liquid embolization using novel materials that promote cell adhesion. This technique is unique from the other treatments discussed previously in that it includes the ability for adhesion to the aneurysm area

through a bioactive mechanism. We addressed the limitations of previous treatment methods, namely complete occlusion, ease and rapidity of procedure, and strong cell adhesion. To this end, we have synthesized photocrosslinkable polyvinyl alcohol (PVA) hydrogels as well as alginate hydrogels that are conjugated with antibodies to CAMs that complement EC surface expression during the inflammatory response. These modified hydrogels can form *in situ*, conform to any geometry, and exhibit strong, synergistic adhesion to activated ECs.

2 PROBING GEOMETRY AND HEMODYNAMICS IN ANEURYSMS

2.1 Introduction

Recent studies of aneurysm hemodynamics focus on a limited number of geometries or Reynolds numbers (Re) that cannot be applied to a wide range of patient-specific cases. In this section, we analyzed flow patterns and wall shear stress (WSS) using non-dimensional analysis in order to assess a range of clinically relevant, idealized geometries and Re to characterize the hemodynamic landscape and transition boundaries between distinct flow patterns. Geometries were altered by increasing the height to width (H_A/W_A) ratio of the aneurysm and neck width to parent vessel width (W_N/W_P) ratio, which have been identified as significant in prior clinical studies. Aneurysms were centered at the midpoint of a bifurcation, offset from the bifurcation midpoint, and located on a sidewall vessel. We demonstrated that at constant geometry small changes in Re can alter hemodynamics. We observed a prevalence of eddies at low W_N/W_P and high H_A/W_A for all aneurysm types. For constant geometries, areas of low WSS (<0.01 N/m^2) decreased with increasing Re for centered aneurysms, but offset and sidewall aneurysm areas remained unchanged. We have identified how hemodynamic patterns and transitions correlate with geometry and Re, which may be useful in the study of aneurysm pathophysiology.

Predictions of aneurysm growth and rupture may be achieved by understanding the fluid and solid mechanics of blood flow and vessel structure. We used numerical methods to study flow patterns in clinically relevant, idealized aneurysm geometries whose significance has been suggested by recent clinical studies that relate hemodynamics (Re from 0-500 and flow patterns), geometry, and wall shear stress (WSS) [89].

Numerical simulations, computational fluid dynamic (CFD) models, and geometric analyses are among the many approaches taken to study the pathophysiology of aneurysms.

These hemodynamic studies have attempted to elucidate distinguishing flow features of aneurysms. One analysis used the finite-element method (FEM) to determine the velocity fields in wide and narrow necked aneurysms under pulsatile flow at two Re [7]. They speculated that eddy formation in the center of the aneurysm may contribute to thrombus formation or cell aggregation, which can lead to growth and rupture of an aneurysm. FEM was also used in a two-dimensional (2D) model of sidewall aneurysms under steady flow [90]. The magnitude of shear stress on the aneurysm wall was shown to depend on the geometry, which suggests that the shape of the aneurysm influences aneurysm growth. These and other studies agree that aneurysm hemodynamics are a function of the geometry and Re [1]. The outcome of these hemodynamic changes is unclear, but only limited simulations for a small number of geometries have been reported.

Several hypotheses have been made that link geometric factors to aneurysm rupture [89-92]. The risk of rupture in patient-specific aneurysm geometries has been evaluated using a CFD model based on three-dimensional (3D) angiographs of real patients. Complex flows and narrow inflow jets are shown to be characteristic of ruptured aneurysms [91]. A correlation between an elliptical shape factor and WSS has indicated an increased susceptibility to rupture [92]. Statistical analysis in patients with both unruptured and ruptured aneurysms revealed that 2D shape factors correlated with sidewall aneurysm rupture [89]. We have built upon this work by describing the hemodynamic phenomena (i.e. WSS, approximate flow fields) that arise due to changes in aneurysm geometries identified as significant in these studies. We observed flow pattern transition boundaries as a function of geometry and Re, which could lead to the correlation between aneurysm shape and rupture for diagnostic purposes.

This brief survey shows that many unanswered questions remain for elucidating the link between hemodynamic features, aneurysm geometry, and rupture. Though it is generally accepted that hemodynamics is important in understanding the fate of aneurysms, most studies focus on a limited number of geometries and flow rates. This does not allow extension of the conclusions to a wide range of aneurysms. We have probed the relationship of aneurysm geometry to flow patterns using non-dimensional terms, which allows for broad application of our data to patient-specific aneurysms. Our findings have shown that flow characteristics are sensitive to changes in geometry and Re. Additionally, because WSS has previously been implicated in aneurysm growth and rupture, we evaluated how the shear stress at the aneurysm wall relates to differences in geometry [93]. Our systematic evaluation of aneurysm hemodynamics may be useful in correlating common features amongst computational investigations that focus on patient-specific data. This work may provide insight into aneurysm pathophysiology.

2.2 Methods and Materials

In this study, a "flow mapping" scheme is presented to evaluate geometric features of saccular aneurysms over a range of Re. We have categorized aneurysm geometries by their height to width (height of the aneurysm/width of the aneurysm or H_A/W_A) and neck to parent (width of the aneurysm neck/width of the parent vessel or W_N/W_P) ratios (**Fig. 2.1A**). Flow patterns were evaluated for aneurysm geometries centered on a bifurcating vessel, offset from a bifurcating vessel, and located on a sidewall vessel. **Table 2.1** depicts the heights and widths of all aneurysm geometries used in the simulations. For each flow map, eleven Re (0.5, 1, 5, 10, 50, 100, 150, 200, 250, 300, and 500) and four W_N/W_P ratios (approximately 0.25, 0.5, 1, and

1.5) were analyzed. Flow maps have been created for H_A/W_A ratios of 0.5, 1, 1.25, 1.5, and 1.75. WSS profiles were examined upon changing geometries; three H_A/W_A ratios and two Re were evaluated for each type of aneurysm.

Table 2.1: Aneurysm dimensions used in simulations.

H_A/W_A	Height (mm)	Width (mm)
0.5	0.5	1
	1	2
	2	4
	3	6
1	1	1
	2	2
	4	4
	6	6
1.25	1.25	1
	2.5	2
	5	4
	7.5	6
1.5	1.5	1
	3	2
	6	4
	9	6
1.75	1.75	1
	3.5	2
	7	4
	10.5	6

Aneurysm geometry

Schematics of the geometries of the aneurysms used in our computational modeling are shown in **Figures 2.1A, 2.1C, and 2.1D**. Physiological widths for the parent (entrance channel) and daughter vessels (branching or bifurcating channels) are 4 mm and 3 mm, respectively [7]. We have set the lengths of the parent and daughter vessels at 30 and 13 mm, respectively. **Figures 2.1C and 2.1D** show representative images for offset and sidewall aneurysms. We have additionally made a 2D model of a basilar artery aneurysm based on an angiogram image to confirm how our flow maps could potentially be extended to other geometric variations (**Fig. 2.1Ei and 2.1Eii**). ImageJ was used to extract the length scale information from the angiogram; the H_A/W_A and W_N/W_P ratios were found to be 1.0 in both cases.

Flow was characterized by the dimensionless Re (Eq. 2.1).

$$\mathrm{Re} = \frac{\rho W_P \bar{u}}{\eta} \qquad (2.1),$$

where ρ is the density, W_P is the width of the parent vessel, $\bar{u}$ is the mean velocity, and η is the fluid viscosity. We focus on a physiological range of 100<Re<400 [94].

Computational model

We numerically solved the Navier-Stokes (Eq. 2.2) and continuity (Eq. 2.3) equations assuming incompressible flow of a Newtonian fluid using the COMSOL 3.3 Multiphysics FEM software:

$$\rho\left(\frac{\partial \boldsymbol{u}}{\partial t} + (\boldsymbol{u}\cdot\nabla)\boldsymbol{u}\right) = -\nabla p + \eta\nabla^2\boldsymbol{u} \qquad (2.2)$$

$$\nabla \cdot \boldsymbol{u} = 0 \qquad (2.3),$$

where p is the pressure, $\boldsymbol{u}$ is the velocity vector, and η is the fluid viscosity. Blood density and viscosity are typically 1060 kg/m^3 and 3 cP, respectively [95, 96]. We assumed 2D, steady ($\frac{\partial \boldsymbol{u}}{\partial t} = 0$), laminar flow in a rigid wall model of a vessel [7, 92, 97]. The no slip condition was applied at the wall. The MATLAB code used to run simulations in COMSOL is shown in **Appendix B**.

WSS profiles were calculated along the aneurysm boundary arc length for varying H_A/W_A and Re (100 and 400). It is convenient to present these results by reporting the arc length ratio, by which we denote the fraction of the arc length that experienced low shear stress (< 0.01 N/m^2). The results utilize an arc length that is non-dimensionalized by the parent vessel width.

The geometries were resolved with a fine mesh with a minimum of 7,400 elements (**Fig. 2.1B**). Special attention was paid to the region of the aneurysm and the corners, and we confirmed that the streamlines and WSS profiles converge by using both coarser and finer meshes.

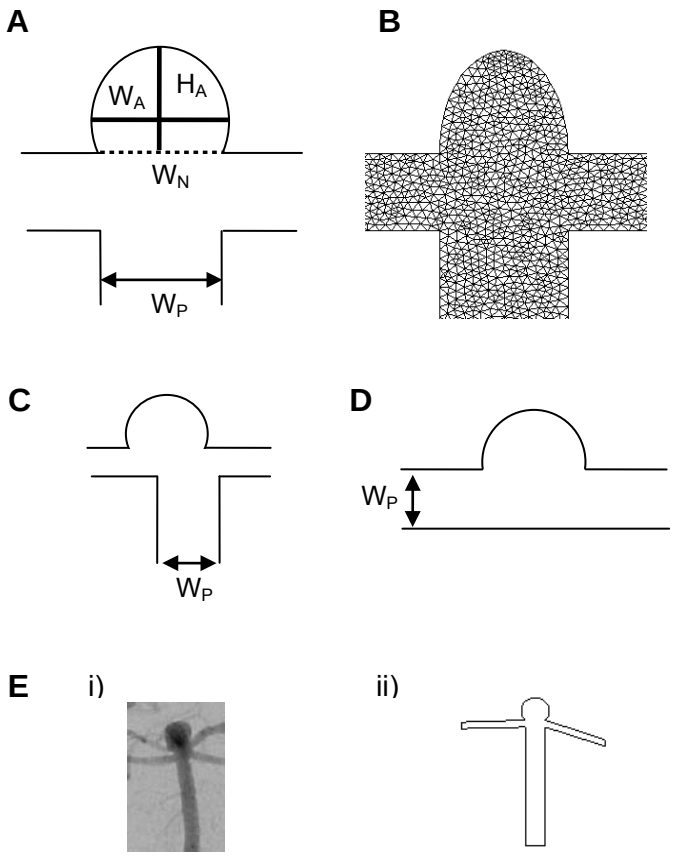

Figure 2.1: Geometric parameters. (A) Centered aneurysm model and definition of parameters. The height (H_A) and width (W_A) of the aneurysm are indicated by solid vertical and horizontal lines, respectively. The width of the neck (W_N) and parent vessel (W_P) are respectively shown by a dashed horizontal line and arrows. (B) Typical mesh used to resolve the aneurysm geometries. (C) Representative offset aneurysm. (D) Representative sidewall aneurysm. (E) i) Angiogram of basilar artery aneurysm. ii) Computational model geometry of angiogram.

By visually inspecting various streamline patterns, we have created flow maps by plotting W_N/W_P versus Re for multiple H_A/W_A values and qualitatively demarcating the transitions between streamline patterns. Mapping of the distinct flow patterns defined common characteristics that appear as a function of Re and geometry. Representative images of the aneurysm geometry were placed at the bottom of each graph for visualization of W_N/W_P. Flow asymmetry was relative to the midpoint line of the aneurysm centered on the aneurysm neck. The physiologically relevant Re range is located between the dashed lines.

We have categorized flow patterns based on geometry and flow characteristics. Our assumptions allowed us to perform simulations that identify macroscopic flow features and transition boundaries which correlate with patient-specific aneurysms. Similar assumptions of 2D geometry, steady flow, and rigid walls have been used in a variety of flow studies [7, 90, 97-99]. Our focus in this study is on the systematic organization of hemodynamic patterns into "flow maps" which categorize qualitatively distinct flow features and transition boundaries. In this approach, the assumptions made are reasonable to describe the qualitative features of flow. There are significant differences between 2D and 3D hemodynamic studies; however, similarities exist among the qualitative flow patterns [100]. It has been previously shown through experiment and computational models that pulsatile character does not affect flow characteristics qualitatively [97, 98, 101-103]. In addition, vessel elasticity has been shown to not significantly alter flow patterns or the average velocity within aneurysm geometries [7, 90, 99, 100, 103, 104]. It is not our position that these simulations mimic clinical aneurysms exactly but that analysis of aneurysm shape factors and flow conditions in a systematic fashion can be used to recognize common hemodynamic patterns and transition boundaries.

2.3 Intra-Arterial Flow Patterns in Symmetric Aneurysms

Six characteristic flow patterns (**Fig. 2.2**) were found commonly upon altering the aneurysm geometry (H_A/W_A, W_N/W_P) and Re (defined in **Fig. 2.1A**). These patterns were distinguished qualitatively by having symmetrical (**Fig. 2.2A**) and asymmetrical (**Fig. 2.2B**) streamline patterns. The patterns showed the formation of eddies (**Fig. 2.2Ai, 2.2Bi**), penetrating bifurcating jets (**Fig. 2.2Aii, 2.2Bii**), and penetrating bifurcating jets with eddies (**Fig. 2.2Aiii, 2.2Biii**).

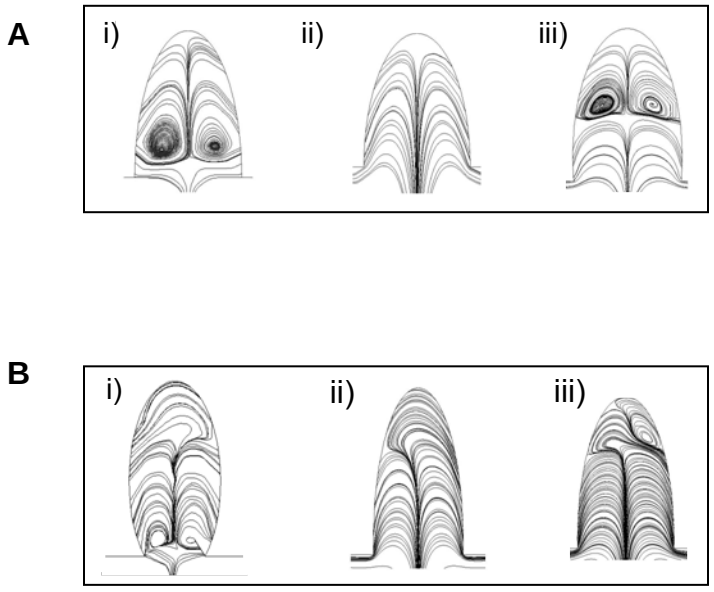

Figure 2.2: Representative streamlines. (A) Symmetric flow streamlines.i) Eddies (Re=0.5, H_A/W_A=1, W_N/W_P=0.25) ii) Penetrating bifurcating jets (Re=500, H_A/W_A=0.5, W_N/W_P=0.5) iii) Penetrating bifurcating jets with eddies (Re=200, H_A/W_A=1.5, W_N/W_P=0.4) (B) Asymmetric flow streamlines. i) Asymmetric eddies (Re=1, H_A/W_A=1.75, W_N/W_P=0.2) ii) Penetrating bifurcating jets (Re=500, H_A/W_A=1.5, W_N/W_P=1) iii) Penetrating bifurcating jets with eddies (Re=150, H_A/W_A=1.75, W_N/W_P=1.5).

We graphically depicted flow patterns for constant H_A/W_A as a function of W_N/W_P vs. Re for centered aneurysms. For H_A/W_A=0.5 (**Fig. 2.3A**), we observed a combination of penetrating bifurcating jets and eddies at low W_N/W_P and Re ($0.2<W_N/W_P<0.5$ and Re<150). Beyond this regime, only penetrating bifurcating jets were seen. Aneurysms with H_A/W_A=1 (**Fig. 2.3B**) resulted in the presence of eddies at low Re (<100) and low W_N/W_P (<0.5). Penetrating bifurcating jets with eddies were found at intermediate values of Re (100<Re<300) for $W_N/W_P<0.5$ and at low Re for $W_N/W_P>0.5$. Asymmetric bifurcating jets dominated at large Re for H_A/W_A =1. Mappings of H_A/W_A=1.25 or 1.5 (**Appendix B, Fig. 8.1**) had similar profiles to the results for H_A/W_A=1. At H_A/W_A=1.75 (**Fig. 2.3C**), the appearance of asymmetric eddies at low W_N/W_P was approximately independent of Re. Bifurcating jets with eddies existed beyond $W_N/W_P>0.5$ but only below physiologically relevant Re (100<Re<400). Asymmetric bifurcating jets with eddies were observed for physiological Re over a large range of W_N/W_P ($0.4<W_N/W_P<1.5$).

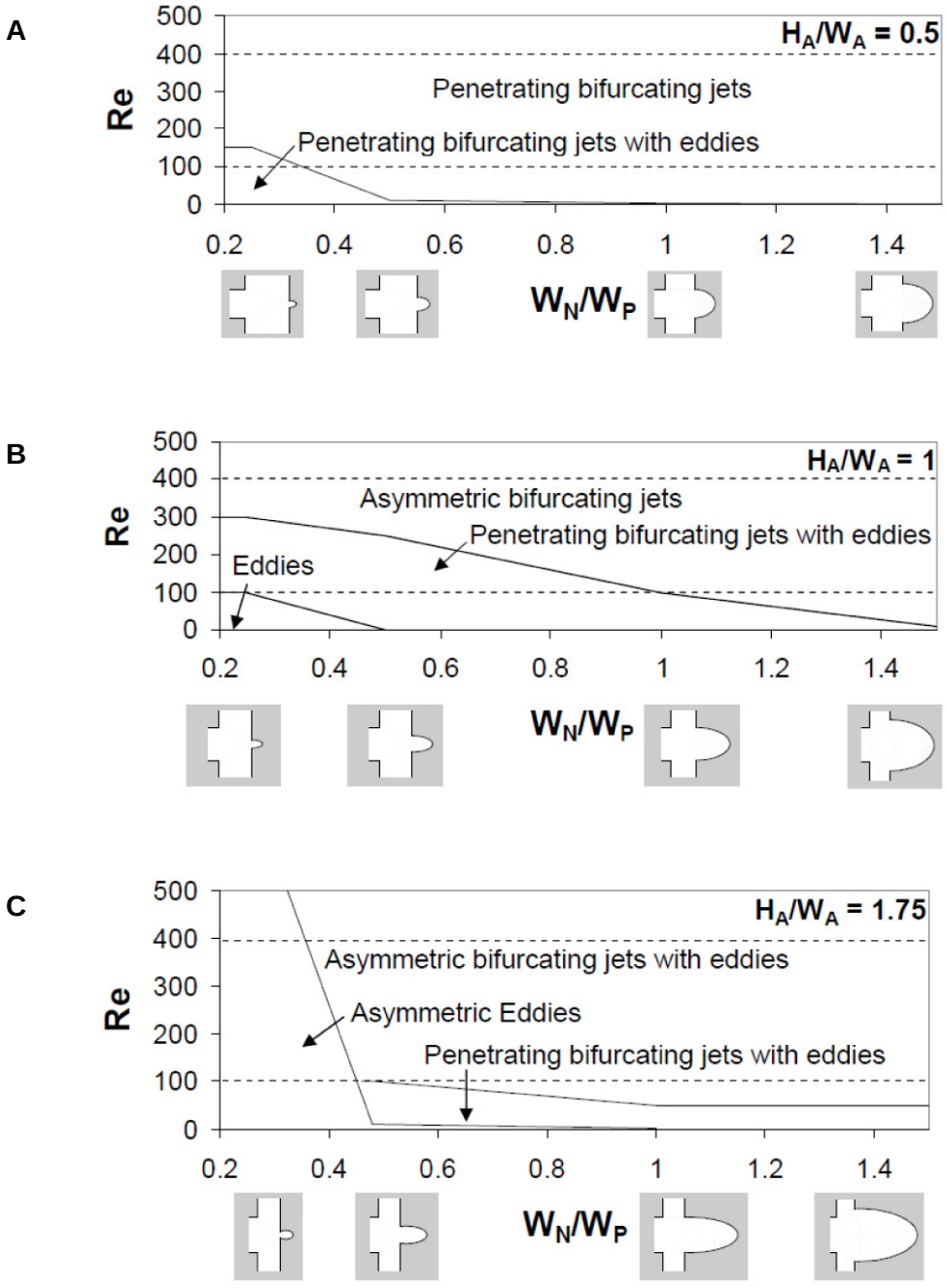

Figure 2.3: Qualitative mapping of flow patterns in symmetric aneurysms. Flow maps are shown in terms of various aneurysm height to width (H_A/W_A) ratios, Reynolds numbers (Re), and neck to parent width (W_N/W_P) ratios for symmetric aneurysms: (A) H_A/W_A=0.5 (B) H_A/W_A=1 (C) H_A/W_A=1.75. Dashed lines indicate physiological Re.

We have created a center terminated model of a basilar artery aneurysm (i.e. aneurysm with angled daughter vessels) with $H_A/W_A=1$ and $W_N/W_P=1$ to mimic the angiograph presented in **Fig. 2.1Ei**. For the range of Re considered ($0<Re<500$), all flows were asymmetric. We have determined that although the angles of the arms were not perpendicular to the parent vessel, the transition from penetrating bifurcating jets with eddies to bifurcating jets at Re=50 was similar to the symmetric aneurysm flow map with $H_A/W_A=1$ (**Fig. 2.3B)**.

2.4 Offset Aneurysms

We have studied flow patterns that arise in aneurysms offset from the inflow (**Fig. 2.1C**). The characteristic flows in this geometry consisted of eddies, penetrating jets, or penetrating jets with eddies (**Fig. 2.4Ai-iii**). For $H_A/W_A=0.5$ (**Fig. 2.4B**), two types of flows were observed: penetrating jets with eddies at low W_N/W_P and penetrating jets when $W_N/W_P>0.5$. When $H_A/W_A=1$, the flow map was dominated by penetrating jets with eddies except for a region of penetrating jets below physiological Re, $0<Re<60$, and $W_N/W_P>1$ (**Fig. 2.4C**). The mappings of $H_A/W_A=1.25$ and 1.5 (**Appendix B, Fig. 8.2**) were similar to graphs for $H_A/W_A=1.75$ (**Fig. 2.4D**). The map displayed penetrating jets with eddies, except for a region of eddies at low Re ($0<Re<50$) and W_N/W_P ($0.2<W_N/W_P<1$).

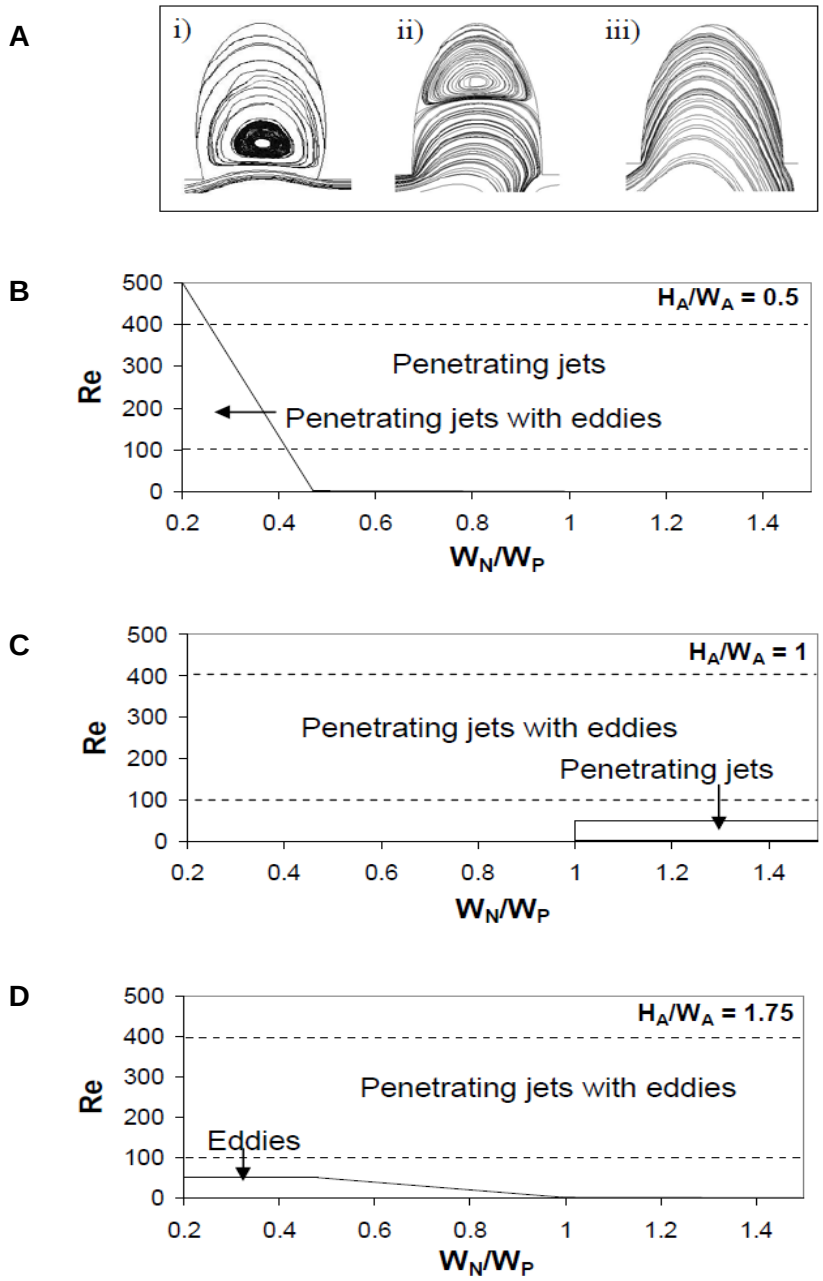

Figure 2.4: Flow mapping of offset aneurysms. (A) Examples of flow patterns in offset aneurysms. i) Eddies (Re=10, H_A/W_A=1.5, W_N/W_P=0.2) ii) Penetrating jets with eddies (Re=10, H_A/W_A=1.5, W_N/W_P=1) iii) Penetrating jets (Re=200, H_A/W_A=0.5, W_N/W_P=0.5). Flow mapping in terms of various aneurysm height to width (H_A/W_A) ratios, Reynolds numbers (Re), and neck to parent width (W_N/W_P) ratios: (B) H_A/W_A=0.5 (C) H_A/W_A=1 (D) H_A/W_A=1.75. Dashed lines indicate physiological Re.

2.5 Sidewall Aneurysms

Over the entire range of H_A/W_A, asymmetric flows dominated flow patterns in sidewall aneurysms (**Fig. 2.1D**). The characteristic asymmetric flows consisted of penetrating jets with eddies (**Fig. 2.5Ai**), eddies (**Fig. 2.5Aii**), or layered eddies (**Fig. 2.5Aiii**). For H_A/W_A=0.5 (**Fig. 2.5B**), asymmetric eddies dominated the map except for a small area of penetrating jets with eddies below physiological Re (Re<10). Similarly, H_A/W_A=1 (**Fig. 2.5C**) predominantly had asymmetric eddies with an area of eddies (W_N/W_P<0.2 and 0<Re<150) and an area of penetrating jets with eddies at low Re and W_N/W_P (Re<150 and 0.22<W_N/W_P<0.5). The mappings of H_A/W_A=1.25 and 1.5 (**Appendix B, Fig. 8.3**) were similar to graphs for H_A/W_A=1; however, asymmetric layered eddies appeared in the H_A/W_A=1.5 flow map over 0<Re<500 at all W_N/W_P ratios. As H_A/W_A was increased to 1.75 (**Fig. 2.5D**), the area on the map of single eddies increased and was independent of Re for W_N/W_P<0.5. An area of penetrating jets with eddies existed for low Re (Re<150) and intermediate W_N/W_P values (0.5<W_N/W_P<1). Asymmetric layered eddies dominated over a large range of Re (0<Re<500) at W_N/W_P>0.4.

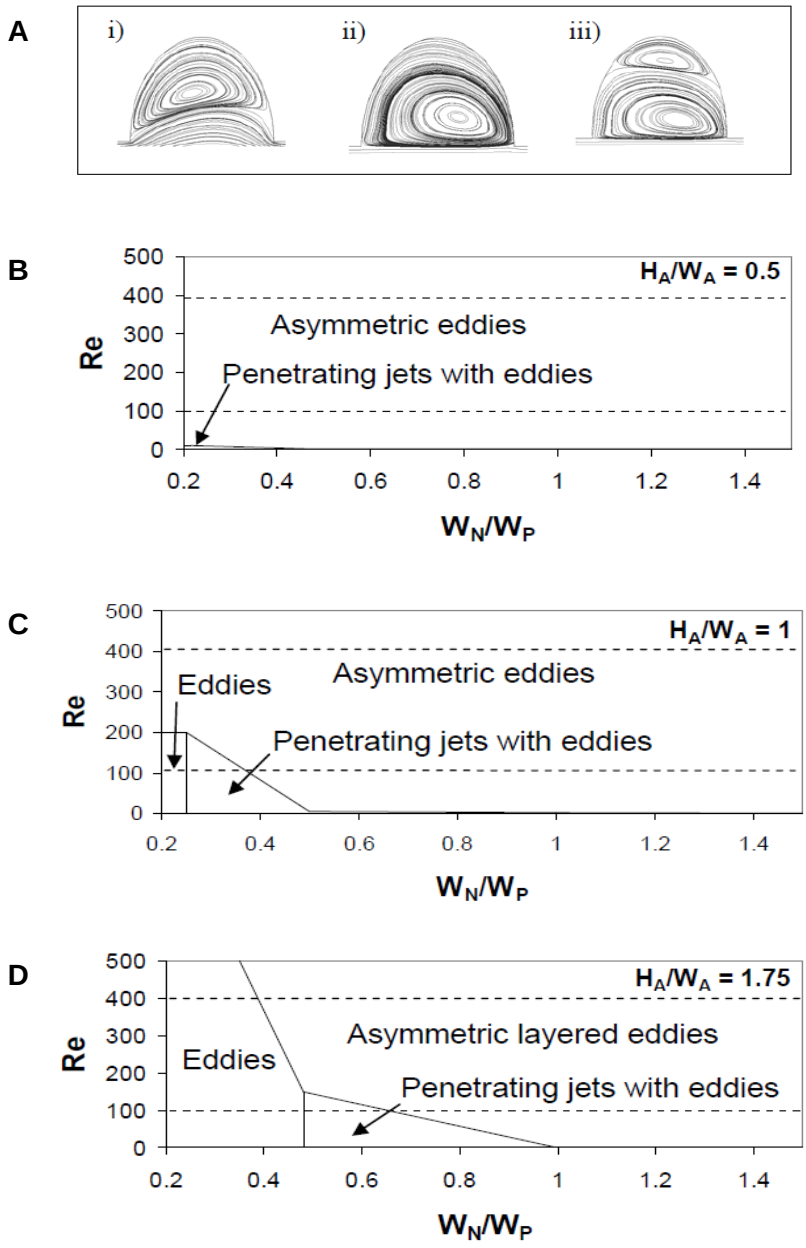

Figure 2.5: Flow mapping of sidewall aneurysms. (A) Characteristic asymmetric flows in sidewall aneurysms: i) Penetrating jets with eddies (Re=5, H_A/W_A=1, W_N/W_P=1.5) ii) Eddies (Re=300, H_A/W_A=1, W_N/W_P=1.5) iii) Layered eddies (Re=500, H_A/W_A=1.5, W_N/W_P=0.5). Flow mapping in terms of various aneurysm height to width (H_A/W_A) ratios, Reynolds numbers (Re), and neck to parent width (W_N/W_P) ratios: (B) H_A/W_A=0.5 (C) H_A/W_A=1 (D) H_A/W_A=1.75. Dashed lines indicate physiological Re.

2.6 Wall Shear Stress Analysis

The WSS profile and corresponding streamlines are shown in **Figure 2.6Ai** for H_A/W_A=1.75, Re=400, and W_N/W_P=1 in a centered aneurysm model. As H_A/W_A increased, the fraction of the aneurysm arc length that experienced low WSS (<0.01 N/m^2) increased (**Fig. 2.6Aii**). The magnitude of the WSS increased with Re and H_A/W_A despite affecting a smaller area. The maximum WSS reached approximately 2 N/m^2 and 23 N/m^2 at Re=100 and 400, respectively, for H_A/W_A=1.75. For constant geometry, the arc length ratio with low WSS decreased with increasing Re (**Fig. 2.6Aii**).

For offset aneurysms, the WSS profiles were asymmetric. **Figure 2.6Bi** illustrates the WSS profile and streamlines for H_A/W_A=1.75, Re=400, and W_N/W_P=1. The WSS was high where the flow impinged upon the aneurysm and decreased significantly along the wall. The maximum WSS for offset aneurysms reached approximately 4.5 N/m^2 and 40 N/m^2 at Re=100 and 400, respectively, for H_A/W_A=1.75, but the increase in low WSS along the aneurysm wall was still apparent as H_A/W_A increased (**Fig. 2.6Bii**). We did not observe a significant difference in the arc length ratio of low WSS at Re=100 and 400 for H_A/W_A=0.5, 1, or 1.75. For H_A/W_A=0.5, the WSS remained above 0.01 N/m^2 and thus was not included in the analysis. Similarly, sidewall aneurysm WSS profiles were asymmetric but had magnitudes greater than 0.01 N/m^2 for the conditions tested (Re=100, 400 and H_A/W_A=0.5, 1, and 1.75). The maximum WSS for sidewall aneurysms reached approximately 9 N/m^2 and 40 N/m^2 at Re=100 and 400, respectively, for H_A/W_A=1.75.

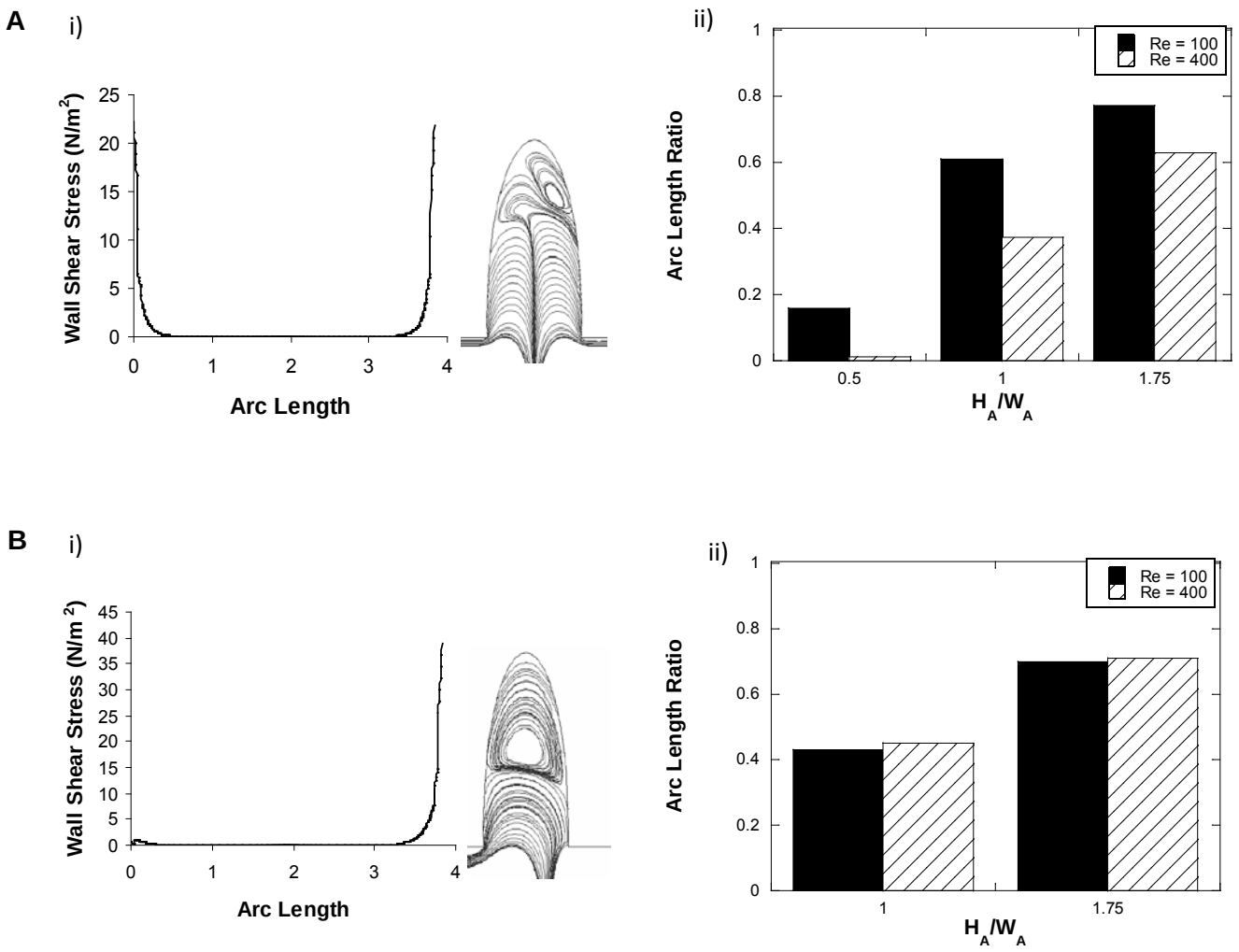

Figure 2.6: Wall shear stress analysis. (A) Centered aneurysms: i) Streamlines and shear stress profile for H_A/W_A=1.75 at Re=400 and W_N/W_P=1 ii) Aneurysm arc length ratio with low shear stress along aneurysm wall. (B) Offset aneurysms: i) Streamlines and shear stress profile for H_A/W_A=1.75 at Re=400 and W_N/W_P=1 ii) Aneurysm arc length ratio with low shear stress along aneurysm wall.

2.7 Discussion

We analyzed how changes in geometry and Re alter hemodynamic profiles in idealized aneurysm geometries and identified transition boundaries where the flow patterns change categorically. These basic flow characterizations may facilitate our understanding of how the hemodynamic landscape and WSS affect complex biological processes [11, 93, 99]. Aneurysm growth and rupture most likely results from a combination of physical and biological phenomena. For example, changes in flow and WSS have been shown to regulate endothelial gene expression [105, 106]. Our systematic mapping and non-dimensional analysis of flow patterns as a function of Re, geometric shape factors, and aneurysm location identify qualitatively when changes in hemodynamics and WSS may occur.

Flow patterns similar to those in our analyses have been reported in the literature [90, 100]. For example, the 2D computational study of Burleson et al. showed an asymmetric eddy profile for a sidewall aneurysm with H_A/W_A=0.925, Re=400, and W_N/W_P=2 [90]. 3D hemodynamic studies showed similarities with our flow patterns as well. Utter and Rossmann showed penetrating bifurcating jets with eddies in their analysis of centered aneurysms with H_A/W_A=1 and W_N/W_P=1 while Hoi et al. found asymmetric eddies in their evaluation of the hemodynamics in sidewall aneurysms with H_A/W_A=1, W_N/W_P=2.5, and Re=136 [92, 107]. Thus, we have shown qualitative agreement between our analysis and other reports.

Unlike other studies that evaluate a limited number of geometries and flow conditions, we have identified common flow patterns and transition boundaries for a broad range of aneurysms. Several aneurysm geometries had flow patterns that are independent of changes in Re. Thus, changes in flow velocity or viscosity did not qualitatively affect hemodynamics. For example, Perktold et al. have found that altering Re from 150 to 250 did not significantly affect

the flow pattern of penetrating bifurcating jets for offset aneurysms with H_A/W_A=1 and W_N/W_P=0.825 [7]. These flow patterns corresponded to our flow map in **Figure 2.4B**. However, in some instances, small changes in Re or geometric shape factors can alter the flow profile. Hoi et al. showed that the impingement area increased significantly as the curvature of the parent artery increased for lateral aneurysms with H_A/W_A=1, W_N/W_P=2.5 and Re=136, causing the flow patterns to change from eddies to penetrating jets with eddies [107]. Our mapping of the hemodynamic landscape recognizes relationships between aneurysm geometry and flow characteristics.

Identifying transitions between regions of different flow patterns may be important in the assessment of treatment of options and predictions of rupture. For centered aneurysms, we observed that for a given Re, the flow profiles evolved from regions of eddies to penetrating bifurcating jets with eddies to asymmetric flows as the neck to parent vessel width (W_N/W_P) ratio increased. Offset aneurysms were dominated by penetrating jets or penetrating jets with eddies. Asymmetric flows or layered eddies were characteristic of sidewall aneurysms. We found that centered aneurysms were more affected by changes in geometry and Re than offset or sidewall aneurysms. Aneurysm location, geometry, and Re dictated the presence of transition boundaries between distinct flow profiles.

In addition to flow patterns, WSS profiles were affected by changes in geometry and Re. We found that deep aneurysms (H_A/W_A>1) had large regions of low WSS and a high magnitude of high WSS for centered aneurysms (**Fig. 2.6A**). Several studies disagree about how the magnitude of WSS relates to aneurysm growth and rupture. In a computational study that modeled patient aneurysms, it was shown that the areas of highest WSS were near the neck of the aneurysm while the shear stress significantly decreased in the aneurysm dome area [11]. The

study concluded that low WSS along the aneurysm wall may facilitate aneurysm growth and rupture while high WSS may contribute to the initial development of an aneurysm. Low WSS along the aneurysm wall has been found to correlate to aneurysm growth and rupture in two independent, patient-specific computational studies [108, 109].

In contrast, some studies have linked high WSS to aneurysm progression [107, 110, 111]. Our analysis showed that the appearance of eddies, which correlated to an increase in H_A/W_A, is accompanied by an increase in areas of low WSS along the aneurysm boundary (**Figs. 2.3, 2.6**). This result could be associated with the finding that increases in H_A/W_A are associated with increased rupture [89]. However, it is possible that changes in the magnitude of WSS along the aneurysm wall contribute to growth and rupture. Nonetheless, WSS appears to play a critical role in predicting aneurysm wall remodeling and rupture.

Flow maps, as we have presented here, may benefit from simulations that capture more of the physiological conditions present within aneurysms. The complexities of fluid flow within aneurysms are not limited to pulsatile flow, elastic walls, and 3D geometry. Though studies have reported similarities between steady vs. pulsatile, rigid vs. compliant, and 2D vs. 3D simulations, future work should accurately and quantitatively validate our assumptions. Our initial study proposes not to quantify exact flow patterns within aneurysms but rather to show that systematic and non-dimensional evaluation of aneurysm hemodynamics is useful in relating common hemodynamic features and identifying transition boundaries between flow patterns. Flow maps that account for physiological phenomena will improve our understanding of how changes in fluid and solid mechanics relate to changes in aneurysm growth and rupture. Our mapping scheme may be useful as an assessment tool and may potentially be used in evaluating aneurysm treatment strategies.

We have systematically examined the hemodynamic and WSS profiles of clinically relevant, idealized aneurysm geometries for a range of physiological Re. Our non-dimensional analysis may be broadly applied to a wide range of patient-specific aneurysms. Our findings indicated an increase in eddies for bifurcating vessels and layered eddies for sidewall vessels for increasing H_A/W_A and W_N/W_P. We demonstrated that small changes in aneurysm geometry or Re can result in distinct changes in the hemodynamic and WSS profiles. This may correlate with changes in cellular function that affect vascular biology and structure leading to aneurysm growth and rupture.

2.8 Experimental Challenges

This aim posed many challenges, including our lack of access to sufficient computing power to conduct in depth 3D simulations. We have started collaborating with Prof. Efthimios Kaxiras, which will allow us to explore how geometry affects aneurysm flow patterns and wall shear stress in 3D. Future experiments will focus on more physiologically relevant aneurysm conditions.

3 COUPLING HEMODYNAMICS AND BIOLOGICAL RESPONSE *IN VITRO*

3.1 Introduction

The vascular endothelium regulates several biological processes essential for immune function, blood flow, and mechanotransduction. Altered hemodynamics is linked to a variety of vascular diseases [112-114]. For example, areas of low shear stress or reversing flow have been associated with the early stages of atherosclerosis and plaque formation [115, 116]. Shear stress has been linked to aneurysm pathophysiology as well [1]. Determining how hemodynamics alters endothelial cell function may be essential for evaluating disease states.

The growth and rupture of cerebral aneurysms may be related to hemodynamics and wall shear stress (WSS). We examined the effect of aneurysm geometry on WSS and the influence of reduced WSS on human aortic endothelial cell (HAEC) monolayers within flow channels since shear stress is often decreased in cerebral aneurysms compared to normal vessels. We measured gene expression patterns of immune regulatory and extracellular matrix (ECM) components 1 and 12 h after exposure to 1 dyne/cm^2 shear. The ECM proteins collagen I (COLI), collagen IV (COLIV), laminin, and fibronectin were visualized by immunostaining HAEC exposed to 0 and 1 dyne/cm^2. We showed that decreased WSS leads to appreciable changes in expression of many genes involved in the inflammatory response and ECM regulation. HAEC regulation of ECM proteins was altered upon experiencing shear stress. Understanding the relationship between hemodynamics, the inflammatory response, and ECM cues may aid in elucidating the pathophysiology of aneurysms.

We also studied the effects of endothelial cell exposure to pro-inflammatory cytokines tumor necrosis factor-α (TNF-α) and interleukin-1α (IL-1α), which are involved in the inflammatory response *in vivo* [117]. We evaluated HAECs and human umbilical vein

endothelial cells (HUVECs). We chose to compare both cell lines as HUVECs are a well-characterized cell line used to study endothelial-leukocyte interactions *in vitro* [118-120].

The rupture of cerebral aneurysms causes stroke, permanent nerve damage, or subarachnoid hemorrhage [2]. Previous studies have found that changes in geometry can greatly affect the hemodynamics within aneurysms [107, 110, 121]. The physical forces exerted on the aneurysm wall may alter the cellular response that could create a vascular microenvironment prone to aneurysm growth and rupture. It has been suggested that evaluating the flow patterns within clinically relevant aneurysm geometries could help predict possible disease outcomes [121]. Indeed, investigating how hemodynamics and the biological responses of the vascular endothelial layer are linked could be beneficial for determining aneurysm pathology and designing new treatments for cerebral aneurysms.

The impact of hemodynamics on cellular function is not fully understood. WSS induces upregulation of endothelial leukocyte adhesion molecule 1 (E-selectin), intercellular adhesion molecule 1 (ICAM1), vascular cell adhesion molecule 1 (VCAM1), thrombomodulin, and ECM components including COLIV and laminin [30, 32, 115, 122, 123]. However, the cellular response to abrupt changes in WSS has not been assessed thoroughly.

Vessel structure and compliance are regulated by a balance of ECM synthesis, degradation, and remodeling [124]. Degradation of ECM components and remodeling in the aneurysm wall characterizes the development of vascular diseases such as atherosclerosis, abdominal aortic aneurysm, and cerebral aneurysm growth [26, 125]. Specifically, matrix metalloproteinases (MMPs), which are involved in the remodeling of vascular walls such as MMP2 and MMP9, have been linked to cerebral aneurysm progression. Additionally, *in vivo*

canine models of aneurysm formation describe the contribution of altered hemodynamics to the remodeling of the vascular wall, which include disruption of the internal elastic lamina, loss of fibronectin, and reduction of smooth muscle cells [93]. Thus, changes in hemodynamics could impact cell function, which may also play a role in aneurysm growth and rupture.

Aneurysm geometry has been implicated in rupture [89], and changes in geometry alter flow patterns within aneurysms. As a result, the relationship between flow patterns and shear stress along the aneurysm wall was analyzed, which may impact vascular biology. In this study, we investigated how WSS is affected by flow pattern transitions and determined gene expression profiles upon abrupt changes in WSS. The effect of shear stress on ECM components was evaluated. Finally, we determined how the expression of cell adhesion molecules (CAMs) on ECs was affected by inflammatory cytokines through the evaluation of gene expression and cell surface protein expression.

3.2 Methods and Materials

Computational Model

We used the COMSOL 3.3 Multiphysics finite-element software to solve the Navier-Stokes (Eq. 2.2) and continuity (Eq. 2.3) equations assuming incompressible flow of a Newtonian fluid. We used typical values for blood density and viscosity (1060 kg/m^3 and 3 cP, respectively [95, 96]). We assumed 2D, steady ($\frac{\partial \boldsymbol{u}}{\partial t} = 0$), laminar flow in a rigid-wall model of a vessel, and the no slip condition was applied [7, 92, 97]. A fine mesh with a minimum of 7,400 elements was used to resolve the geometries.

We varied the aneurysm neck to parent vessel ratio (aneurysm neck width/parent vessel width, W_N/W_P) while keeping the height to width ratio (aneurysm height/aneurysm width, H_A/W_A) constant. We varied the Reynolds number (Re), the non-dimensional ratio of inertial to viscous forces (Eq. 2.1). **Figure 2.1A** depicts the aneurysm geometry used in these simulations.

WSS profiles were calculated along the aneurysm boundary arc length for varying W_N/W_P (0.25-1.5) and Re (50 and 200). These geometries and Re were chosen because of observed transitions in flow patterns in these areas (**Fig. 2.3B**). We present these results through the arc length ratio, by which we denote the fraction of the arc length that experienced WSS < 0.01 N/m^2. The results utilize an arc length which is non-dimensionalized by the parent vessel width.

ECM Regulation

Confluent monolayers of HAECs (Lonza Walkersville, Walkersville, MD, USA) were grown at 37^oC with 5% CO_2 in a humidified chamber in flow channels made from polydimethyl siloxane (PDMS; Sylgard® 184 Silicone Elastomer Kit) in a 10:1 (w/w) base to curing agent ratio bonded to glass. Channels were 70 mm long x 7.5 mm wide x 1.6 mm high. Endothelial Cell Growth Medium-2 (EGM-2; Lonza, Basel, Switzerland) with either 0 or 2% fetal bovine serum (FBS) was flowed into the channels at Re=66 using a peristaltic pump (AC-2110 Perista Pump, ATTO Corporation, Tokyo, Japan), causing the cells to experience a WSS of 1 dyne/cm^2 for 12 h. The outlet stream was fed into a 0.22 μm cellulose acetate filter unit (Corning Life Sciences, Lowell, MA, USA) to avoid contamination. Cells experiencing no flow were incubated with media containing either 0 or 2% FBS for 12 h. Cells were fixed with 4% formaldehyde and blocked with 1% bovine serum albumin (BSA) in phosphate buffered saline (PBS). Cells were then stained with mouse anti-human COLI or COLIV IgG_1 (Sigma-Aldrich, St. Louis, MO,

USA) or rabbit anti-human laminin or fibronectin IgG (Sigma-Aldrich). Secondary staining was done with goat anti-mouse IgG_1 conjugated to fluorescein isothiocyanate (FITC, Caltag Laboratories, Burlingame, CA, USA) or goat anti-rabbit IgG conjugated to Texas Red (Invitrogen, Carlsbad, CA, USA) followed by a Hoechst 33342 (Invitrogen) nuclear stain. Glass coverslips were also incubated with media (0 or 2% FBS) only for 12 h and staining as described.

Gene Expression

Cells were sheared in the manner described above for 4 h at 1 dyne/cm^2 with media containing 2% FBS. Total RNA was isolated from cells using a Qiagen RNeasy Mini Kit following the manufacturer's procedures (Qiagen, Valencia, CA, USA). The cells were either lysed immediately after flow or lysed after 1 or 12 h of static incubation after flow. The control cell population experienced no flow. Quantitative reverse transcriptase polymerase chain reaction (qRT-PCR) was performed on a 7300 real-time PCR system using the Taqman method (Applied Biosystems, Carlsbad, CA, USA). We evaluated the regulation of a variety of genes involved in tissue injury and remodeling: E-selectin, ICAM1, VCAM1, platelet endothelial cell adhesion molecule 1 (PECAM1), type I collagen (COLI), COLIV, MMP2, and MMP9. Glyceraldehyde 3-phosphate dehydrogenase (GAPDH) was used as the endogenous control. All primers were obtained from Applied Biosystems.

HAECs or HUVECs were seeded in 12 well plates and grown to confluence in EGM-2 media with 2% FBS. Cells were treated with 1, 10, or 25 ng/mL of TNF-α (Sigma Aldrich) or IL-1α (R&D Systems, Minneapolis, MN, USA) at 1, 5, or 10 ng/mL for 2, 4, 6, 12, or 24 h. Experiments were done in triplicate, and controls were performed with no cytokine treatment. Again, cells were lysed, RNA was extracted and converted to cDNA, and qRT-PCR was

performed. An endogenous control of GAPDH was used, and evauations were done in triplicate. Relative expression levels of E-selectin and VCAM1 were assessed.

Flow Cytometry

VCAM1 and E-selectin expression by ECs was evaluated by flow cytometry after 1, 6, 12, and 24 h incubations with either IL-1α (5 ng/mL) or TNF-α (20 ng/mL) [85]. Quantification of the density of molecules on the surface was done using Quantum™ Simply Cellular® microbeads. After ECs were activated with IL-1α or TNF-α, 10^6 cells were collected from a 6-well plate, spun down, and resuspended with ice cold 1% BSA. ECs were rinsed 3 times through suspension-spin cycles and blocked with 1% BSA in PBS for 30 min in an ice bath. ECs were incubated with mouse anti-human VCAM1 and sheep anti-human E-selectin monoclonal antibodies (1 mL, 10 ng/mL) for 30 min in an ice bath. After rinsing with 1% BSA three times to remove free antibodies, ECs were stained with FITC-conjugated goat anti-mouse and tetramethylrhodamine isothiocyanate (TRITC)-conjugated rabbit anti-sheep secondary antibodies for 30 min in an ice bath. ECs were finally rinsed with 1% BSA three times, resuspended in PBS, and analyzed by flow cytometry.

3.3 Hemodynamic Analysis

Three characteristic flow patterns were found upon altering aneurysm geometry (**Fig. 2.2**): eddies, penetrating bifurcating jets with eddies, and asymmetric bifurcating jets. **Fig. 2.3B** shows the characteristic flow map based on Re and W_N/W_P ratio at a constant $H_A/W_A=1$. The presence of eddies was shown at low Re (<100) and low W_N/W_P (<0.5). Penetrating bifurcating jets with eddies were found between $100<Re<300$ for $W_N/W_P<0.5$ and at low Re for all other W_N/W_P ratios. Asymmetric bifurcating jets dominated at large Re and W_N/W_P ratios.

The shear stress along the aneurysm arc length was analyzed over areas where flow pattern transitions occurred. The flow patterns were found to transition from eddies to penetrating bifurcating jets with eddies to asymmetric bifurcating jets at Re=50 and from penetrating bifurcating jets with eddies to asymmetric bifurcating jets at Re=200 upon increasing W_N/W_P. As the W_N/W_P ratioincreased at a constant $H_A/W_A=1$, representing a widening of the aneurysm, the percentage of the aneurysm arc length that experienced low WSS decreased (**Fig. 3.1**). In addition, as Re increased from 50 to 200, the arc length that experienced low WSS decreased. Aneurysms with the lowest Re and W_N/W_P ratios had the highest incidence of low WSS along the arc length.

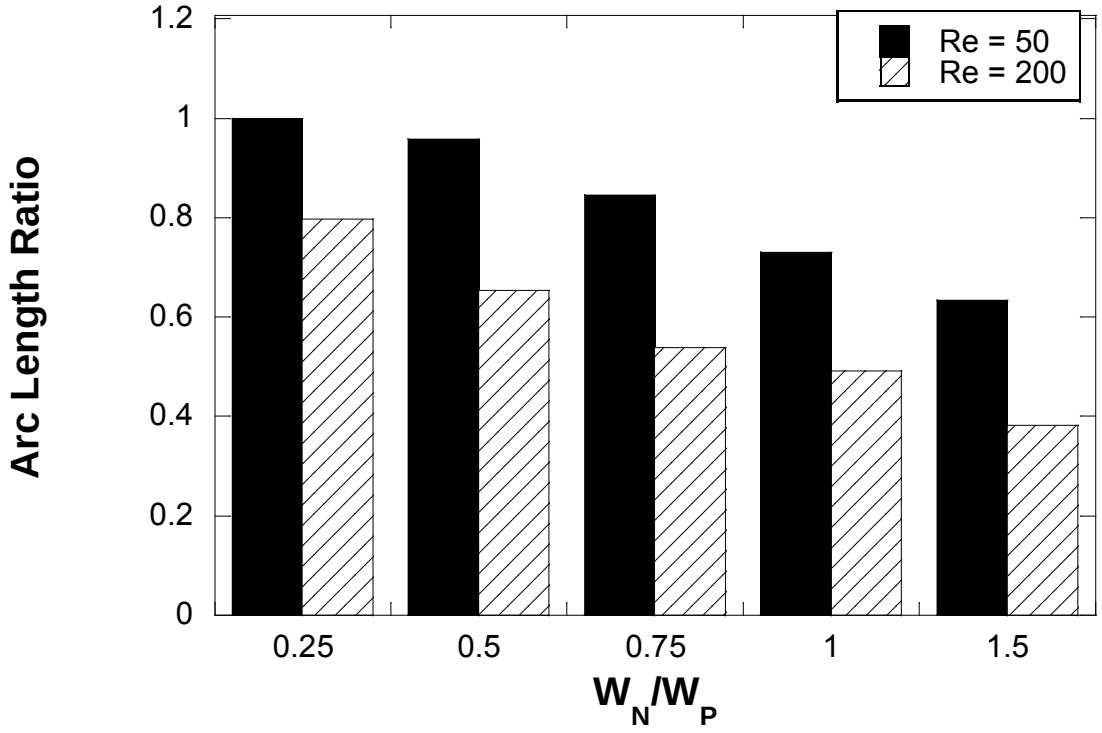

Figure 3.1: Low wall shear stress analysis. $H_A/W_A=1$ and varying Re and W_N/W_P.

3.4 Modulating Endothelial Cell Gene Expression with Shear Stress

We showed how changes in shear stress can alter the expression of HAEC inflammatory (**Fig. 3.2A**) and ECM regulative (**Fig. 3.2B**) genes. Appreciable differences in gene expression were found when cells were lysed immediately after steady shear or waiting 1 or 12 h. The expression of E-selectin and ICAM1 decreased significantly after 12 h, while VCAM1 showed a decrease in expression after waiting only 1 h (**Fig. 3.2A**). The expression of PECAM1 remained constant. Although the shear stress of 1 dyne/cm^2 was well below the physiological value of approximately 36 dyne/cm^2 in cerebral vessels [11], E-selectin was upregulated by approximately 20 times compared to the no flow condition and 40 times greater than waiting 12 h after shear. COLIV increased in expression after 1 h while decreasing again after 12 h, and MMP2 increased in expression after 1 h and remained high after 12 h (**Fig. 3.2B**). The expression of COLI decreased slightly after 1 h, and MMP9 levels remained relatively constant.

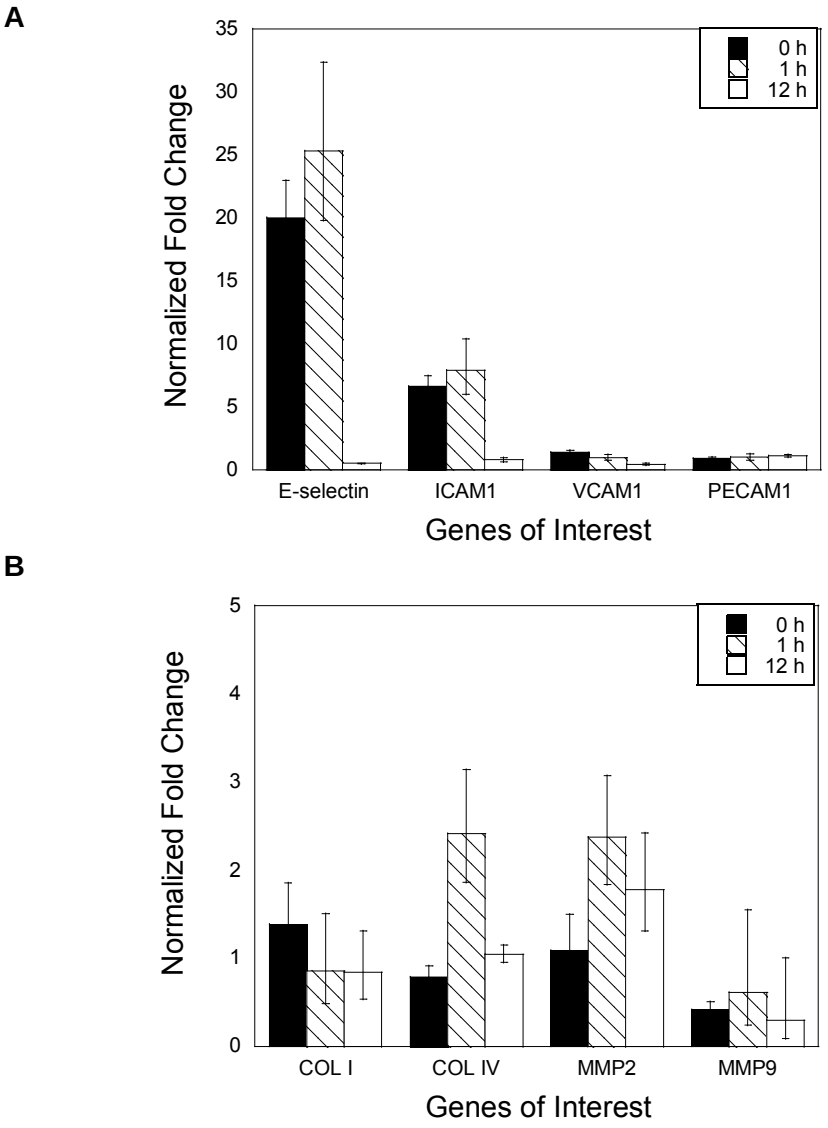

Figure 3.2: Gene expression profiles of ECs upon changing shear stress. (A) Inflammatory and (B) ECM gene expression from qRT-PCR on HAEC after 4 h of shear stress at 1 dyne/cm^2. Solid bars correspond to cells lysed immediately after flow, diagonal lines to lysing cells after 1 h, and white bars to lysing cells 12 h after flow. Normalized fold change represents the proportional change in expression compared to the no flow condition. Gene abbreviations: E-selectin, ICAM1, PECAM1, VCAM1, COLI, COLIV, MMP2, and MMP9.

3.5 The Effect of Shear Stress on ECM Regulation

We have evaluated the HAEC expression of the ECM components COLI, COLIV, laminin, and fibronectin after being exposed to shear stress (**Fig. 3.3**). After 12 h of steady shear with media containing serum, cell morphology was elongated compared to the cells experiencing no flow. COLI was expressed highly after flow, while the fibronectin network appeared more extended along the cell membrane. Laminin expression increased along the cell membrane after shearing compared to the static condition where it was concentrated around the nucleus. COLIV was expressed across the membrane before and after flow.

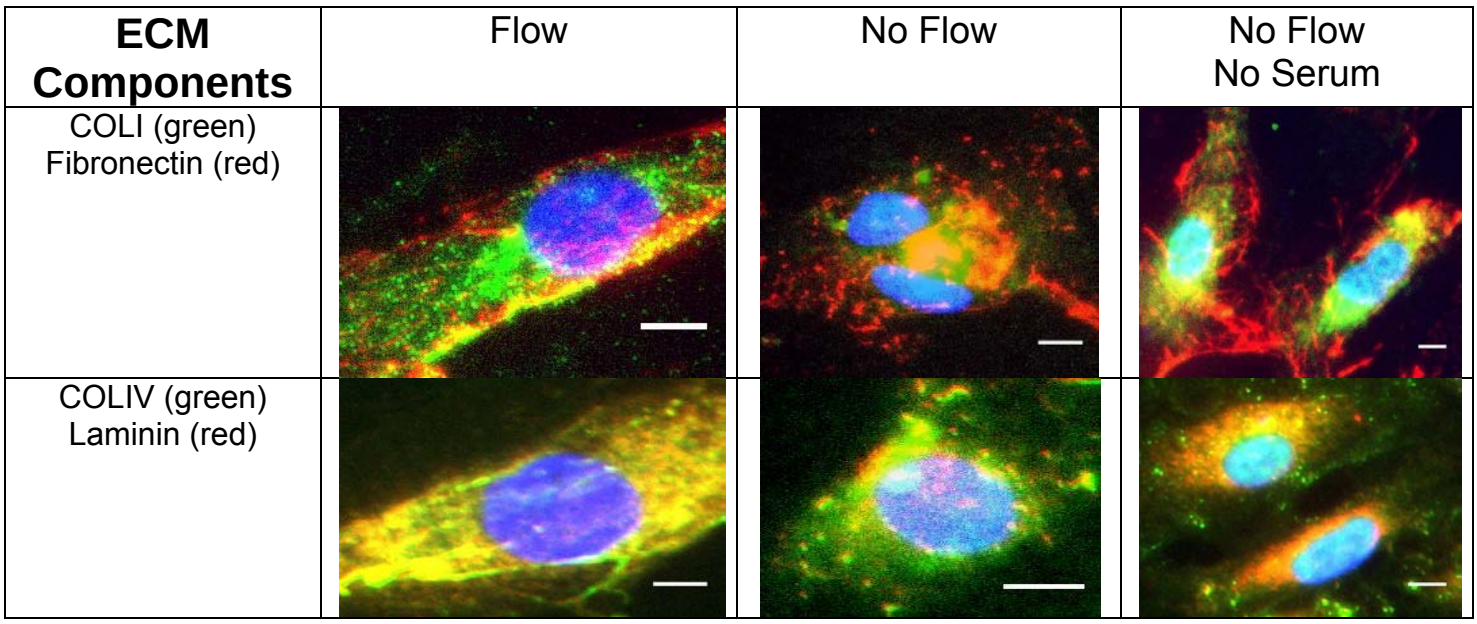

Figure 3.3: Immunofluorescence staining of HAECs after shear. HAECs stained for COLI, COLIV, fibronectin, and laminin after 12 h shear at 1 dyne/cm^2 or no shear. Nuclear stain is shown in blue. Scale bar is 25 μm.

The ECM components of the cells incubated without serum under no shear were comparable to the serum condition: strong fibronectin and faint COLI expression across the cell membrane, concentrated laminin around the nucleus, and diffuse COLIV across the membrane. Control glass coverslips incubated only with media exhibited no ECM staining as expected.

3.6 VCAM1 and E-selectin Expression under Inflammatory Conditions

In line with previous studies looking at the effects of infllammatory cytokines *in vitro,* we evaluated the effects of stimulation of ECs with 1-10 ng/mL and 1-25 ng/mL for IL-1α and TNF-α, respectively [86, 126-129]. The results are shown in **Figures 3.4-3.6** below. In HAECs, expression of VCAM1, ICAM1, E-selectin was maximized upon treatment with 10 ng/mL TNF-α for 4 h. The highest upregulation of VCAM1, ICAM1, and E-selectin on HUVECs occurred at 25 ng/mL and 24 h of TNF-α stimulation. Stimulation with 5 ng/mL IL-1α for 6 h provided the highest upregulation of all molecules. HUVEC gene expression levels exceeded HAEC levels in magnitude. Because ICAM1 had the lowest expression levels for all cell lines and treatments, we proceeded in quantifying only VCAM1 and E-selectin surface markers in the flow cytometry experiments.

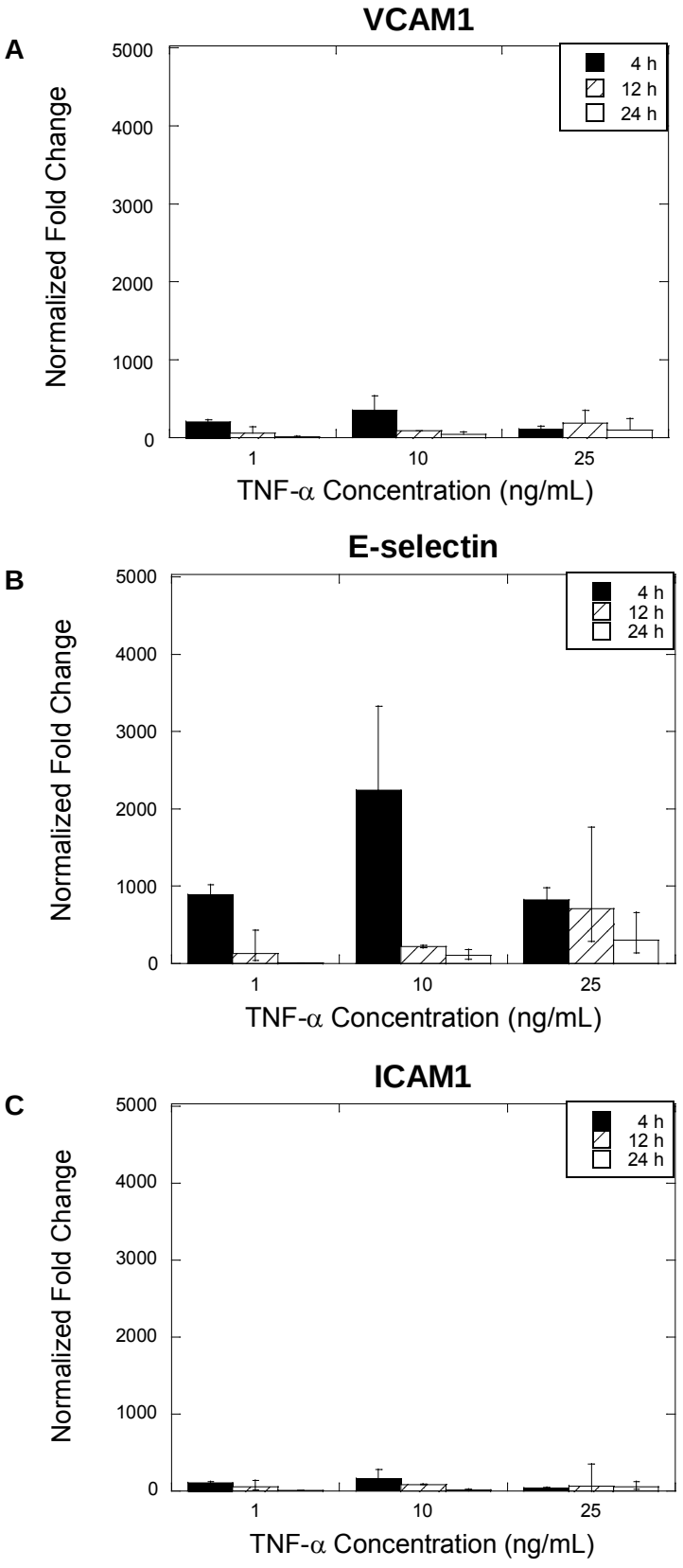

Figure 3.4: HAEC gene expression profiles after exposure to TNF-α. Profiles for (A) VCAM1, (B), E-selectin, and (C) ICAM1 after treatment with 1-25 ng/mL TNF-α for 4-24 h.

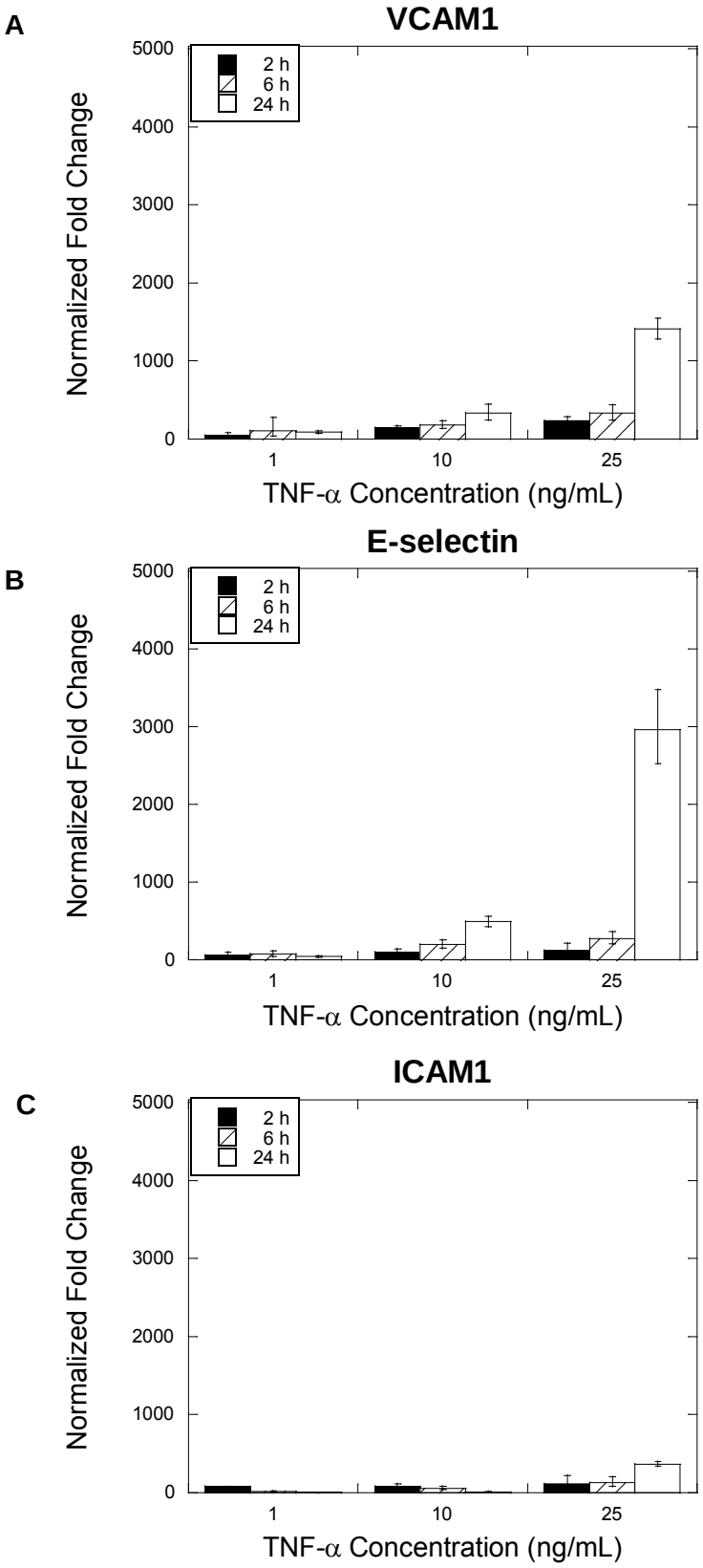

Figure 3.5: HUVEC gene expression profiles after exposure to TNF-α. Profiles for (A) VCAM1, (B), E-selectin, and (C) ICAM1 after treatment with 1-25 ng/mL TNF-α for 4-24 h.

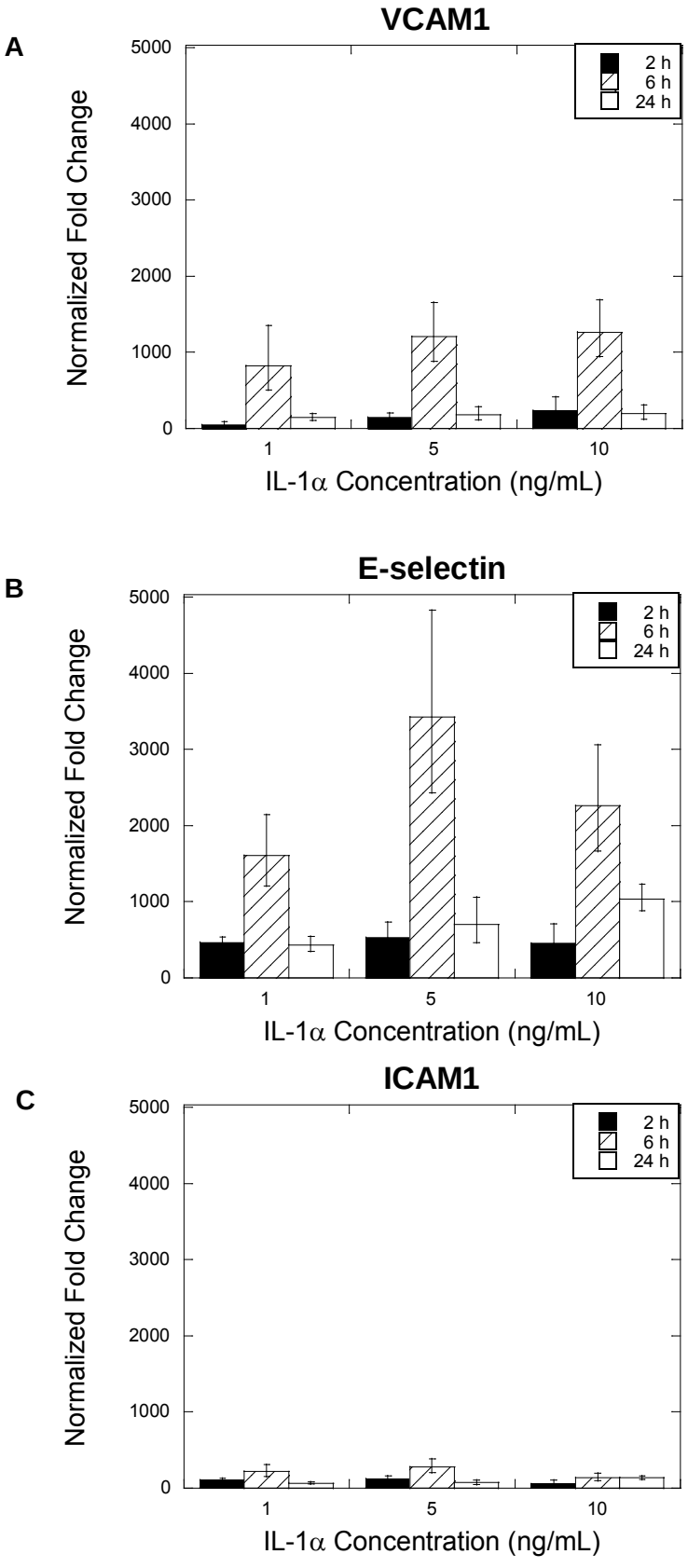

Figure 3.6: HUVEC gene expression profiles after exposure to IL-1α. Profiles for (A) VCAM1, (B), E-selectin, and (C) ICAM1 after treatment with 1-10 ng/mL IL-1α for 2-24 h.

Surface expression of VCAM1 and E-selectin on HUVECs was similar after treatment with either IL-1α and TNF-α (**Fig. 3.7**) [85]. VCAM1 expression increased and reached a saturation point after 24 h while E-selectin expression peaked at 6 h and subsequently decreased over time.

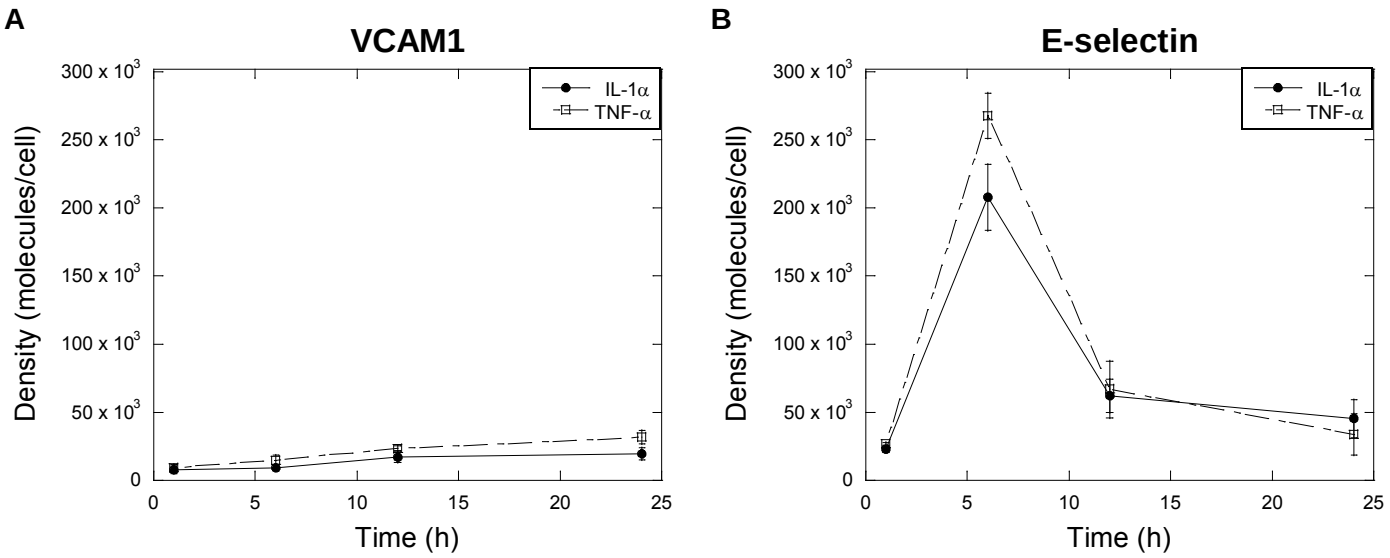

Figure 3.7: Expression of VCAM1 and E-selectin on TNF-α and IL-1α activated HUVECs. Expression of VCAM1 (A) and E-selectin (B) is determined using flow cytometry as a function of time. Error reported is standard error with n = 3.

3.7 Discussion

We have shown the effect of abrupt decreases in WSS on gene expression and ECM deposition. Changes in flow patterns within aneurysm geometries may lead to considerable biological changes regarding shear stress, gene expression, and ECM surface expression. We sheared HAECs within flow channels and treated HAECs and HUVECs with inflammatory cytokines to understand how these factors would affect gene expression. We used flow to determine the effect of constant shear on the ECM.

We examined the effect of flow pattern transitions within different aneurysm geometries on shear stress along the aneurysm wall (**Fig. 3.1**). We determined that decreasing the W_N/W_P, which narrows an aneurysm, led to increasing areas of low WSS on the arc length. WSS has been linked to aneurysm pathophysiology, but its direct role is unclear [1]. For example, low magnitude WSS has been linked to aneurysm growth and rupture [11, 108, 109]. However, high shear has been correlated to aneurysm growth [107, 110, 111]. Though there are competing theories about how aneurysms rupture, shear stress most likely plays a part in aneurysm progression.

We assessed effect of decreasing WSS on HAEC gene expression (**Fig. 3.2**). WSS was abruptly decreased to mimic the aneurysm environment, where the growth of an aneurysm leads to decreased flow and WSS. Physiological shear stress in arteries can vary between approximately 10-20 dyne/cm^2 [130]. The WSS within aneurysms is variable both spatially and in terms of magnitude; WSS in aneurysms has been estimated in the range of 1-35 dyne/cm^2 [11]. Changes in VCAM1, ICAM1, COLIV, and MMP2 have previously been implicated in aneurysm pathophysiology [69, 131-133]. Even at the low WSS of 1 dyne/cm^2, significant changes are observed in the regulation of gene expression in HAECs. E-selectin and ICAM1, adhesion molecules involved in the inflammatory response, increased after 1 h of static incubation following 4 h shear at 1 dyne/cm^2. Expression of E-selectin and ICAM1 have been found to increase in the cerebrospinal fluid after aneurysm rupture [134]. Although VCAM1 decreased after static incubation in our study, *in vivo* studies suggest that higher levels of VCAM1 are found in aneurysms compared to normal vessels [69, 134]. This discrepancy could be due to the presence of immunological factors and cells recruited *in vivo*. Nevertheless, the

inflammatory response is significant in the progression of aneurysms, and decreases in shear may be involved in creating an aneurysm environment susceptible to rupture.

With regards to ECM regulatory gene expression, stopping flow after 4 h shear at 1 dyne/cm^2 for 1 or 12 h decreased COLI expression. This correlates with the reduction of COLI levels observed in cerebral aneurysms [135]. After decreasing shear for 1 h, expression of COLIV increased; this pattern has similarly been observed in human cerebral aneurysms after surgery [136]. An increase in COLIV may cause vessels to increase in stiffness and could lead to higher susceptibility of rupture [137]. MMP2 levels increased in comparison to the gene expression immediately after shear, which relates to previous findings of increased levels of MMP2 in aneurysms [133]. Expression of MMP9 did not increase after decreasing shear stress in our study. This might be explained by the fact that the *in vivo* response requires immune cells to release MMP9 into the aneurysm cavity [26]; such cells were not present in our experiments.

Other studies have examined the effect of altered or disturbed flow on EC gene expression [106, 138]. For example, a step-flow chamber was used to probe the effects of disturbed flow on bovine aortic ECs [139]. This study showed that disturbed flow at 12 dyne/cm^2 caused sustained activation of a transcription factor involved in biosynthesis of cholesterol, sterol regulatory element binding protein, while steady, laminar shearing produced a transient response. These studies suggest that altered flow, and consequently altered WSS, within aneurysms can lead to significant biological changes.

We additionally evaluated how the presence or absence of WSS can affect ECM regulation (**Fig. 3.3**). Aneurysm occurrence and growth has been shown to be affected by matrix remodeling events that alter or degrade the ECM [133]. COLI expression increased in HAECs

after 12 h sustained shear compared to the cells experiencing no flow, which did not correlate with the decreased biosynthesis of COLI observed in our altered shear experiment or *in vivo* studies [135]. Fibronectin, which has been implicated in aneurysm repair, was found to change expression patterns by stretching with the elongated cell after the cell experienced shear stress [140]. Cells starved from serum after 12 h shear did not remain fully attached to the glass substrate and did not retain an elongated morphology. The differences found in ECM expression after constant shearing compared to conditions of altered shear suggest that the changes in WSS experienced within aneurysms could have distinct effects on cellular gene and protein expression. It is also possible that gene expression of ECM components does not correlate with ECM regulation. Further experiments exploring the differences between gene expression and protein regulation would be beneficial for understanding aneurysm remodeling events.

We have shown how decreasing shear stress affects EC gene expression and ECM regulation. A decrease in WSS led to considerable changes in inflammatory and ECM regulatory gene expression, which correlates with *in vivo* studies. ECM regulation was altered by low shear stress. The interplay between hemodynamics, shear, and biological response may dictate aneurysm pathophysiology. This work demonstrates how aneurysm growth, which reflects modifications in shear stress along the aneurysm wall, can potentially lead to appreciable biological changes.

The cytokines IL-1α and TNF-α play an important role in the progression of inflammation and injury. Patterson et al. suggest that TNF-α activation provides a close representation of CAM changes associated with dysfunctional endothelium [141], and TNF-α has been shown to increase endothelial permeability and cause cytoskeletal reorganization [142]. IL-1α increases expression of CAMs, activates EC and smooth muscle cell proliferation,

activates macrophage infiltration, increases vascular permeability, and contributes to EC dysfunction by stimulating the creation of deleterious reactive oxygen and nitrogen species [143]. We have shown the influence of the concentration and treatment time of these cytokines on CAM gene and protein expression.

There are limitations associated with this aim. First, we chose to change shear stress temporally rather than spatially. *In vivo*, aneurysm growth causes spatial changes in shear stress due to changes in hemodynamics. We could have more closely modeled the aneurysm environment by shearing ECs in a construct with angled edges to create spatial changes in shear. Nonetheless, we found that an abrupt, slight change in shear from 1 to 0 dyne/cm^2 causes discernible differences in gene expression. We do not claim that this experimental set-up recapitulates the aneurysm environment; however, these results have implications for aneurysm pathophysiology since we have shown the importance of changing shear with respect to gene expression. In addition, we treated ECs with inflammatory cytokines to recapitulate an acute immune response. ECs within aneurysms *in vivo* most likely exhibit varying expression profiles from what is shown *in vitro*. However, we will use the information gained in this aim as a basic model for targeting ECs with biomaterials. Future studies should take these factors into account for a more realistic model system.

The results from this aim have determined how we proceeded in stimulating ECs in future experiments to design biomaterials for EC adhesion. Because the aneurysm environment is considered inflammatory and gene expression is higher on ECs exposed to inflammatory cytokines (**Figs. 3.4-3.7**) rather than those exposed to shear, we will continue to activate ECs by simulating inflammatory events. We will use HUVECs in all further experiments due to their higher levels of gene expression as compared to HAECs, which would allow for easier targeting

of inflamed cells. IL-1α will be used as the main agent for simulating inflammation. This is due to the fact that the qRT-PCR results derived after IL-1α stimulation followed our flow cytometry results, indicating that gene expression and cell surface protein expression were similar. Since expression of VCAM1 and E-selectin were maximized with 5 ng/mL IL-1α treatment after 6 h at much higher magnitudes than ICAM1, we will target only VCAM1 and E-selectin using this activation protocol for all subsequent experiments.

3.8 Experimental Challenges

Completing this section posed many experimental challenges, especially in regards to the shear stress experiments. During the flow experiments, contamination within the channels was a major obstacle. Despite use of extensive sterilization procedures, including autoclaving, UV sterilization, ethanol sterilization, and filtration, contamination occurred at a high frequency. However, we were able to complete enough experiments without contamination for evaluation of gene expression. This is one reason we shifted our focus toward assessing inflammatory environments. To combat contamination in flow experiments in the future, we may attempt to use all glass channels rather than PDMS/glass constructs, and we may consider using tubing that is more resistant to contamination.

There were further limitations in the magnitude of shear stress that could be achieved with our flow pump, which is why we only evaluated the effects of a shear stress of 1 dyne/cm^2. We have since acquired a flow apparatus capable of higher flow rates and may explore higher shear stresses in future experiments. In addition, we may consider using microfluidic channels to achieve increased shear stresses.

4 POLYVINYL ALCOHOL HYDROGELS

4.1 Introduction

Adhesion is an important regulator of cell proliferation, migration, apoptosis, and differentiation [144]. Previous research has demonstrated that adhesion is dependent on matrix chemistry and stiffness. For example, cell adhesion and migration is influenced by varying the density of cell adhesion peptides on surfaces [145], and cell spreading and density is regulated by material stiffness [146-148]. Matrix stiffness is also observed to direct human mesenchymal stem cell differentiation toward neurogenic, myogenic, or osteogenic commitment [149]. Previous reports have tailored adhesion by adjusting a single parameter. In contrast, biology utilizes multiple cues to regulate cell behavior.

Leukocyte-EC adhesion is regulated via multiple interactions between cell adhesion molecules (CAMs), such as vascular cell adhesion molecule-1 (VCAM1) and endothelial leukocyte adhesion molecule-1 (E-selectin), and their binding ligands. Their role in leukocyte rolling, adhesion, and transmigration has been elucidated [150]. Antibodies that target CAMs have been used to modify drug delivery vehicles [151] or surfaces [152] to target inflamed ECs and cancer cells, respectively.

We have recently exploited the use of multiple CAMs on drug delivery vehicles that exhibited synergistic adhesion in targeted drug delivery [85-87]. Increased vehicle-cell binding was achieved at optimal anti-VCAM1:anti-E-selectin ratios that complemented cytokine-activated EC surface expression. Cytokine-activated CAM expression is essential in harnessing the immune response; dysfunction of this response can lead to diseased states, such as atherosclerosis [153], ischemic cerebrovascular disease [154], cerebral aneurysms [69], and rheumatoid arthritis [155].

We hypothesized that cell adhesion could be engineered via modification of hydrogel surface chemistry and elasticity. Polyvinyl alcohol (PVA) was chosen because it is non-degradable, non-adhesive, and can easily be modified [156]. We mimicked adhesive interactions between cells via the presentation of antibodies that bind VCAM1 and E-selectin on PVA hydrogels. We additionally investigated the effect of surface elasticity on cell adhesion by varying the methacrylate content of PVA gels. Understanding how to engineer cell adhesion is a fundamental problem in the development of materials for vascular remodeling.

4.2 Methods and Materials

Materials

PVA (MW 31 kDa, 88% hydrolyzed), dimethyl sulfoxide (DMSO), 2-isocyanoethylmethacrylate (2-ICEMA), 2,6-di-tert-butyl-4-methylphenol (DTBMP), 4-aminobutyraldehyde diethyl acetal (4-ABA), hydrochloric acid (HCl), ammonium hydroxide (NH_4OH), *N*-(3-Dimethylaminopropyl)-*N′*-ethylcarbodiimide hydrochloride (EDC), N-hydroxysulfosuccinimide (sulfo-NHS), 2-(N-morpholino)ethanesulfonic acid hydrate (MES), and sodium chloride (NaCl) were purchased from Sigma Aldrich (St. Louis, MO). Irgacure 2959 was purchased from Ciba Specialty Chemicals (Basel, Switzerland). Deuterium oxide (D_2O) was purchased from Cambridge Isotope Laboratories (Andover, MA). Hank's Balanced Salt Solution (HBSS) and phosphate buffered saline (PBS) were purchased from Invitrogen (Carlsbad, CA).

Methacrylated, Aminated PVA Synthesis

PVA was dissolved in DMSO in a 20% w/v solution at 60^{o}C [157]. The solution was purged with N_2 (g) for 30 min. 1, 2, 5, or 10 mol% of 2-ICEMA was added dropwise. 1%

DTBMP was added to inhibit polymerization of methacrylates. The reaction was kept at 60^{o}C for 4 h. The methacrylated PVA was precipitated in acetone and collected and dried under vacuum.

Methacrylated PVA was aminated using a method previously described [156, 158]. Briefly, a 12% w/v solution of methacrylated PVA was dissolved in water at 40^{o}C. 4-ABA was added dropwise to a final concentration of 10 mol% for all formulations. HCl was then added dropwise to the solution to bring the pH down below 1, and the reaction was continued for 30 min. The pH was then increased rapidly to 8.0 with NH_4OH, and the final solution was dialyzed (MWCO 2000) and lyophilized.

^{1}H nuclear magnetic resonance (NMR) spectroscopy was performed to confirm the successful conjugation of methacrylate and amine groups to the PVA backbone. Specifically, samples were dissolved in D_2O and spectra were obtained using a Varian M300 Spectrometer.

Hydrogel Fabrication

Aminated, methacrylated PVA solutions were made at 10-30% w/v in water with 0.75% Irgacure2959 photoinitiator. Solutions were exposed to UV light (21.7 mW/cm^{2}, 365 nm) for 90 sec, resulting in hydrogels. Hydrogels were synthesized either in Teflon molds (10 mm × 1 mm × 30 mm) for use in mechanical studies or in well plates and then cut to an appropriate size using a cork borer for use in cell studies.

Mechanical Properties

The Young's moduli of various hydrogel formulations were determined using an Instron BioPuls machine (Instron, Norwood, MA). Hydrogels (10 mm × 1 mm × 30 mm) were extended at a rate of 1 mm/min at room temperature immediately after polymerization. Swelling properties

were evaluated as well. Hydrogels were swollen in HBSS to equilibrium. Mass swelling ratios (Q) were calculated by $Q = W_S / W_D$, where W_S and W_D are the masses of the swollen and dry hydrogels, respectively.

Cell Culture

Human umbilical vein endothelial cells (Lonza, Walkersville, MD) were cultured in Endothelial Cell Growth Medium-2 (EGM-2; Lonza). ECs were maintained at 37^{o}C with 5% CO_2 in a humidified incubator and grown to confluence before seeding onto hydrogels or 12 well plates for gene expression studies. All hydrogel formulations used with cells were 20% w/v solutions of the precursor methacrylated and aminated PVA.

Covalent Surface Modification of Hydrogels

Primary monoclonal mouse anti-human antibodies (R&D Systems, Minneapolis, MN) were activated for conjugation to the amine group on synthesized precursor hydrogels using 2 mM EDC and 5 mM sulfo-NHS in 50 mM MES buffer (pH 6.0, 0.5 M NaCl) for 1 h at room temperature [159, 160]. An arginine-glycine-aspartic acid (RGD)-containing peptide (arginine-glycine-aspartic acid-serine, Tocris Bioscience, Ellisville, MO), anti-E-selectin (R&D Systems) antibody only, anti-VCAM1 (R&D Systems) antibody only, or a 1:1 ratio of anti-VCAM1:anti-E-selectin were added at a total of 0.5 mg antibody/g amine group on the PVA backbone to the EDC/sulfo-NHS solution [161]. Hydrogels were added to the solution and allowed to react at 4ºC overnight. Gels were rinsed with PBS before use to remove excess reactants.

Cell Staining

ECs were activated for 6 h with 5 ng/mL IL-1α and then seeded onto PVA-2 gels (20% w/v). After a 24 h incubation, cells were fixed in cold acetone for 5 min at -20^{o}C. Nuclear and F-actin stains were performed by concurrent addition of 0.2 μg/mL 4',6-diamidino-2-phenylindole dihydrochloride (DAPI; Millipore, Billerica, MA) and 0.33 μM Alexa Fluor 546 phalloidin (Invitrogen) to cells for 1 h at room temperature. Fluorescent images were acquired using confocal microscopy (Zeiss LSM 510 META).

Centrifugation Assay

Adhesion of cells onto hydrogels was assessed using a centrifugation assay adapted from previously described methods [162-164]. Gels were seeded with 0.5×10^6 activated ECs per gel for 24 h. Gels undergoing centrifugation were placed in 24 well plates filled completely with media in order to avoid the possibly deleterious effects of air bubble formation on cell retention. Plates were sealed with Titer-Top Plate Sealant (Electron Microscopy Sciences, Hatfield, PA), inverted, and centrifuged at 300 × g for 10 min at 4^{o}C. Hydrogels in plates of identical set-up that were inverted at 4^{o}C but not centrifuged were used as controls for all conditions. Following centrifugation or inversion, cells were rinsed once with PBS and trypsinized. A Z2 Coulter counter (Beckman Coulter, Brea, CA) was used to determine the number of cells adhered to gels after either centrifugation or inversion. A cell retention ratio was calculated as the total number of cells remaining after centrifugation divided by the number of cells retained after inversion. Statistical significance between samples was determined by two-way ANOVA analysis.

4.3 Modification of the PVA Backbone

In this study, we investigated cell adhesion as a function of surface stiffness and chemistry. We synthesized PVA hydrogels with increasing percentages of methacrylation. This generated a series of hydrogels with differing mechanical properties. Methacrylated PVA was subsequently functionalized with an amine moiety for conjugation of antibodies. The nomenclature we used for each PVA formulation is as follows: 1 mol% methacrylation is designated as PVA-1, 2 mol% is PVA-2, 5 mol% is PVA-5, and 10 mol% is PVA-10. PVA hydrogels presenting three ratios of antibodies, either 1:0, 1:1, or 0:1 anti-VCAM1:anti-E-selectin, were used to study cell adhesion strength. EC binding to functionalized PVA hydrogels was quantified using a centrifugation assay and compared to unmodified, aminated PVA and RGD-modified PVA.

Methacrylated, Aminated PVA Synthesis

Figure 4.1 depicts the chemical reaction scheme for synthesizing methacrylated, aminated PVA. Representative ^{1}H NMR spectra for unmodified, methacrylated, and aminated PVA are shown in **Figures 4.2-4.6**. Peaks at chemical shifts of 5.6-6 ppm (vinyl) and 2.8 ppm (amine) confirmed successful methacrylation and amination, respectively. **Table 4.1** describes the efficiency of methacrylation and amination for the four PVA formulations. This was calculated from the ratio of vinyl or amine peaks to the –CH and $–CH_2$ groups in the NMR spectra as determined by the area under the curve (AUC).

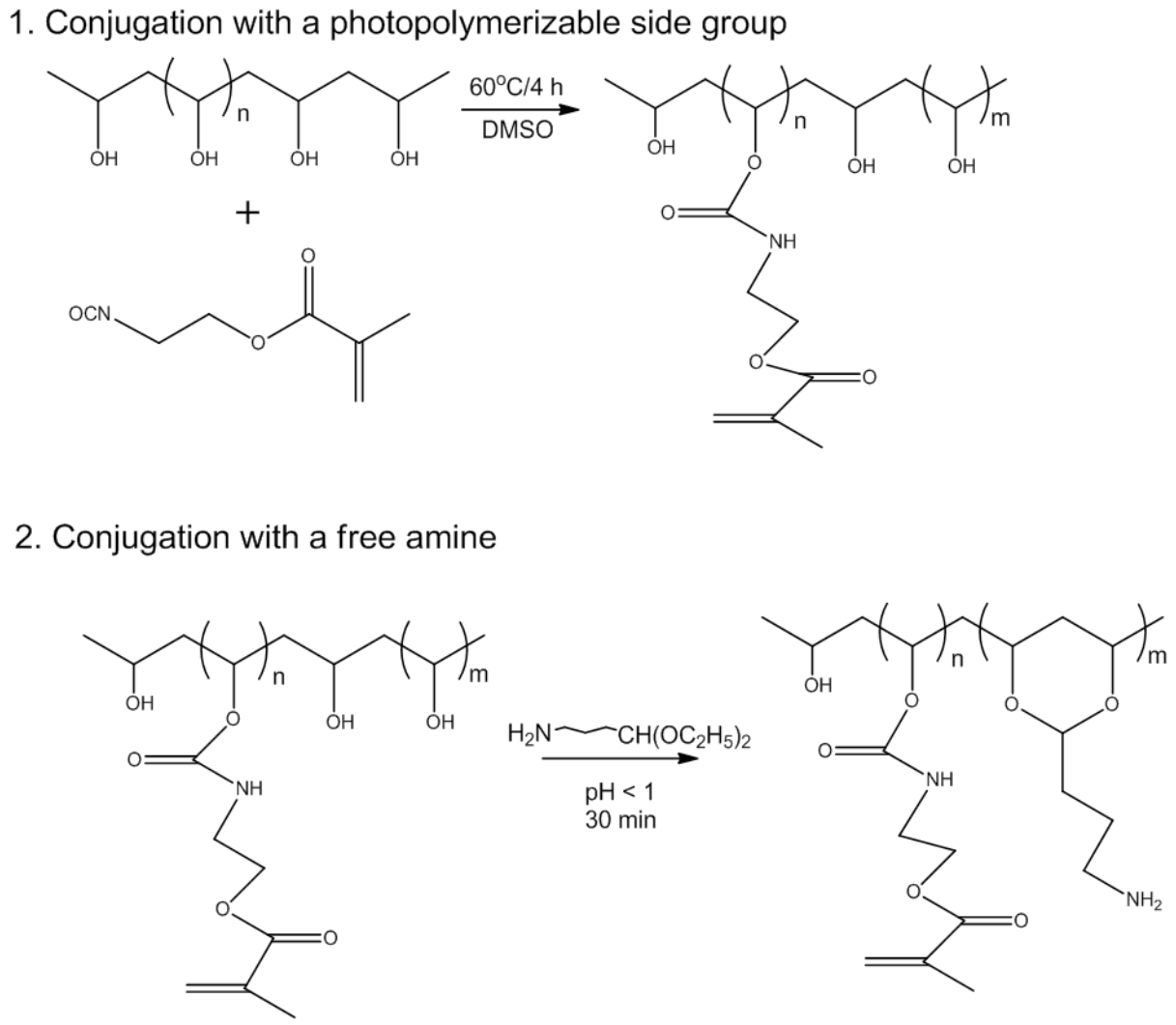

Figure 4.1: Reaction scheme for methacrylation (1) and amination (2) of polyvinyl alcohol.

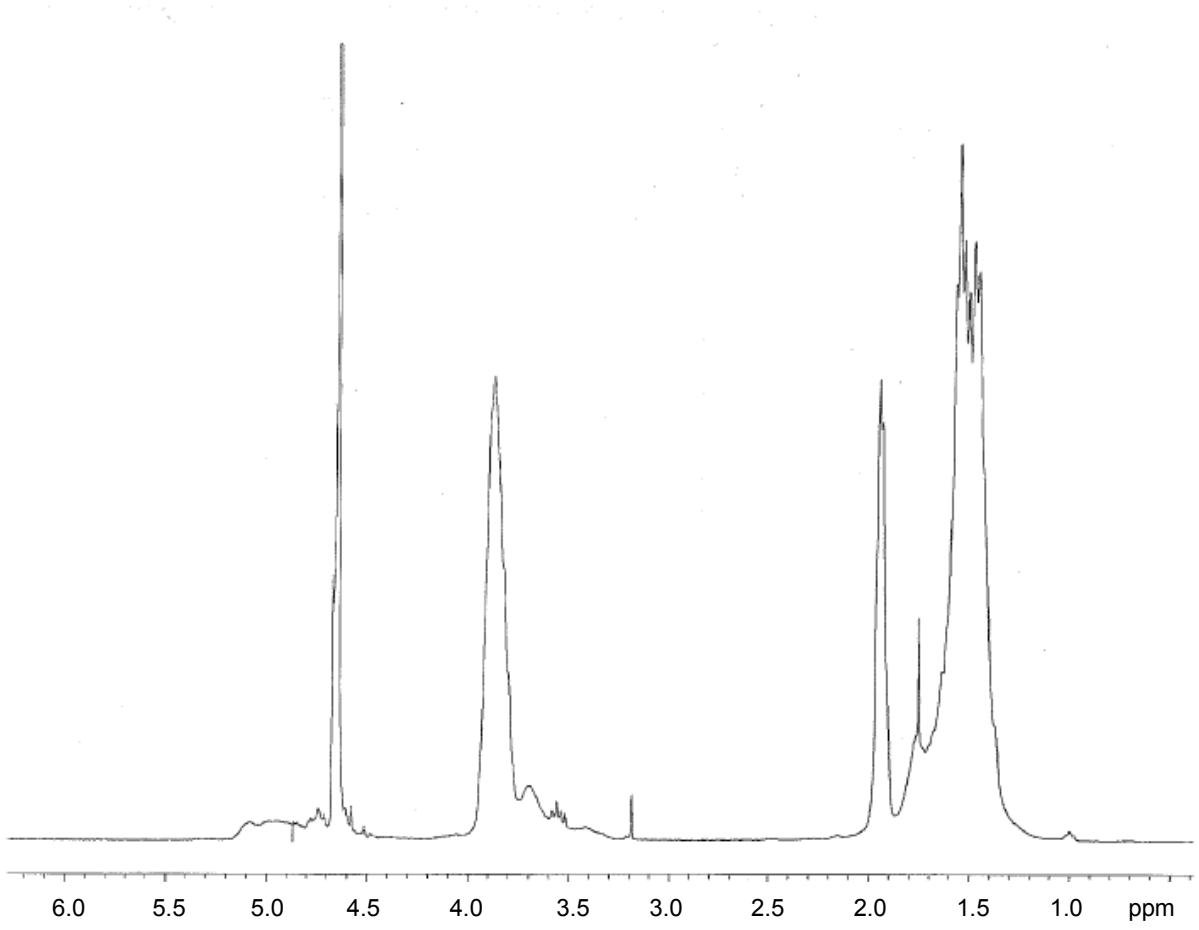

Figure 4.2: ^{1}H NMR spectrum of unmodified PVA.

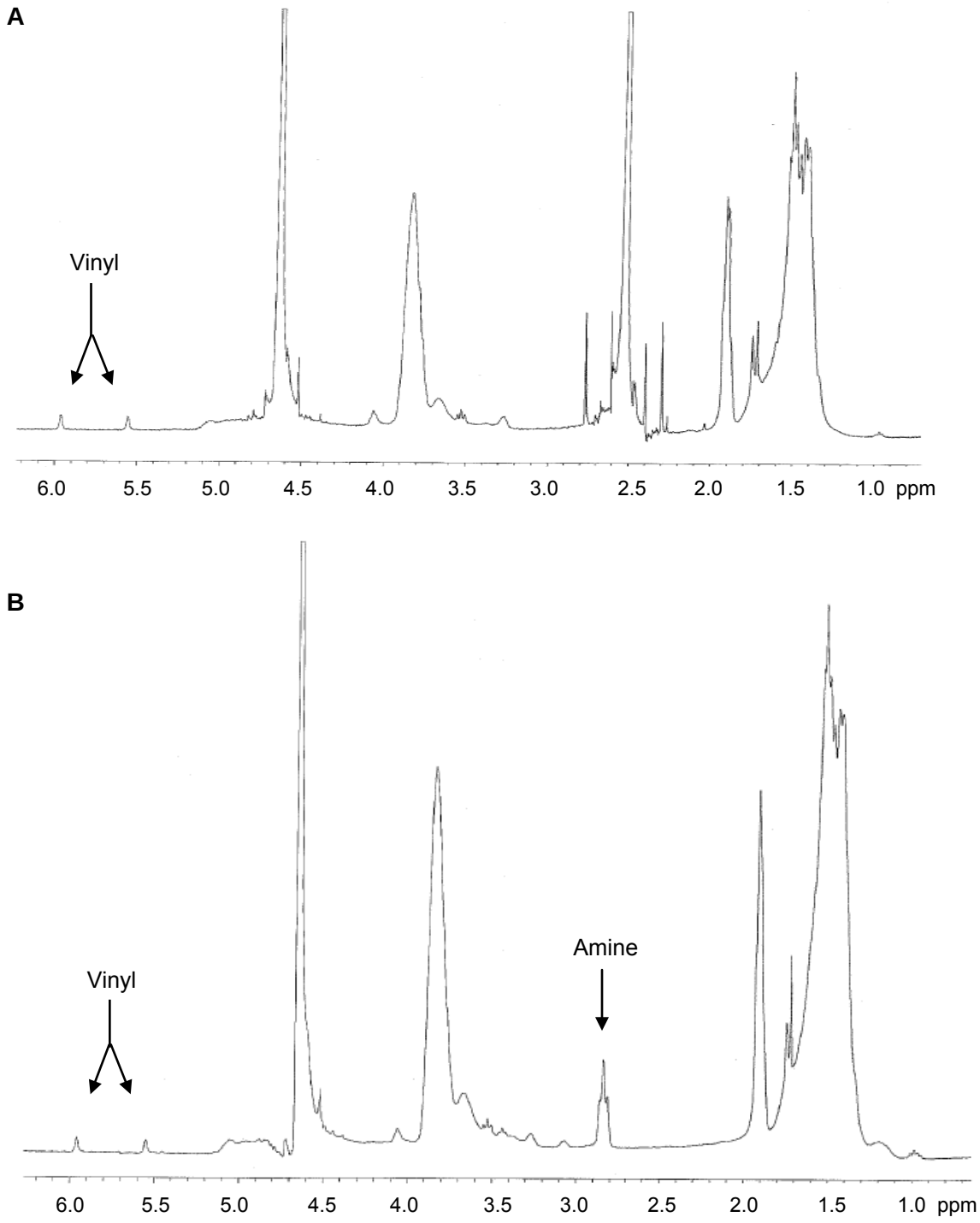

Figure 4.3: ^{1}H NMR spectrum of PVA-1. (A) Methacrylated and (B) methacrylated and aminated PVA-1.

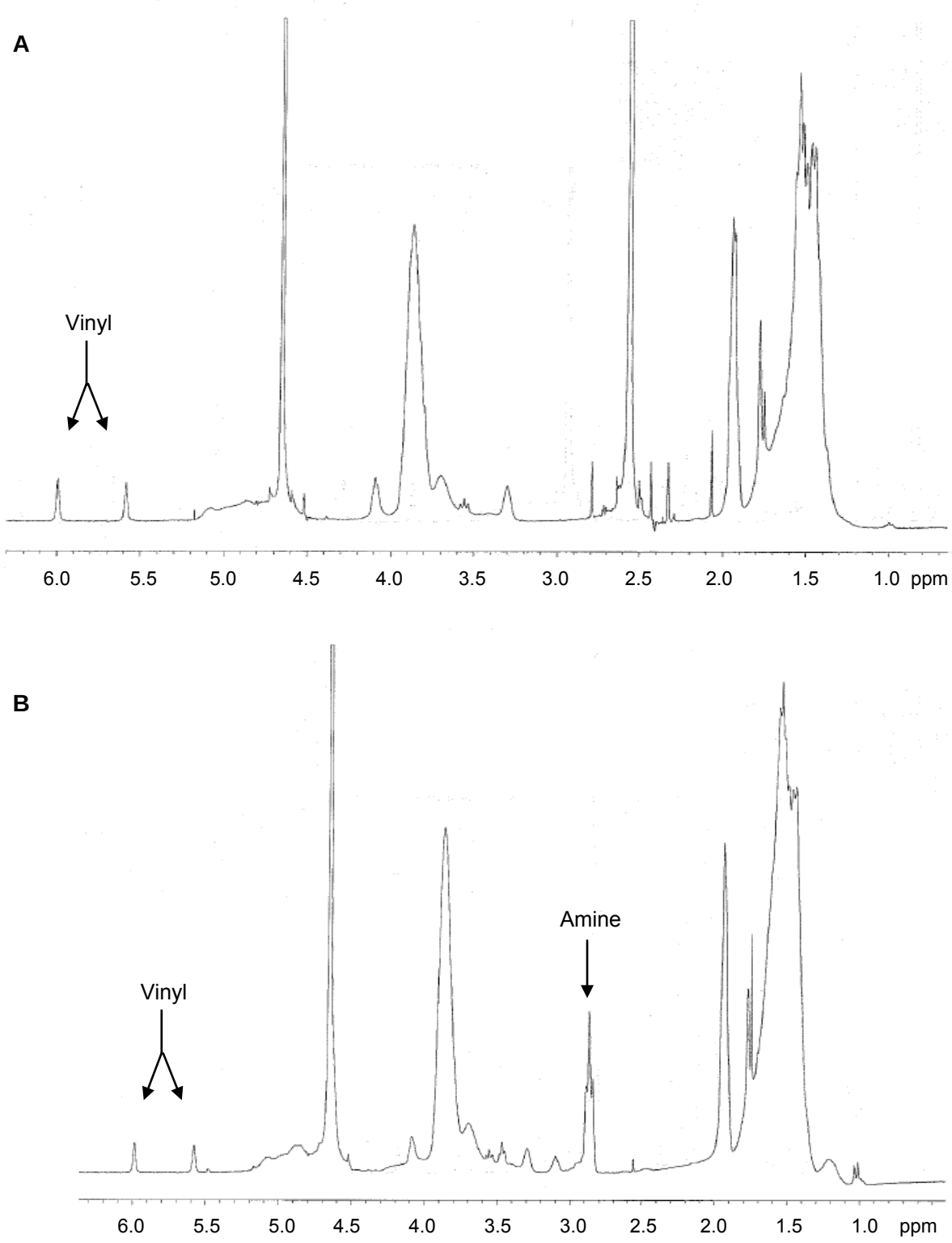

Figure 4.4: ^{1}H NMR spectrum of PVA-2. (A) Methacrylated and (B) methacrylated and aminated PVA-2.

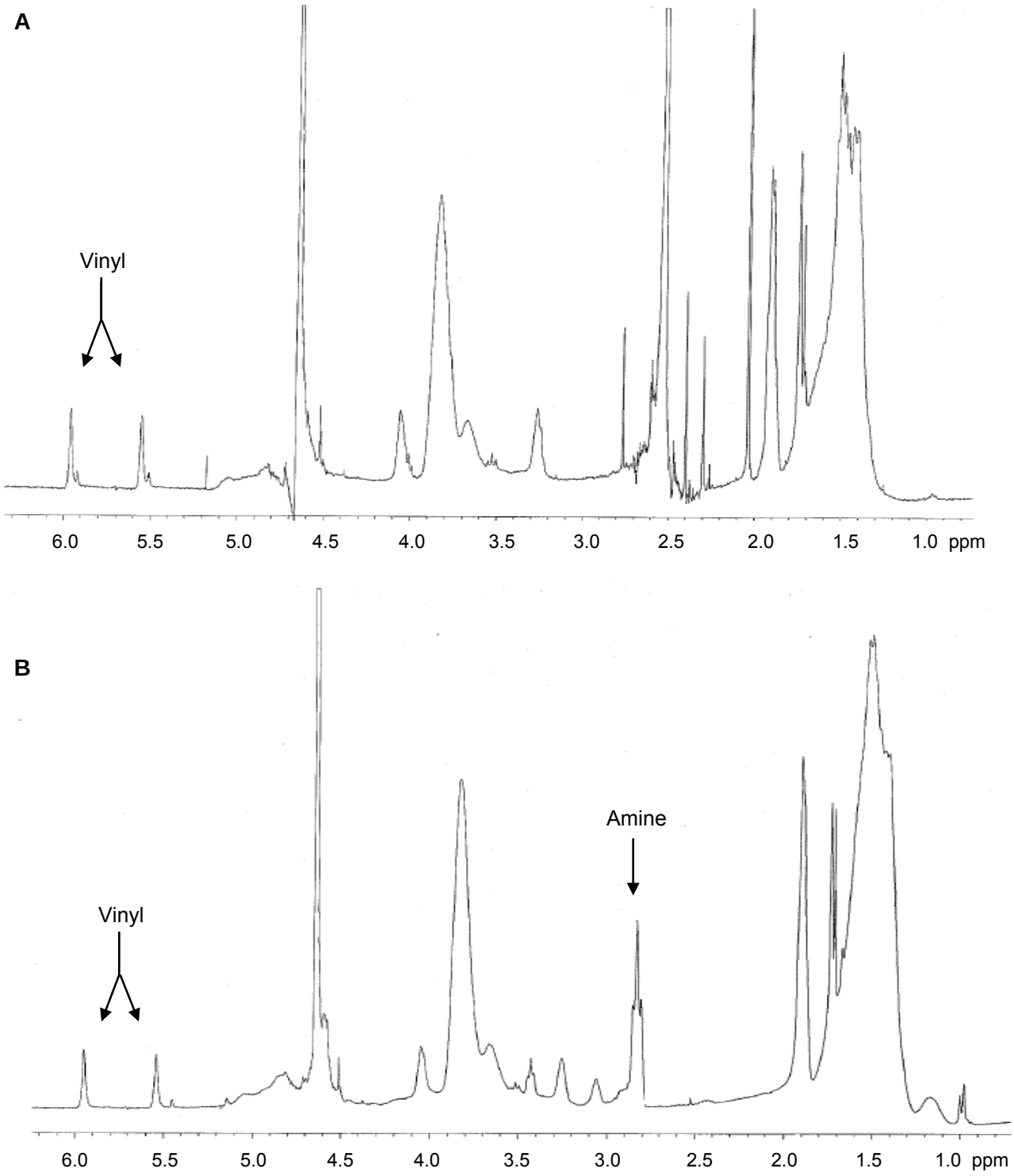

Figure 4.5: ^{1}H NMR spectrum of PVA-5. (A) Methacrylated and (B) methacrylated and aminated PVA-5.

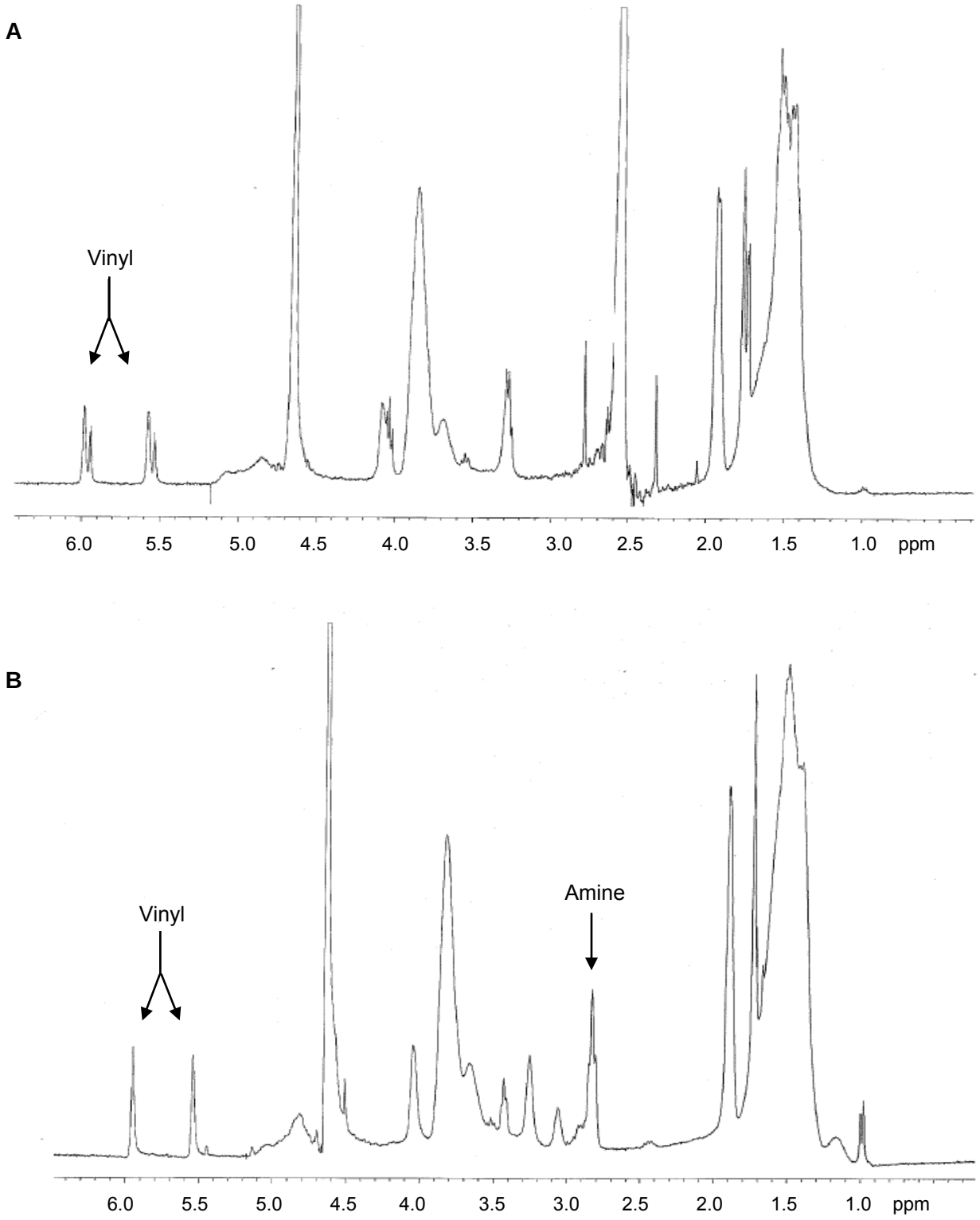

Figure 4.6: ^{1}H NMR spectrum of PVA-10. (A) Methacrylated and (B) methacrylated and aminated PVA-10.

Table 4.1: Functionalization of PVA backbone as determined by ^{1}H-NMR

	Target Methacrylation (mol%)	Measured Methacrylation (mol%)	Target Amination (mol%)	Measured Amination (mol%)
PVA-1	1	0.68	10	4.3
PVA-2	2	1.15	10	4.6
PVA-5	5	1.73	10	4.6
PVA-10	10	3.41	10	4.4

4.4 Mechanical Properties of PVA Hydrogels

Methacrylate group concentration was altered to vary the elastic and swelling properties of synthesized gels. Crosslinking occurred with the formation of poly (methacrylate) chains that connect two or more PVA chains. A schematic of this process is shown in **Fig. 4.7**. The distance between crosslinks is dependent on the degree of substitution of the PVA chain. Young's moduli varied between 130 and 720 kPa for gels synthesized from a 10% w/v PVA-1 polymer solution and 30% w/v PVA-10 polymer solution, respectively (**Fig. 4.8A**). Young's moduli increased with increasing percentage of methacrylation or weight percent of PVA in polymer solutions. Mass swelling ratios reflected the extent of crosslinking of the gels (**Fig. 4.8B**); swelling ratios increased as the amount of methacrylate groups or weight percent of PVA decreased.

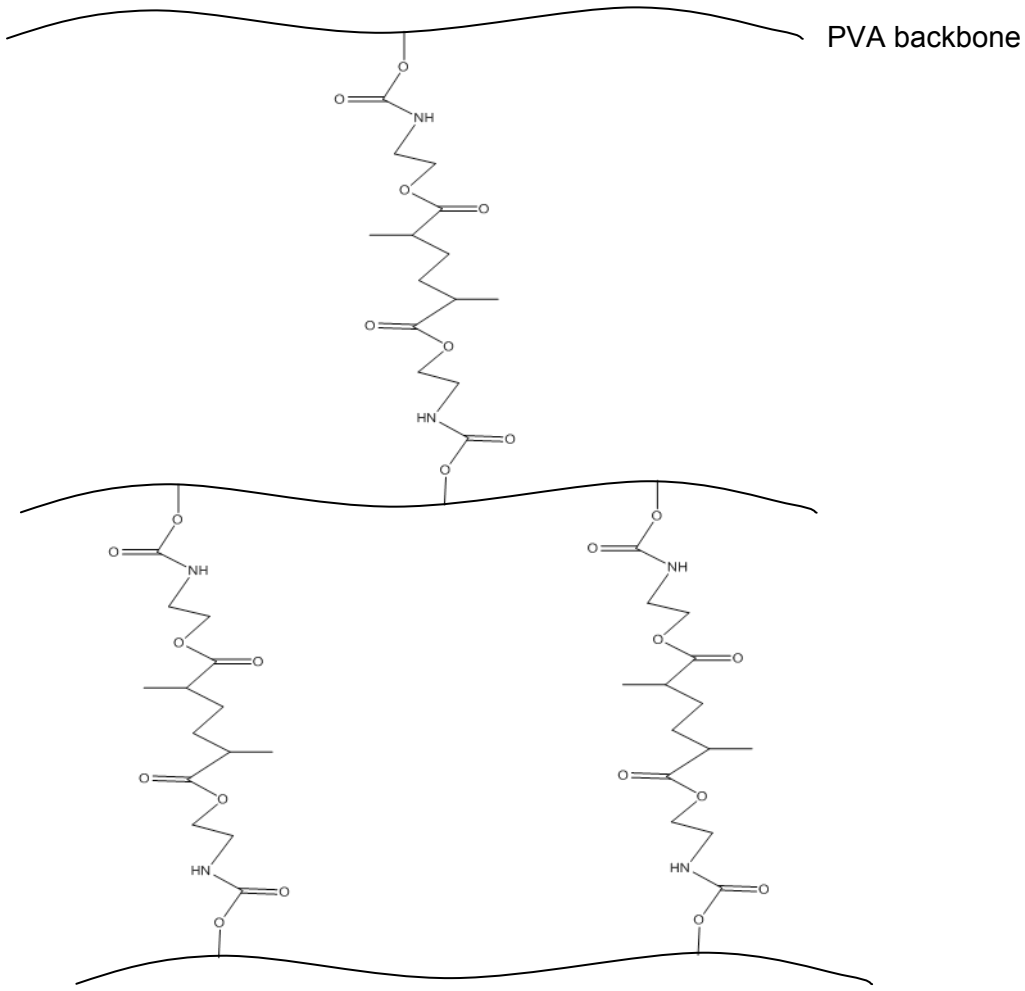

Figure 4.7: Schematic of PVA crosslinking.

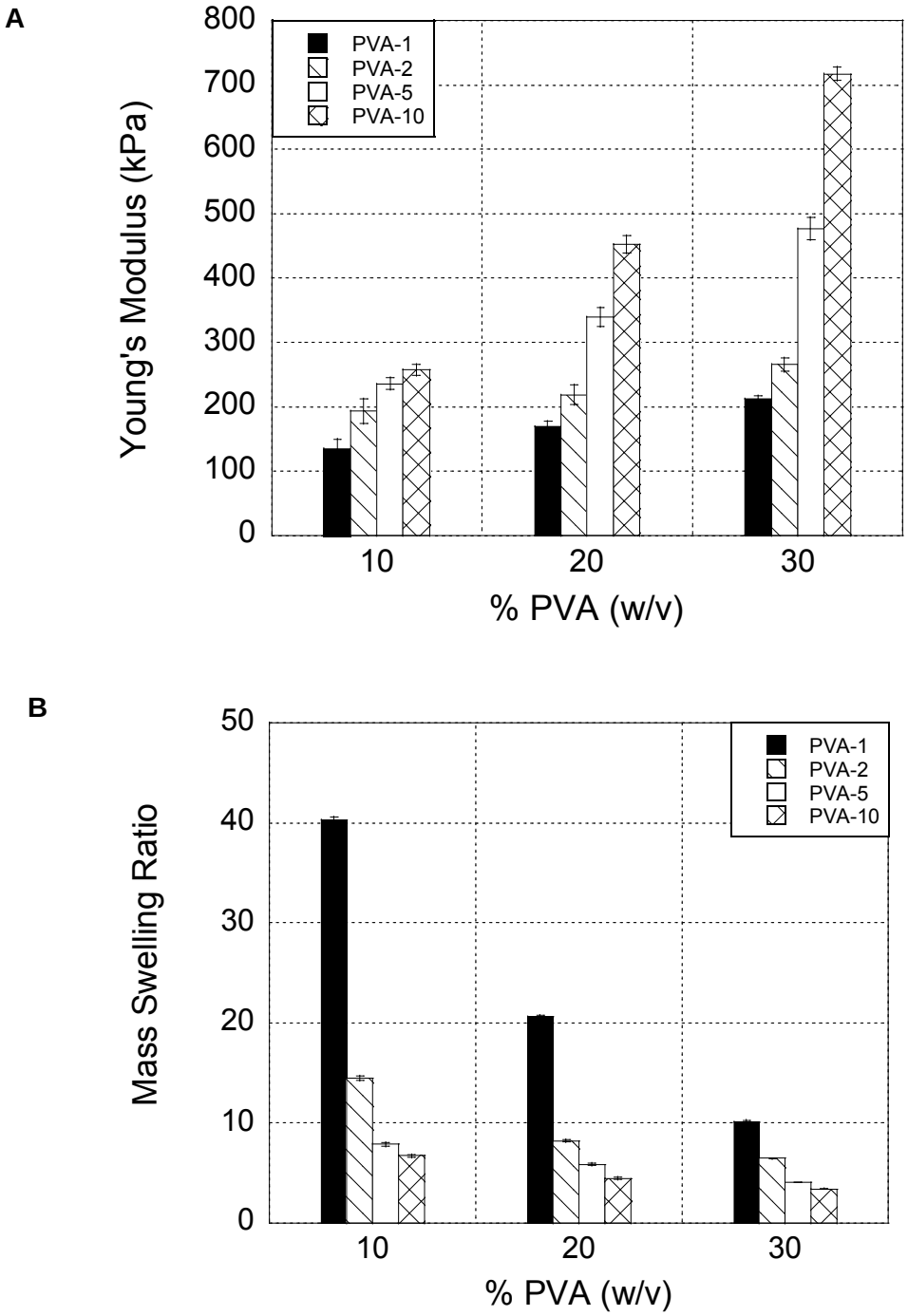

Figure 4.8: Characterization of PVA hydrogel mechanical properties. The Young's modulus (A) and mass swelling ratio (B) of PVA hydrogels is dependent on the degree of methacrylation and the weight percent of PVA. Error bars reported are standard error.

4.5 Functionalizing PVA Hydrogel Surfaces

ECs temporally upregulate VCAM1 and E-selectin in well-characterized patterns. We confirmed increased expression of VCAM1 and E-selectin in ECs exposed to 1, 5, or 10 ng/mL IL-1α for 2, 6, or 24 h (**Fig. 3.6**). The results were similar to those in documented reports of cytokine activated EC expression [80], including our previous publication that correlates gene expression with surface CAM presentation [85]. EC stimulation with 5 ng/mL IL-1α for 6 h resulted in the highest upregulation of both E-selectin and VCAM1. ECs were activated to maximize cell surface expression prior to being seeded on functionalized PVA hydrogels.

The relative cell adhesion abilities of PVA hydrogels with varying mechanical and chemical properties were investigated. Hydrogels (20% w/v) exhibiting sequentially increasing Young's moduli and decreasing mass swelling ratios were prepared from PVA-2, PVA-5, and PVA-10 solutions. Adhesion onto PVA-1 hydrogels was not evaluated due to the fragility of these hydrogels upon handling. Cell adhesion onto hydrogels modified with one of three ratios of anti-VCAM1:anti-E-selectin was tested and compared to that on unmodified, aminated PVA and RGD-modified PVA. Activated ECs were seeded onto hydrogels for 24 h. More ECs adhered to functionalized PVA hydrogels than to unmodified, aminated PVA hydrogels (**Fig. 4.9**). Gels modified with a 1:1 ratio of anti-VCAM1:anti-E-selectin had the highest cell density on their surface 24 h post-seeding (2×10^5 cells/cm^2). Surface cell densities (1×10^5 cells/cm^2) were comparable between gels presenting RGD, anti-E-selectin, or anti-VCAM1. Surface cell spreading was not observed on unmodified, aminated PVA hydrogels; cell spreading was qualitatively lower on hydrogels modified with anti-VCAM1 than on hydrogels modified with RGD, anti-E-selectin, or 1:1 anti-VCAM1:anti-E-selectin (**Fig. 4.10**).

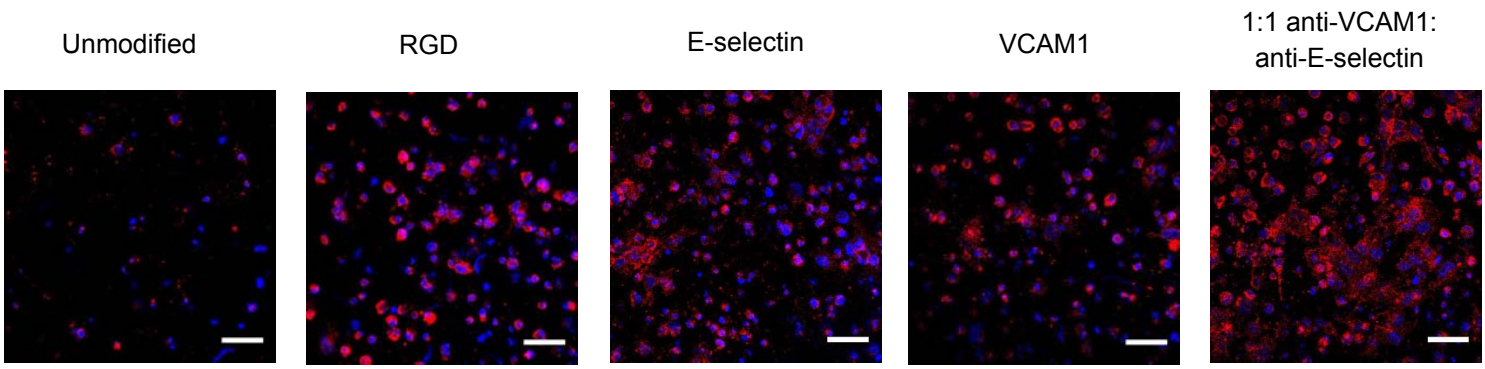

Figure 4.9: Confocal microscopy images of activated ECs on hydrogels. ECs are activated for 5 ng/mL IL-1α treatment for 6 h and seeded onto PVA-2 hydrogels (20% w/v PVA) for 24 h and stained with F-actin (red) and nuclear stains (blue). Scale bar is 50 μm.

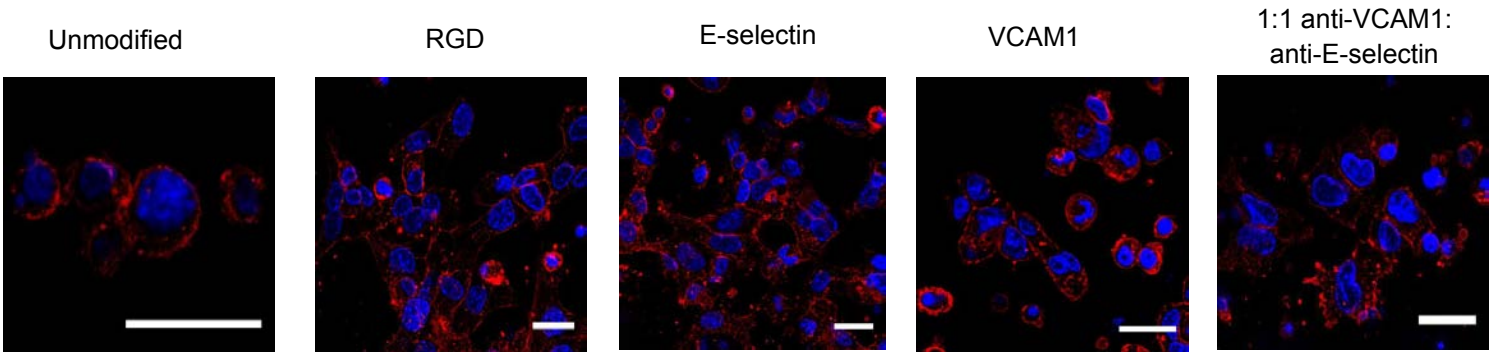

Figure 4.10: Morphology of ECs seeded onto hydrogels. ECs are stained with phalloidin (red) and DAPI (blue). Scale bar is 25 μm.

4.6 Cooperative Binding

Strength of cell adhesion onto hydrogel surfaces was examined via a centrifugation assay. We determined the cell retention ratio by dividing the number of cells adhered after gel centrifugation at 300 × g for 10 min by the number of cells adhered after gel inversion (1 × g) for 10 min. Cell adhesion onto PVA hydrogels modified with a 1:1 ratio of anti-VCAM1:anti-E-selectin was higher than on unmodified hydrogels and those modified with RGD, anti-E-selectin, or anti-VCAM1. No significant differences in adhesion onto PVA hydrogels with varying

mechanical properties (Young's moduli ranging from 170-450 kPa) were identified. However, differences in adhesion between the antibody-functionalized hydrogels were most pronounced on hydrogels with greater stiffness (PVA-10 vs. PVA-2) (**Fig. 4.11**).

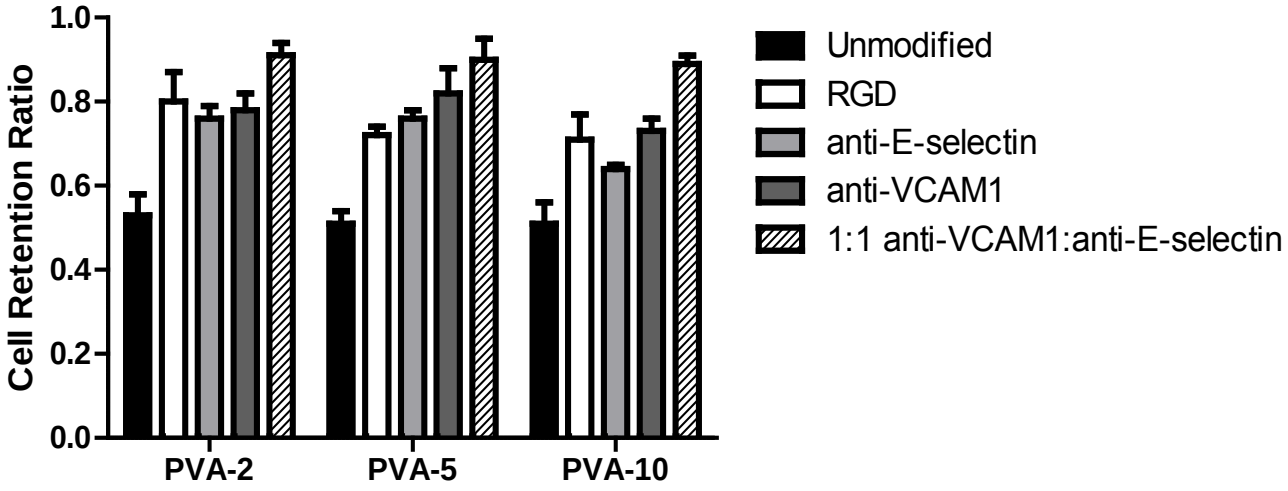

	Unmodified vs. RGD	Unmodified vs. anti-E-selectin	Unmodified vs. anti-VCAM1	Unmodified vs. 1:1 anti-VCAM1:anti-E-selectin	RGD vs. 1:1 anti-VCAM1:anti-E-selectin	E-selectin vs. 1:1 anti-VCAM1:anti-E-selectin	VCAM1 vs. 1:1 anti-VCAM1:anti-E-selectin
PVA-2	***	**	***	***	--	--	--
PVA-5	**	**	***	***	*	--	--
PVA-10	*	--	**	***	*	***	*

Figure 4.11: Synergistic binding of ECs on dual functionalized PVA hydrogels. Retention of ECs stimulated with IL-1α (5 ng/mL for 6 hr) seeded onto antibody-modified hydrogels. All PVA hydrogels tested were synthesized from 20% w/v PVA solutions. Cell retention ratio is defined as ratio of cells remaining on gels after centrifugation at 300 × g divided by cells retained on non-centrifuged samples. Error bars are reported as standard error. Statistical significance was calculated using a two-way ANOVA analysis with *$p < 0.05$, **$p < 0.01$, and ***$p < 0.001$.

4.7 Discussion

We synthesized a series of PVA hydrogels with different mechanical and chemical properties. We modified hydrogels with either antibodies against cell adhesion molecules upregulated on inflamed endothelium or RGD, a peptide that binds the $\alpha_5\beta_1$ integrin domain [165]. Our interest in cell adhesion molecules is derived from the fact that these molecules are regulated by cytokine-activation in a temporal and reproducible manner [80] and are localized within lipid rafts on the cell surface [166]. Mimicking cell-cell interactions by modifying hydrogels with antibodies against CAMs may allow for the engineering of the strength of cell adhesion onto polymeric materials.

Cell adhesion molecules participate in leukocyte-EC interactions while integrins mediate cell-matrix interactions. RGD signaling involves the FAK pathway [167] whereas VCAM1 and E-selectin signaling are mediated by the Rac pathway [168] and activation of the ERK1/2 pathway [169], respectively. Rac and ERK 1/2 are downstream of FAK; these pathways regulate various cellular processes, including adhesion, migration, and actin polymerization [170]. Thus, directing adhesion through cell adhesion molecules is similar to the use of RGD. However, our approach is unique because we can tune adhesion based on the molecular density and organization of anti-VCAM1 and anti-E-selectin presented on hydrogel surfaces.

The mechanical properties of our synthesized PVA hydrogels ranged from 130 to 720 kPa. This range reflected the Young's moduli exhibited by soft tissues, including thoracic aorta and femoral arteries (126-433 kPa [171]) and articular cartilage (500-1000 kPa [172]). Our hydrogels were stiffer than collagen (0.1-0.4 kPa [173]) and conventional alginate hydrogels (13-45 kPa, 0.21 g/mL calcium sulfate ($CaSO_4$) [174]) but were softer than hydroxyethyl methacrylate (HEMA) gels (1600 kPa, 3 mol% tetraethylene glycol dimethacrylate (TEGDMA)

[175]). Additionally, the mechanical properties of our gels fell within the range of previously described methacrylated PVA hydrogels, which spanned from 55-838 kPa [156, 157, 176]. Cell adhesion was not significantly altered within the range of Young's moduli examined in this study (**Fig. 4.8**). However, cell adhesion was affected by stiffness across a larger range: greater cell spreading and adhesion was found on polyacrylamide gels when moduli increased from 5 to 70 kPa [146], on poly(L-lysine)/hyaluronan films (3-400 kPa) with moduli greater than 300 kPa [147], and on polyelectrolyte films (0.15-150 MPa) of 150 MPa [148].

Notably, synergistic, cooperative binding onto PVA hydrogels presenting both anti-VCAM1 and anti-E-selectin was observed. Cooperativity may be defined as two antibodies that function together to produce a result not independently obtainable. We observed synergistic binding between IL-1α activated ECs and liposomes that present an optimal ratio of antibodies to relevant CAMs, a 1:1 ratio of anti-VCAM1:anti-E-selectin [85]. Liposome binding was inhibited by disrupting lipid raft formation and blocking of either CAM [87]. This previous work suggested that CAM surface density and organization may be important in cell-material interactions. In the present study, synergistic binding was observed on PVA hydrogels presenting 1:1 anti-VCAM1:anti-E-selectin. Cooperativity was demonstrated by the increased relative retention of cells on gels presenting 1:1 anti-VCAM1:anti-E-selectin versus PVA hydrogels presenting anti-VCAM1 or anti-E-selectin alone.

All hydrogels used for cell adhesion studies had similar antibody surface densities. Antibodies were conjugated onto aminated PVA hydrogels (as determined by ^{1}H NMR, **Table 4.1**) using carbodiimide chemistry. Our previous work has shown that this chemistry results in nonpreferential conjugation of antibodies to surfaces at 70% efficiency; the molecular density was confirmed by flow cytometry [86]. We estimate that our conjugation conferred a density of

700 molecules/μm^2 based on the number of surface amine groups available for antibody conjugation and the conjugation efficiency. This is comparable to the 20-200,000 molecules/μm^2 modification density reported in previous studies on RGD modified hydrogel surfaces [145, 177].

Strength of cell adhesion onto hydrogel surfaces was measured by a centrifugation assay where we compared the number of cells that remained adhered after centrifugation at 300 × g relative to inversion at 1 × g (**Fig. 4.11**). A force of 300 × g was equal to or greater than that used in previous analyses of cell adhesion strength [145, 162, 163]. The PVA hydrogels modified with 1:1 anti-VCAM1:anti-E-selectin strongly adhered ECs; a 0.9 cell retention ratio was observed. In comparison, the previously studied systems that most effectively adhered cells showed lower cell retention. For example, RGD modified interpenetrating networks composed of poly(acrylamide-co-ethylene glycol/acrylic acid) exhibited a cell retention ratio of 0.6 for rat calvarial osteoblast cells centrifuged at 57 × g [163] and dinitrophenol functionalized acrylamide surfaces demonstrated a 0.8 cell retention ratio for rat basophilic leukemia cells centrifuged at 300 × g [162]. The 1:1 anti-VCAM1:anti-E-selectin PVA hydrogels presented here thus enabled stronger binding than functionalized materials reported in the literature and demonstrated that hydrogel chemistry that mimics at least two types of cell-cell interactions can facilitate stronger cell adhesion than that which resembles cell-matrix interactions.

Presentation of either RGD, anti-VCAM1 or anti-E-selectin alone resulted in similar EC adhesion (**Fig. 4.11**). The dissociation constant of RGD-integrin binding was approximately 10^{-4}-10^{-6} M depending on the length of the peptide evaluated [178] whereas the disassociation constant of antibody-antigen binding was 10^{-9} M [179]. The differences in the disassociation constants did not correlate with overall EC adhesion; this is most likely because we measured

several interactions and not a single interaction. Since anti-VCAM1 and anti-E-selectin presenting PVA hydrogels had similar binding to RGD modified surfaces, we concluded that the stronger adhesion observed with 1:1 anti-VCAM1:anti-E-selectin was due to the synergy and cooperativity between anti-VCAM1 and anti-E-selectin.

PVA hydrogels are non-cytotoxic, can conform to any geometry, and can be photocrosslinked *in situ* on short time scales [156, 180]. These qualities make PVA suitable as a vascular embolic agent for the treatment of cerebral aneurysms. In comparison to ionically crosslinked alginate hydrogels that have been investigated for use in endovascular embolization [181, 182], functionalized PVA hydrogels can not only adhere to ECs but also be tuned to match vascular mechanical properties. Future work will evaluate functionalized PVA hydrogels in vascular remodeling applications.

Regarding the PVA and alginate hydrogel systems discussed in this and the following chapter, we have shown cooperative binding of our modified hydrogels to activated ECs *in vitro* using an acute inflammatory model rather than a more physiologically relevant model. We do not profess that this model can be used to treat aneurysms *in vivo* without more experimentation; rather, we submit that these proof of principle experiments will lay the groundwork for using synergy and cooperativity in engineering cell adhesion for vascular therapies. Although we have shown that a 1:1 ratio of anti-VCAM1:anti-E-selectin resulted in the greatest cell adhesion to hydrogels, further studies should re-evaluate this ratio to better complement EC conditions *in vivo*. Additional studies should evaluate cell adhesion based on a more realistic model that takes hemodynamics and shear stress into account rather than a centrifugation assay. The conformation of the antibodies adhered to the hydrogels was also not characterized, and antibodies most likely adhered randomly due to the availability of multiple binding sites. Future studies may benefit

from controlling antibody adhesion to the hydrogel surfaces. Finally, cell seeding beyond 24 h was not investigated. Complementary work should determine the effect of longer seeding times on cell adhesion. Nonetheless, we have shown the significance of cooperative antibody presentation in cell adhesion.

We have synthesized photopolymerizable, mechanically tunable, functionalized PVA hydrogels. PVA hydrogels presenting a 1:1 anti-VCAM1:anti-E-selectin ratio exhibited synergistic and cooperative adhesion to ECs. These functionalized hydrogels may serve as ideal candidates for tissue engineering applications. The results of this work have been published in Rafat et al. *Biomaterials* 2012 [183].

4.8 Experimental Challenges

We began by modifying PVA (13-23 kDa, 98% hydrolyzed) with the glycidyl methacrylate side group in our initial experiments. After modification, hydrogels took more than 90 s for gelation and were difficult to handle. We then decided to modify PVA (31 kDa) that was 88% hydrolyzed with 2-ICEMA, which produced hydrogels with tunable properties that could all be polymerized in 90 sec. A subsequent challenge was that PVA modification was conducted in a sequential two-step process, both of which took approximately one week due to drying and lyophilization requirements. Moreover, the synthesized PVA had approximately 20% efficiency. Because of these limitations, producing large quantities of modified PVA sufficient for hydrogel fabrication was time-consuming. One reason we chose to examine alginate hydrogels in the next section was the ability to fabricate hydrogels rapidly without chemical modification.

5 ALGINATE HYDROGELS

5.1 Introduction

Materials that adhere to the endothelial cell (EC) lining of blood vessels may be useful for treating vascular injury, including treatments for cerebral aneurysms. Cell adhesion molecules (CAMs), such as endothelial leukocyte adhesion molecule-1 (E-selectin) and vascular cell adhesion molecule-1 (VCAM1), modulate EC-leukocyte interactions. In this study, we mimicked cell-cell interactions by seeding cells on alginate hydrogels modified with antibodies against E-selectin and VCAM1, which become upregulated during inflammation. ECs were activated with interleukin-1α (IL-1α) to increase CAM expression and subsequently seeded onto hydrogels. The strength of cell adhesion onto gels was assessed via a centrifugation assay. Synergistic EC adhesion was observed on hydrogels presenting a 1:1 ratio of anti-VCAM1:anti-E-selectin. Cell adhesion was stronger on dual functionalized gels than on gels modified with anti-VCAM1, anti-E-selectin, or the arginine-glycine-aspartic acid (RGD) peptide alone. Anti-VCAM1:anti-E-selectin-modified hydrogels may be engineered to adhere the endothelium cooperatively.

A fundamental challenge in tissue engineering is modulating cell adhesion as it affects cell migration and assembly [74]. Integrin-extracellular matrix (ECM) interactions are employed to regulate cell adhesion [184, 185]. For example, RGD peptides are widely used to increase cell attachment to materials that are characterized as non-adhesive, such as hyaluronic acid (HA) [186], polyvinyl alcohol (PVA) [156], and alginate [76].

Engineering substrate surface chemistry has enabled control over cell behavior. The type and number of binding sites have affected cell migration and differentiation [77]. Increasing the molecular surface density beyond the saturation density, however, does not increase adhesion

strength [145]. Beyond the saturation density, it has been observed that cell adhesion can be controlled via multiple cooperative receptor-ligand interactions [82]. We have shown previously that optimal ratios of CAMs cooperatively bind drug delivery vehicles [85-87]. Enhanced cell adhesion was shown to be dependent on the relative molecular surface density; vehicles presenting an optimal anti-VCAM1:anti-E-selectin ratio that complemented EC surface expression showed increased binding [85].

To overcome the saturation of integrin-ECM interactions, we proposed to use dual functionalized hydrogels to strengthen cell adhesion. As a model system, we have engineered cellular adhesion by modifying materials with antibodies against CAMs that are upregulated on the surface of inflamed ECs. CAM expression is regulated by cytokine stimulation, shear stress, substrate mechanical properties, and cell-cell interactions [187-189]. CAMs, including E-selectin and VCAM1, are known to be expressed on ECs in inflammatory diseases such as atherosclerosis [190, 191] and cerebral aneurysms [69].

In this study, we hypothesized that alginate hydrogels presenting antibodies against VCAM1 and E-selectin may result in strong, cooperative adhesion. We measured cell retention as a function of time and increasing force via a centrifugation assay. We chose to evaluate natural alginate hydrogels in addition to the synthetic PVA hydrogels in the previous chapter due to their non-adhesiveness, *in situ* gelation, and ease of modification. Alginate hydrogels presented a different stiffness range as compared to PVA and were also previously implicated in the treatment of aneurysms [181, 182]. Engineering cell adhesion strength through the presentation of antibodies may be useful in improving materials design for vascular embolization, where binding of materials to the endothelium may be compromised by hemodynamic forces.

5.2 Methods and Materials

Materials

Calcium sulfate ($CaSO_4$), alginic acid sodium salt from brown algae (alginate, medium viscosity), *N*-(3-Dimethylaminopropyl)-*N′*-ethylcarbodiimide hydrochloride (EDC), N-hydroxysuccinimide (NHS), 2-(N-morpholino)ethanesulfonic acid hydrate (MES), and sodium chloride (NaCl) were purchased from Sigma Aldrich (St. Louis, MO). Hank's Balanced Salt Solution (HBSS) and phosphate buffered saline (PBS) were purchased from Invitrogen (Carlsbad, CA).

Alginate Hydrogel Fabrication

Alginate was dissolved in phosphate buffered saline (PBS) to make a 2% w/v solution and filtered through 0.45 μm pore syringe filters. $CaSO_4$ slurries in deionized water were prepared at concentrations of 0.15, 0.80, and 1.5 M. Hydrogels were fabricated by mixing 2% w/v alginate and a $CaSO_4$ slurry at a 20:1 v/v ratio in connected syringes. Hydrogels were made either in Teflon molds (10 mm × 1 mm × 30 mm) or between two glass slides (75 mm × 50 mm × 1 mm) and punched out using a cork borer with a 12 mm inner diameter. All crosslinking took place at room temperature to enable calcium diffusion [192].

Mechanical Properties

Hydrogels (10 mm × 1 mm × 30 mm) were extended at a rate of 1 mm/min at room temperature immediately after fabrication using an Instron BioPuls machine (Instron, Norwood, MA). Swelling properties were evaluated as well. Hydrogels were swollen in HBSS to equilibrium. Mass swelling ratios (Q) were calculated by $Q = W_S / W_D$, where W_S and W_D are the masses of the swollen and dry hydrogels, respectively.

Cell Culture

Human umbilical vein ECs (Lonza, Walkersville, MD) were cultured in Endothelial Cell Growth Medium-2 (EGM-2; Lonza). ECs were maintained at 37^{o}C with 5% CO_2 in a humidified incubator and grown to confluence before seeding onto hydrogels. All hydrogel formulations used with cells were crosslinked with 1.5 M $CaSO_4$.

Covalent Surface Modification of Hydrogels

The chemical reaction scheme for covalent surface modification of alginate hydrogels is shown in **Figure 5.1**. Gels were activated for conjugation by soaking for 1 h at room temperature in a solution of EDC (1 mg/g alginate) and NHS (0.5 mg/g alginate) dissolved in 0.1 M MES buffer (pH=6.5, 0.3 M NaCl). Primary monoclonal mouse anti-human antibodies (R&D Systems, Minneapolis, MN) or arginine-glycine-aspartic acid-serine (RGD, Tocris Bioscience, Ellisville, MO) were added to the above solution at a total of 0.5 mg antibody/g alginate and allowed to react at 4^{o}C overnight. Gels were rinsed with PBS before use to remove excess reactants. Detection of surface-conjugated antibodies was achieved by utilizing FITC-labeled goat anti-mouse secondary antibodies (Abcam, Cambridge, MA) at 0.5 and 0.75 mg antibody/g alginate in conjugation reactions. Gels with conjugated primary antibodies were incubated with fluorescently labeled secondary antibodies (0.5 mg antibody/g alginate) for 1 h at room temperature. Fluorescence of modified gels relative to unmodified ones was measured using a Spectramax Gemini XPS microplate reader (Molecular Devices, Sunnyvale, CA) at 490 nm/525 nm excitation/emission. Although hydrogels were modified at the same relative density, a limitation of this study was that we did not directly quantify the number of molecules on the hydrogels.

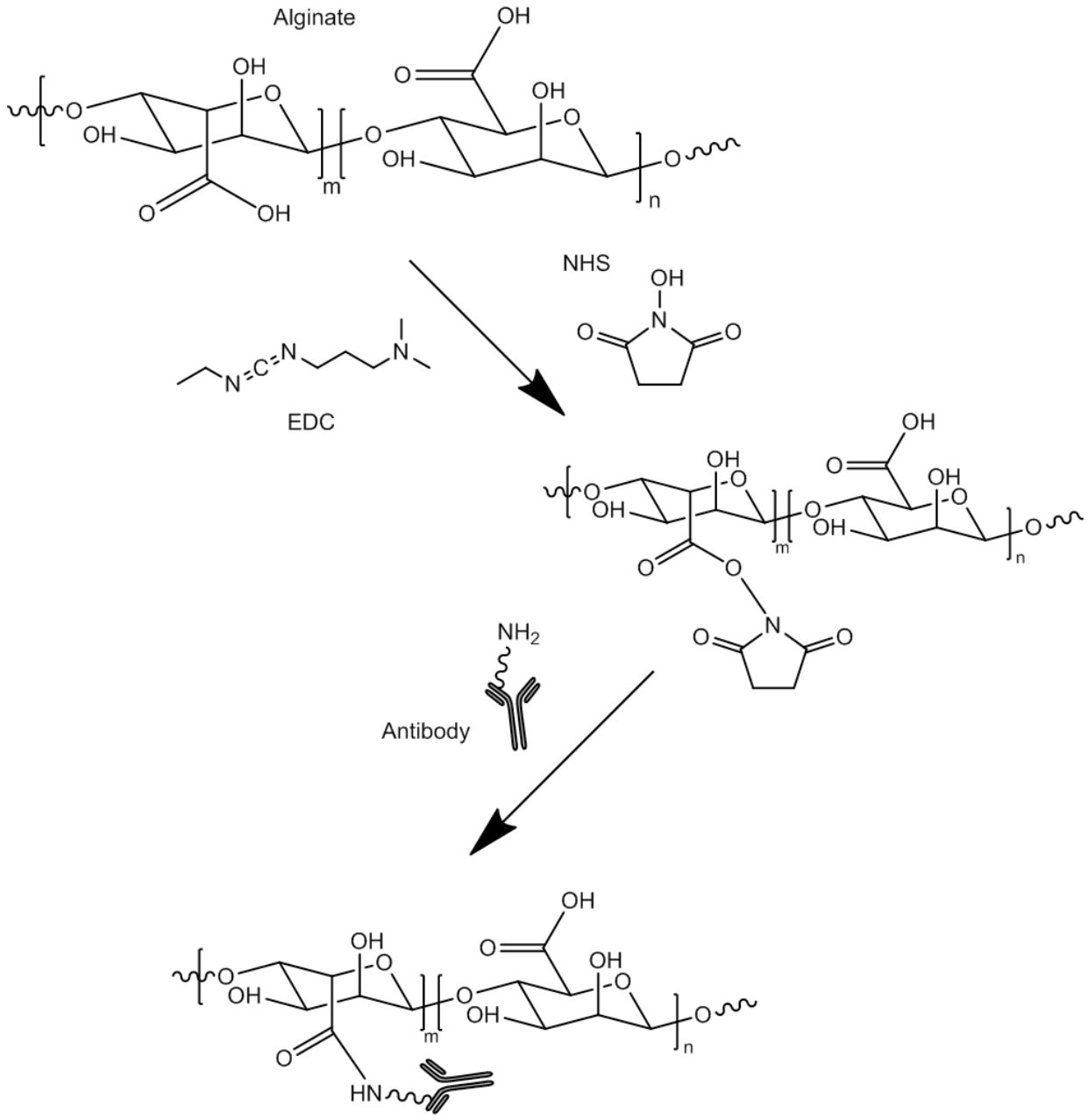

Figure 5.1: Chemical reaction scheme of antibody modification of alginate hydrogels.

X-ray Photoelectron Spectroscopy

X-ray Photoelectron Spectroscopy (XPS) was used to characterize the chemical composition of the gel surface. Unmodified or anti-E-selectin-modified hydrogels were dried at 65^{o}C and placed on aluminum foil. Gels were analyzed on an XPS ESCA SSX-100 using a monochromatic Al Kα X-ray source.

Atomic Force Microscopy

Atomic force microscopy (AFM) imaging was used to characterize the gel surface. Unmodified, EDC/NHS reacted, or anti-E-selectin-modified hydrogels were dried at 65^{o}C. Prior to imaging, gels were attached to glass slides with cyanoacrylate glue. Gels were imaged on an Asylum MFP3D Atomic Force Microscope at a frequency of 1 Hz with a MikroMasch Ultrasharp NSC14/AIBS Cantilever (10 nm radius, 160 kHz resonance frequency).

Centrifugation Assay

A centrifugation assay was used to determine the adhesion of cells onto hydrogels. This widely used technique evaluated the force necessary to disrupt interactions between the cells and hydrogels. The parameters that we used were comparable to previous studies of cell-matrix interactions [145, 162, 163]. Gels were seeded with 0.5×10^{6} non-activated or activated ECs per gel for 4 or 24 h. Activated ECs were treated with 5 ng/mL IL-1α for 6 h. Serum free media was used during cell seeding to remove the effects of the adsorption of serum proteins on cell adhesion. Gels undergoing centrifugation were placed in 24 well plates filled completely with media in order to avoid the possible harmful effects of air bubble formation on cell retention. Plates were sealed with Titer-Top Plate Sealant (Electron Microscopy Sciences, Hatfield, PA), inverted, and centrifuged at 300, 500, or 700 × g for 10 min at 4^{o}C. Hydrogels in plates that were

inverted at 4°C but not centrifuged were used as controls. Centrifugal forces were converted to a dislodging force, F_D in dynes, using the following equation [162, 164]: $F_D = (\rho_{cell}-\rho_{medium}) \times V_{cell} \times RCF$, where ρ_{cell} is the density of the cell (1.07 g/cm^3), ρ_{medium} is the density of the medium (1.0 g/cm^3), V_{cell} is the volume of the cell (diameter = 10 μm), and RCF is the relative centrifugal force (× g, where g = 980 dyne/g). Cells were estimated to feel between 1.1×10^{-5} and 2.5×10^{-5} dynes when centrifuged at 300 to 700 × g.

Following centrifugation or inversion, cells were rinsed once with PBS and trypsinized. A Z2 Coulter counter (Beckman Coulter, Brea, CA) was used to determine the number of cells adhered to gels after either centrifugation or inversion. The cell retention ratio, defined as the total number of cells remaining after centrifugation divided by the number of cells retained after inversion, was quantified for all gels. Statistically significant differences in cell retention on gel samples were determined using two-way ANOVA analysis.

5.3 Mechanical Properties of Alginate Hydrogels

We investigated the strength of cell adhesion onto alginate hydrogels as a function of gel surface chemistry. Adhesion onto alginate hydrogels presenting three different ratios of antibodies (1:0, 1:1, or 0:1 anti-VCAM1:anti-E-selectin) was examined. A schematic of cell adhesion onto antibody-modified hydogels is shown in **Figure 5.2**. EC binding to functionalized alginate hydrogels was quantified using a centrifugation assay and compared to binding on unmodified and RGD-modified hydrogels.

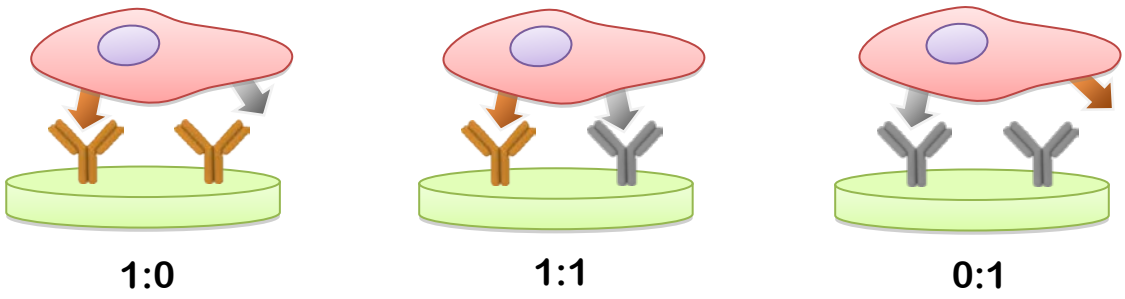

Figure 5.2: Schematic of cell adhesion to modified hydrogels. Arrows represent VCAM1 (orange) and E-selectin (gray) receptors on cell surfaces. Hydrogels presenting optimized ratios of antibodies allow for strong adhesion between the expressed antigen and antibody.

The $CaSO_4$ concentration used for crosslinking was altered during synthesis to vary the elastic and swelling properties of the hydrogels. The linear-elastic region between 0-0.2 tensile strain of the stress-strain curve was used to determine the Young's modulus (**Fig. 5.3A**). For gels synthesized with a 0.15 M and 1.5 M $CaSO_4$ slurry, Young's moduli varied between 34 ± 3 and 70 ± 4 kPa, respectively (**Fig. 5.3B**). Young's moduli increased with increasing concentrations of $CaSO_4$. Swelling ratios increased as the amount of $CaSO_4$ used in synthesis decreased (**Fig. 5.3C**). All hydrogels used for cell studies were crosslinked with 1.5 M $CaSO_4$.

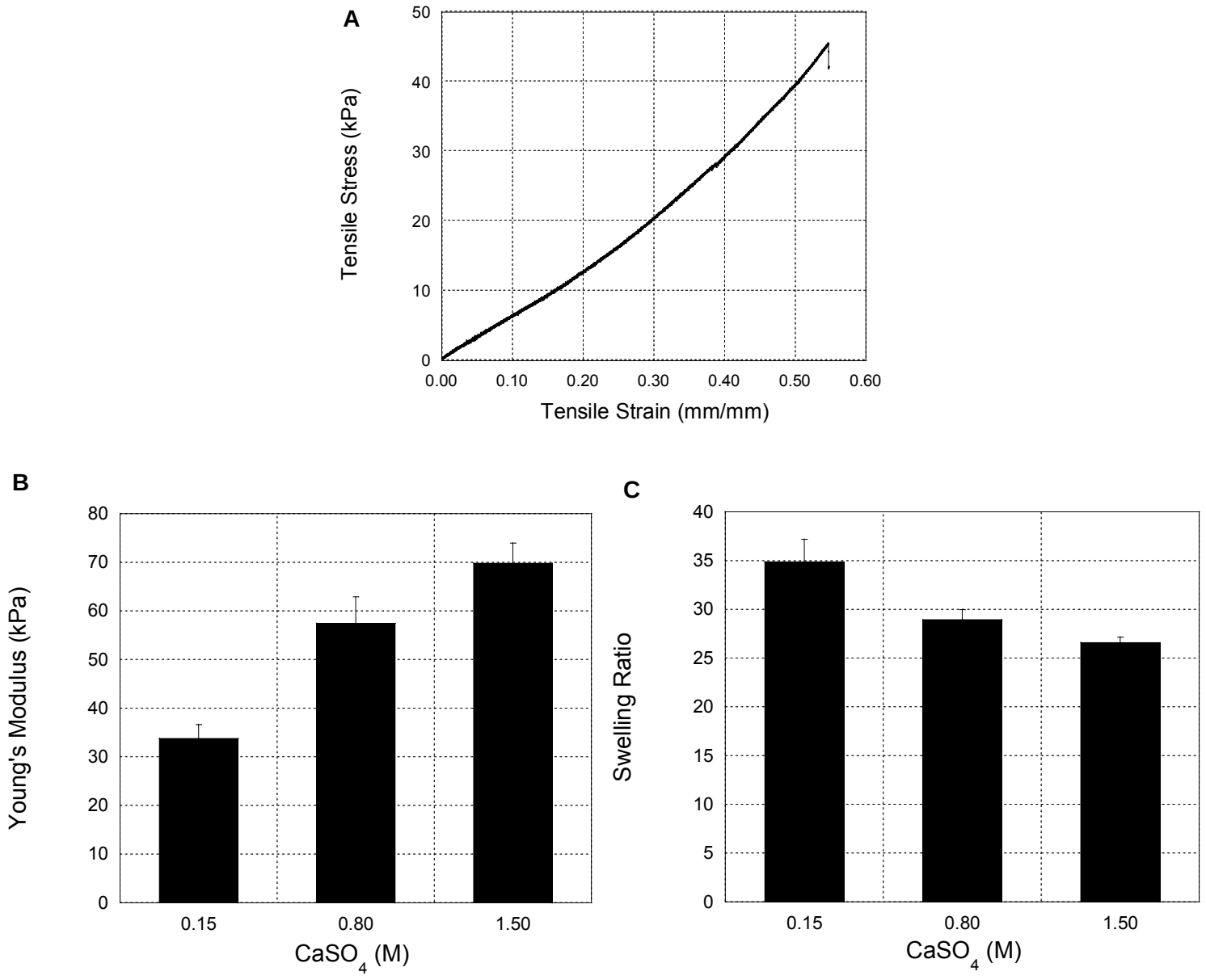

Figure 5.3: Characterization of alginate hydrogel mechanical properties. (A) Representative stress-strain curve for hydrogels made with 1.5 M $CaSO_4$. The Young's modulus (B) and mass swelling ratio (C) of alginate hydrogels is dependent on the concentration of $CaSO_4$. Error bars shown are standard error with n = 4.

5.4 Characterization of Modified Alginate Surfaces

XPS analysis of the molecular composition of the surfaces of unmodified (**Fig. 5.4A**), anti-E-selectin gels (**Fig. 5.4B**), and RGD-modified gels (**Fig. 5.4C**) verified successful conjugation of antibodies. A high-resolution focus on the nitrogen 1s orbital between 395-397 eV indicated the presence of nitrogen only in the modified gels [193] when compared to the unmodified condition (**Fig. 5.4D**). As unmodified alginate does not contain nitrogen, the increase in signal was attributed to the conjugation of anti-E-selectin or RGD.

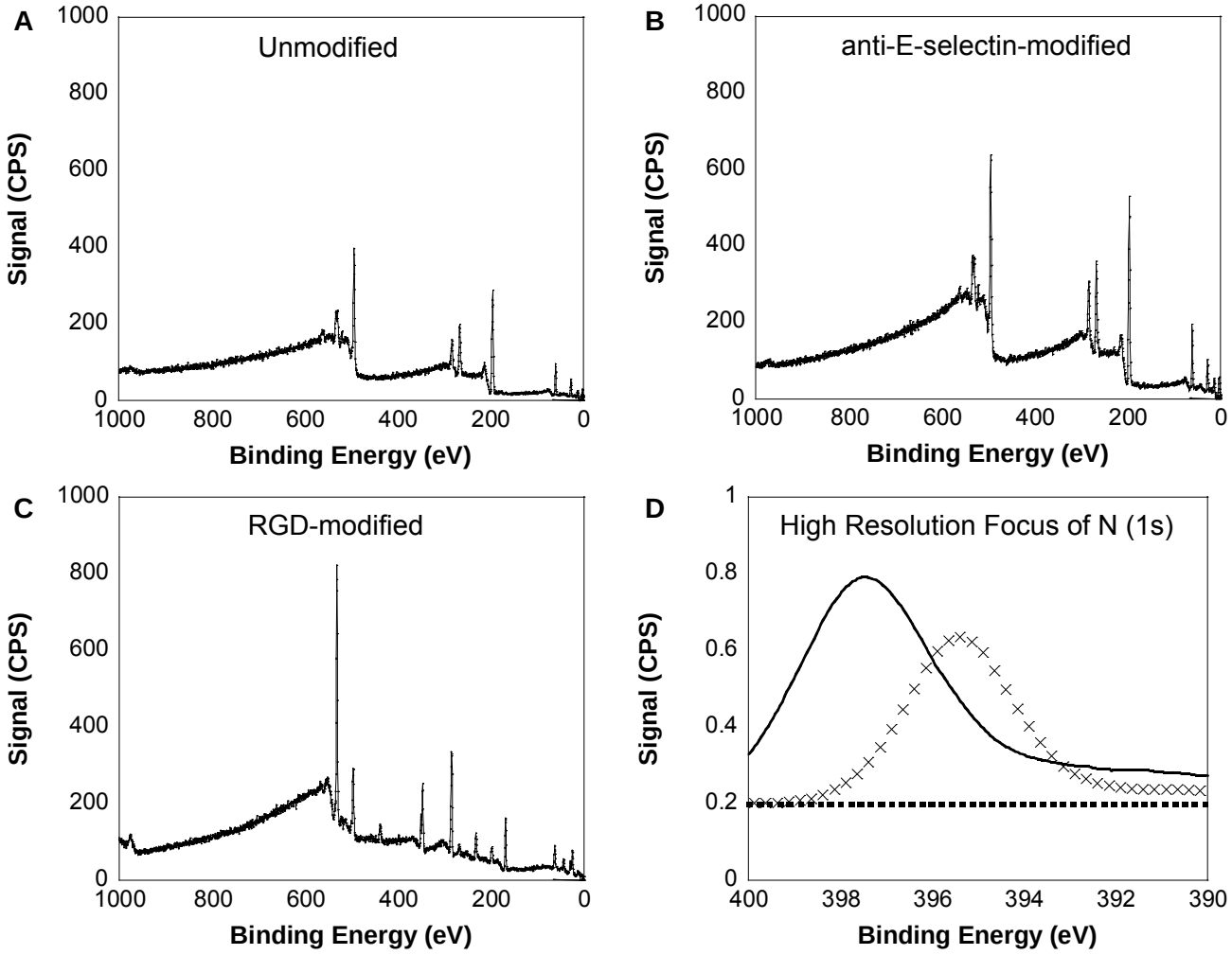

Figure 5.4: X-ray photoelectron spectroscopy analysis of alginate hydrogels. (A) Unmodified, (B) anti-E-selectin-modified, and (C) RGD-modified alginate hydrogels are shown.

Figure 5.4 (Continued): A high resolution focus on the nitrogen 1s orbital of the unmodified (dashes), RGD-modified (crosses), and anti-E-selectin-modified (solid) hydrogels is shown in (D).

Antibody conjugation to hydrogels was corroborated via AFM (**Fig. 5.5**). **Fig. 5.5Ai** presents a reconstructed topographical map of the unmodified gel surface. In contrast to the unmodified hydrogel, dense peaks of 5-10 nm in height were observed along the surface of the anti-E-selectin-conjugated gel (**Fig. 5.5Bi**). The surface of unmodified and EDC/NHS reacted gels (**Fig. 5.5Ci**) were relatively smooth except for surface features arising from dehydration of the gel. The presence of nanoscale features on anti-E-selectin-modified hydrogels was confirmed by cross-sectional analyses of gel surface height variation (**Fig. 5.5Bii**). Repeated, regular peaks and valleys measuring 4-6 nm were present along the cross-sectional width of the anti-E-selectin-modified gels while the unmodified and EDC/NHS reacted gels had smoother surfaces with broader height variations (**Fig. 5.5Aii, Fig. 5.5Cii**). Surface feature heights seen in cross-sectional analyses were consistent with prior published work regarding antibody height [194].

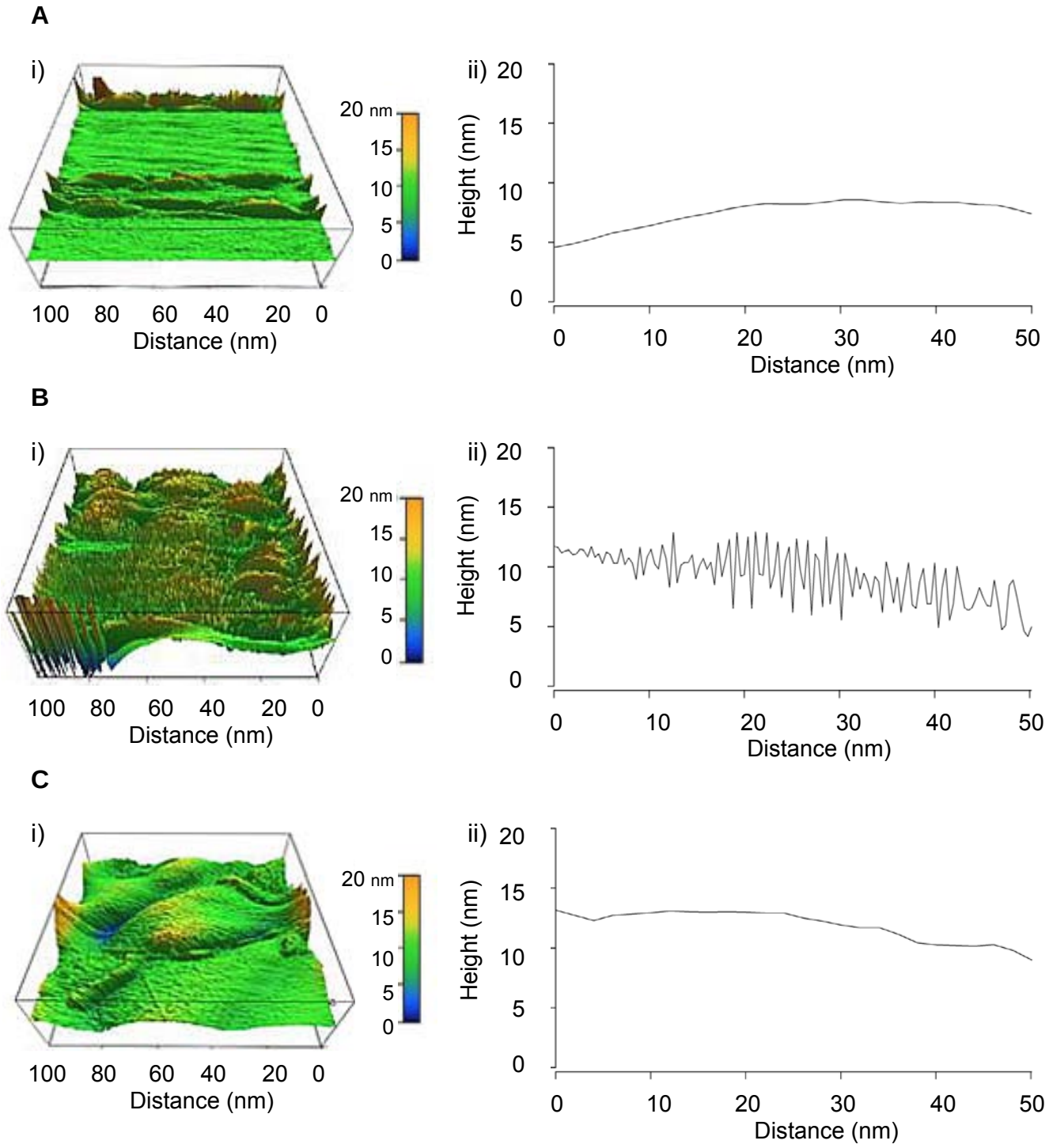

Figure 5.5: Atomic force microscopy analysis of surface modification. Determination of the surface properties of (A) unmodified, (B) anti-E-selectin-modified, and (C) EDC/NHS reacted alginate hydrogels using atomic force microscopy. (Ai), (Bi), and (Ci) are 3D topographical

Figure 5.5 (Continued): images (100 nm x 20 nm). (Aii), (Bii), and (Cii) are cross-sectional analyses of gel surface height variations for 100 nm wide sections.

We additionally confirmed antibody conjugation using fluorometric methods. Secondary antibodies (e.g. FITC-labeled goat anti-mouse secondary antibodies) were reacted with the hydrogel surfaces or conjugated to mouse anti-human primary antibodies. Increasing fluorescence was observed with increasing quantities of secondary antibody utilized in the conjugation reaction (**Fig. 5.6A**). Similar fluorescence intensities were measured for anti-E-selectin and anti-VCAM1 modified alginate hydrogels (**Fig. 5.6B**).

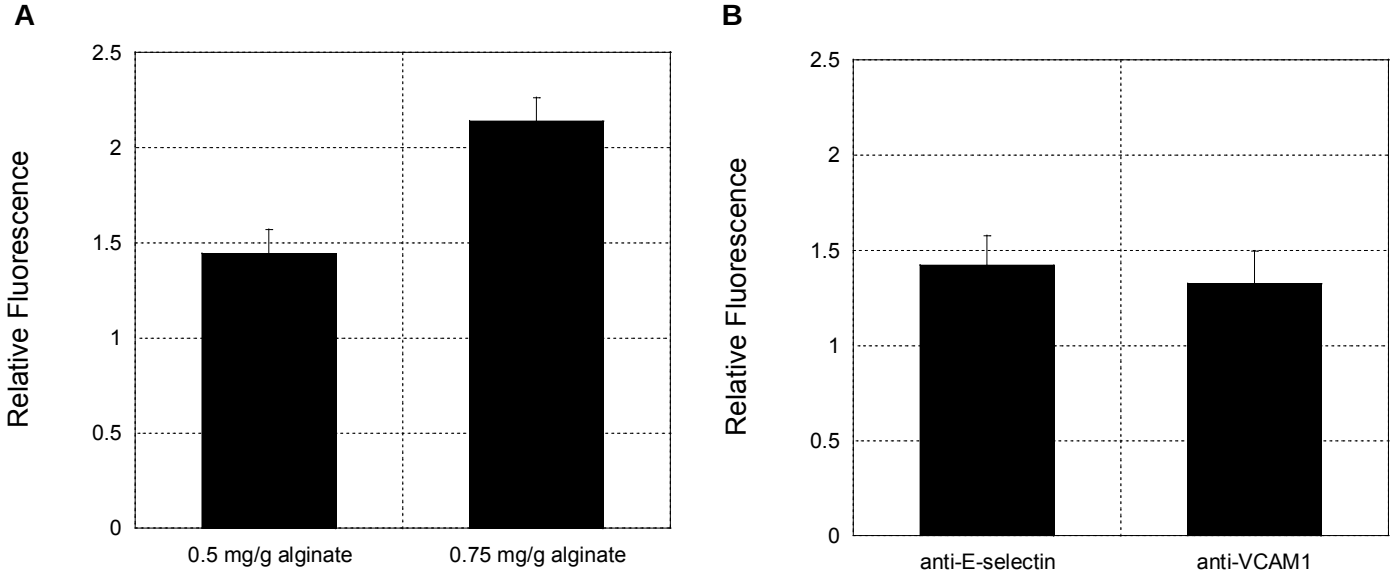

Figure 5.6: Molecular surface density analysis. Relative fluorescence of (A) increasing concentrations of FITC-labeled secondary antibodies conjugated directly to the alginate surface and (B) secondary antibody-labeled primary antibodies conjugated to alginate at 0.5 mg antibody/g alginate. Error bars are reported as standard error with n = 4.

5.5 Dynamic Cell Adhesion

ECs temporally upregulate VCAM1 and E-selectin in response to cytokine stimulation in well-characterized patterns [80]. We have previously quantified the increase in VCAM1 and E-selectin surface expression after EC stimulation with 5 ng/mL IL-1α for 6 h [85]. Before being seeded onto functionalized alginate hydrogels, ECs were activated to mimic the expression of CAMs observed in vascular disease [80].

Cell adhesion onto hydrogels modified with varying ratios of anti-VCAM1:anti-E-selectin was compared to adhesion on unmodified and RGD-modified alginate. The adhesion properties of non-activated ECs were first evaluated via centrifugation at 300 × g 24 h post-seeding (**Fig. 5.7**). Non-activated ECs exhibited CAM-independent binding. Hydrogels modified with 0:1, 1:1, or 1:0 anti-VCAM1:anti-E-selectin had similar binding to the unmodified condition. Activated ECs were then seeded onto hydrogels for 4 or 24 h, and adhesion is examined via the centrifugation assay. As previously described, the cell retention ratio compares the number of cells adhered after gel centrifugation to the number of cells adhered after gel inversion [183]. Gels modified with both antibodies had the highest cell retention after centrifugation at 300 × g 4 h post-seeding; RGD-modified gels exhibited the lowest adhesion relative to modified hydrogels (**Fig. 5.8A**). Cell retention was greatest on alginate hydrogels modified with a 1:1 ratio of anti-VCAM1:anti-E-selectin than RGD, anti-E-selectin, or anti-VCAM1-modified hydrogels after centrifugation at 300 × g 24 h post-seeding (**Fig. 5.8B**).

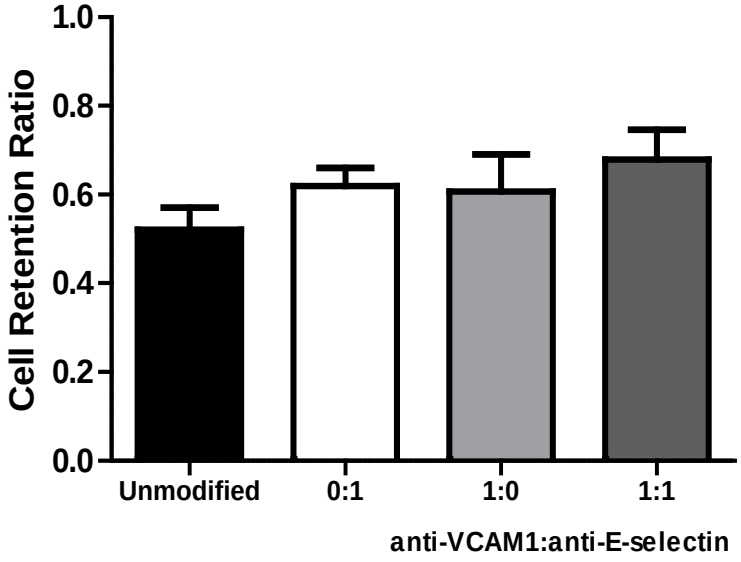

Figure 5.7: Unstimulated EC retention. Unstimulated ECs upon centrifugation at 300 × g 24 h after cell seeding onto hydrogels were examined. Cell retention ratio is defined as ratio of cells remaining on gels after centrifugation divided by cells retained on non-centrifuged samples. Error bars are reported as standard error with n = 4. No statistically significant differences were found between conditions using two-way ANOVA analysis.

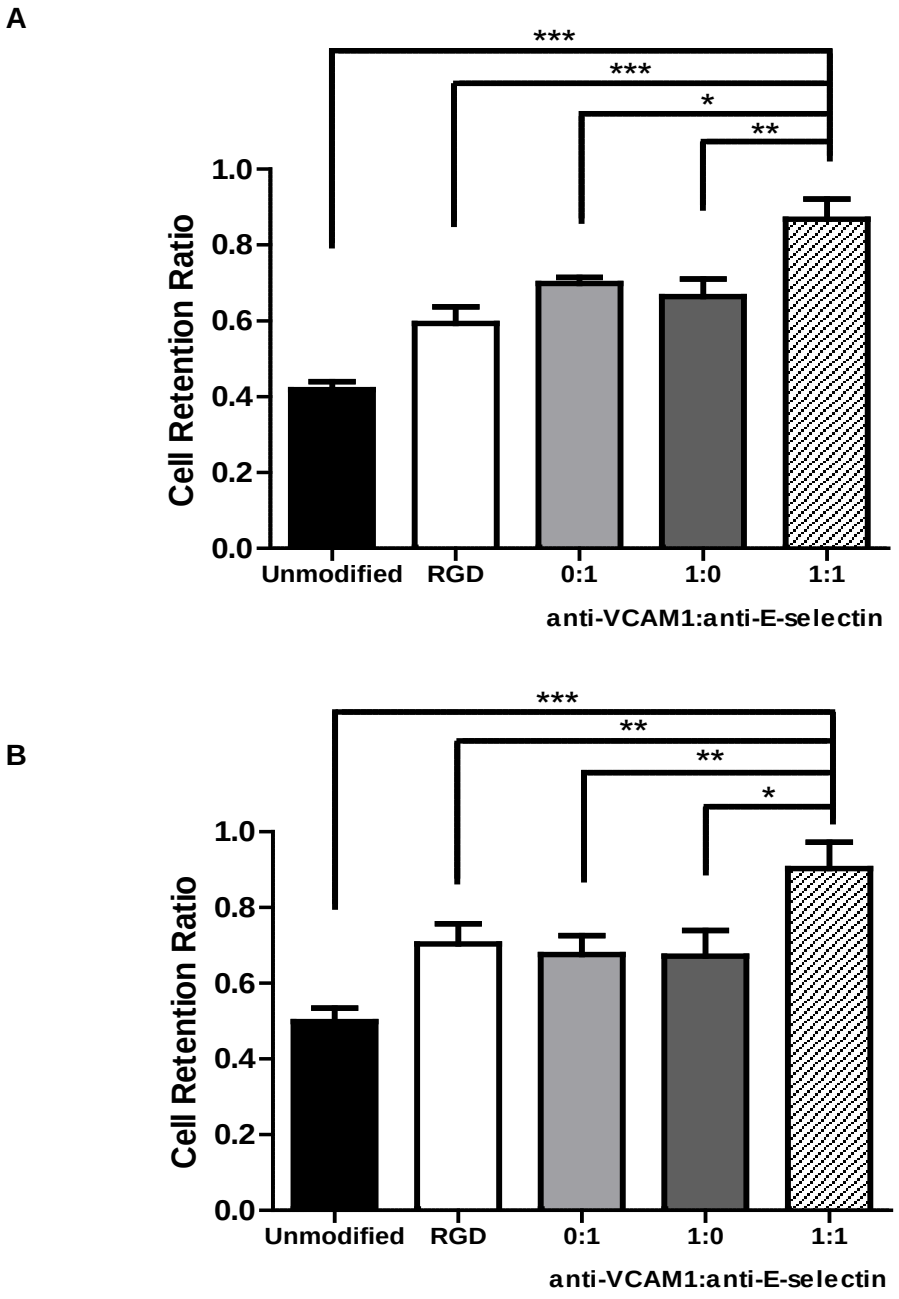

Figure 5.8: Cell adhesion dynamics. Retention of ECs stimulated with IL-1α (5 ng/mL for 6 h) seeded onto antibody-modified hydrogels upon centrifugation at 300 × g (A) 4 h and (B) 24 h after cell seeding onto hydrogels. Error bars are reported as standard error with n = 4. Statistical significance was evaluated using two-way ANOVA with *$p < 0.05$, **$p < 0.01$, and ***$p < 0.001$. Statistically significant differences in cell retention ratios were also found between

Figure 5.8 (Continued): unmodified hydrogels and RGD ($p < 0.05$), anti-E-selectin ($p < 0.01$), and anti-VCAM1-modified ($p < 0.01$) gels centrifuged 4 h after seeding as well as between unmodified and RGD ($p < 0.05$) gels centrifuged 24 h after seeding.

5.6 Cell Adhesion Strength on Alginate Hydrogels

The strength of cell adhesion was evaluated by subjecting alginate hydrogels to increasing centrifugation forces of up to 700 × g (2.5×10^{-5} dynes) and subsequently quantifying the cell retention ratio (**Fig. 5.9**). Cell retention on all hydrogel types decreased with increasing centrifugal force. However, at all centrifugation speeds, alginate hydrogels modified with a 1:1 ratio of anti-VCAM1:anti-E-selectin exhibited the highest cell retention. Statistically significant differences in cell retention ratios were found between hydrogels modified with a 1:1 ratio of anti-VCAM1:anti-E-selectin and all other conditions. This indicated the increased strength of cell adhesion to dual antibody conjugated hydrogels at higher forces.

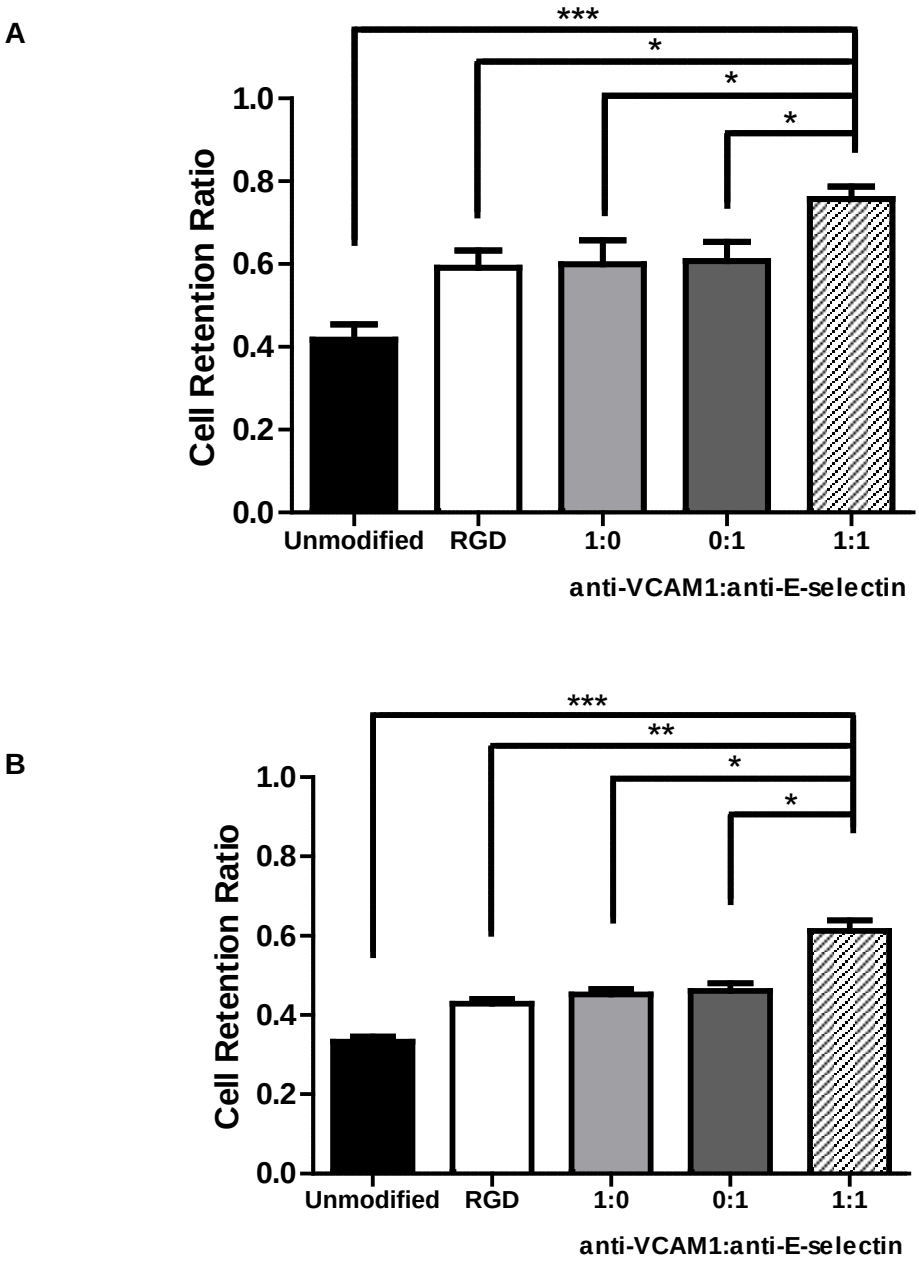

Figure 5.9: Cell adhesion strength. Retention of ECs stimulated with IL-1α (5 ng/mL for 6 h) seeded onto antibody-modified hydrogels upon centrifugation at (A) 500 × g and (B) 700 × g 24 h after cell seeding onto hydrogels. Error bars are reported as standard error with n = 4. Statistical significance is calculated using two-way ANOVA analysis with *$p < 0.05$, **$p < 0.01$, and ***$p < 0.001$. Statistically significant differences in cell retention ratios were also found

Figure 5.9 (Continued): between unmodified hydrogels and RGD ($p < 0.05$), anti-E-selectin ($p < 0.05$), and anti-VCAM1-modified ($p < 0.05$) gels centrifuged at 500 × g.

5.7 Discussion

We have engineered a dual antibody-functionalized alginate hydrogel that exhibited stronger cell adhesion than hydrogels modified with antibody or RGD alone. Engineering cooperative EC adhesion to alginate hydrogels may be used as an alternative, minimally-invasive method to remodel vessels. The proposed alginate gel has the ability to form *in situ* by rapid ionic crosslinking, conform to any geometry, and adhere to ECs. These characteristics may be useful for space-filling applications that benefit from EC adhesion, including the occlusion of wide-necked or enlarged aneurysms.

Previous studies have demonstrated that cell adhesion can be modulated by varying substrate stiffness. Pelham et al. showed that cell adhesion and spreading increased when the moduli of polyacrylamide gels increased from 5 to 70 kPa [146]. Differences in adhesion onto antibody functionalized PVA hydrogels with stiffnesses ranging from 170 to 450 kPa showed a similar trend [183]. Here, alginate hydrogels were synthesized with Young's moduli varying from 34-70 kPa (**Fig. 5.3**). If necessary, alginate stiffness can be further tuned by altering the composition of guluronic and mannuronic acid [181]. The mechanical properties of the ascending aorta (47-76 kPa) and carotid arteries (34-63 kPa) are estimated to fall within a similar range [171]. Alginate hydrogel stiffness may be used to tailor cell adhesion and spreading.

Adhesion is also dependent on cellular surface chemistry. Previous work has demonstrated that RGD surface density and spatial organization influences cell adhesion. Enhanced cell adhesion strength is attributed to reorganization of actin filaments in response to

RGD clustering patterns [145]. Instead of exploiting integrin-matrix interactions, we have taken advantage of inflammation-induced CAM overexpression to increase adhesion between the antibody-modified hydrogel and the endothelium. Both E-selectin and VCAM1 are upregulated on ECs during inflammation [61]. Cytokine activation mimics this phenomenon *in vitro* [80, 85]. We have shown previously that activated ECs exhibited maximal binding of drug delivery vehicles presenting a 1:1 ratio of anti-VCAM1:anti-E-selectin. Based on this prior work, we have conjugated three ratios of anti-VCAM1:anti-E-selectin to alginate surfaces to examine cooperative adhesion. Successful modification of hydrogel surfaces was confirmed using XPS, AFM, and fluorescence measurements of secondary antibodies (**Fig. 5.4-5.6**). The molecular density of all modified hydrogels was similar (**Fig. 5.6B**).

We evaluated whether cell adhesion was time-dependent. Adhesion to RGD-modified surfaces after centrifugation at 300 × g increased by 18.5% between 4 and 24 h post-seeding (**Fig. 5.8**), which may be due to increasing integrin-ligand bonds over time [195, 196]. In contrast, cell adhesion to antibody-modified hydrogels remained similar between 4 and 24 h, suggesting that antibody-mediated cell binding is independent of integrin-matrix interactions.

Dual antibody-presenting alginate hydrogels enabled cooperative adhesion to activated ECs. As centrifugation forces increase from 300 to 700 × g (i.e., 1.1×10^{-5} -2.5×10^{-5} dynes), activated EC adhesion was consistently greater on hydrogels presenting a 1:1 ratio of anti-VCAM1:anti-E-selectin relative to anti-VCAM1, anti-E-selectin or RGD-modified hydrogels (**Fig. 5.9**). Cell retention declined by 32.2% when the force increased by 133%.

The cell retention ratio reported herein for hydrogels with a 1:1 anti-VCAM1:anti-E-selectin ratio was comparable to previously published work (0.6 for 700 × g). For example, a cell

retention ratio of 0.2 was reported when human glioma cells adhered to fibronectin-coated surfaces were subjected to a force of 2.8×10^{-5} dynes [197]. This force was comparable to the one used in our study; however, our cell retention ratio was three times greater. Furthermore, the retention ratio between non-activated human ECs and polymorphonuclear leukocytes was 0.6 at 600 × g [198]. Our retention ratio was similar despite using a greater force. Cooperative adhesion of ECs to antibody-functionalized matrices provides an opportunity to engineer adhesion strength without altering number and organization of binding sites.

We measured cell adhesion strength by modifying alginate with different ratios of anti-VCAM1 and anti-E-selectin. At similar modification densities, hydrogels presenting a 1:1 ratio of anti-VCAM1:anti-E-selectin showed enhanced, synergistic cellular binding relative to those presenting single antibodies or RGD alone. Therefore, dual functionalized hydrogels may be used to engineer cell adhesion for improving current treatments for cerebral aneurysms or for vascular remodeling. This results of this work have been published in Rafat et al. *Acta Biomaterialia* 2012 [199].

5.8 Experimental Challenges

Although alginate hydrogels can be fabricated more quickly than PVA, rapid crosslinking of alginate caused the retention of air bubbles, which resulted in uneven hydrogel densities. We improved our mixing technique and polymerized the gels between glass plates to minimize air bubble formation. A second challenge was that alginate hydrogels were not optically clear after cell culture, which potentially interfered with fluorescence measurements. Future work should dissolve alginate in MES buffer rather than PBS to minimize the cloudy appearance.

6 FUTURE DIRECTIONS

In this section, we propose future experiments that can be extended from our previous aims.

6.1 Further *in vitro* Experiments

3D Computational Model

We have collaborated with Prof. Efthimios Kaxiras to evaluate 3D aneurysm geometries. In this study, 3D geometries for three patients were obtained via a GE Computed Tomography (CT) scanner from Dr. James Rabinov at Massachusetts General Hospital and processed by Harvard graduate student Amanda Peters Randles and Joseph Insley from the Argonne National Laboratory. The CT angiography data provided was segmented using Vitrea workstations from Vital Images. The wall shear stress and velocity profiles of blood flow in the patient aneurysms were produced through the Lattice Boltzmann method (LBM) [200-202]. LBM is a low-Mach, weakly-compressible fluid solver that reproduces hydrodynamics in the continuum limit. The volume from the CT data was filled with a regular array of lattice points and a minimal form of the classical Boltzmann equation (Eq. 6.1) was solved for each lattice point.

$$f_p\left(x + c_p\Delta t, t + \Delta t\right) = f_p(x,t) - \omega\Delta t\left(f_p - f_p^{eq}\right)(x,t) + \Delta f_p(x,t) \quad (6.1)$$

Here, ω is the relaxation frequency and f_p^{eq} represents the local equilibrium distribution. The basic quantity $f_p(x, t)$ is the distribution function representing the probability of finding, at mesh location x and at time t, a "fluid particle" traveling with discrete velocity c_p. The fluid populations are advanced in a timestep Δt through the equation.

Information travels along straight lines defined by a set of discrete speeds. In this model, we used a D3Q19 lattice (19 speeds in 3D space). This is shown in **Figure 6.1** [203].

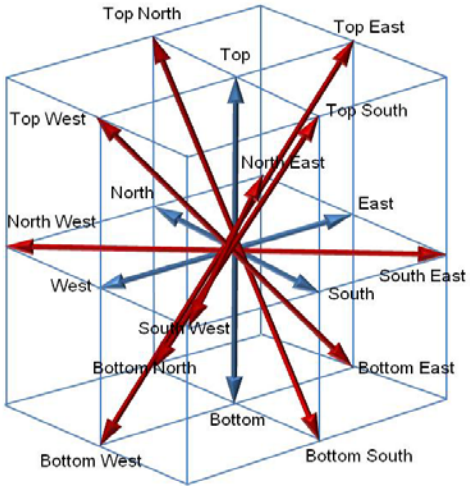

Figure 6.1: D3Q19 stencil used in the computational model.

An advantage of LBM is that shear stress is easily calculated as a linear combination of the discrete populations at each lattice point as shown in Equations 6.2 and 6.3 below.

$$S(\vec{x}_\omega, t) = \sqrt{(\overleftrightarrow{\sigma}:\overleftrightarrow{\sigma})(\vec{x}_\omega, t)} \tag{6.2}$$

$$\overleftrightarrow{\sigma}(\vec{x}, t) = \frac{\nu\omega}{c_s^2}\sum_i \vec{c}_i\vec{c}_i\left(f_i - f_i^{eq}\right)(\vec{x}, t) \tag{6.3}$$

where S is the shear stress, $\overleftrightarrow{\sigma}$ is the stress tensor, ν is the kinematic viscosity, and $c_s = \frac{1}{\sqrt{3}}$ is the speed of sound. The simulation was run at a 10 μm resolution. The fluid kinematic viscosity is 4×10^{-6} m^2/s, and the density is 1000 kg/m^3. As in the 2D models in COMSOL, the no slip boundary condition was applied at the walls. We assumed 3D, steady, laminar flow in a rigid wall model of the vessels. The simulations were executed at Harvard SEAS on the resonance GPU cluster using multi-scale physics software (MUPHY) code from Prof. Kaxiras's group.

Preliminary results elucidated the velocity and shear stress profiles for all three patients (**Figs. 6.2-6.4**). In all cases, fluid flow and shear stress were markedly decreased in the aneurysm area. In future studies, we can conduct a systematic comparison of how changes in aneurysm geometry affect 3D flow patterns.

A

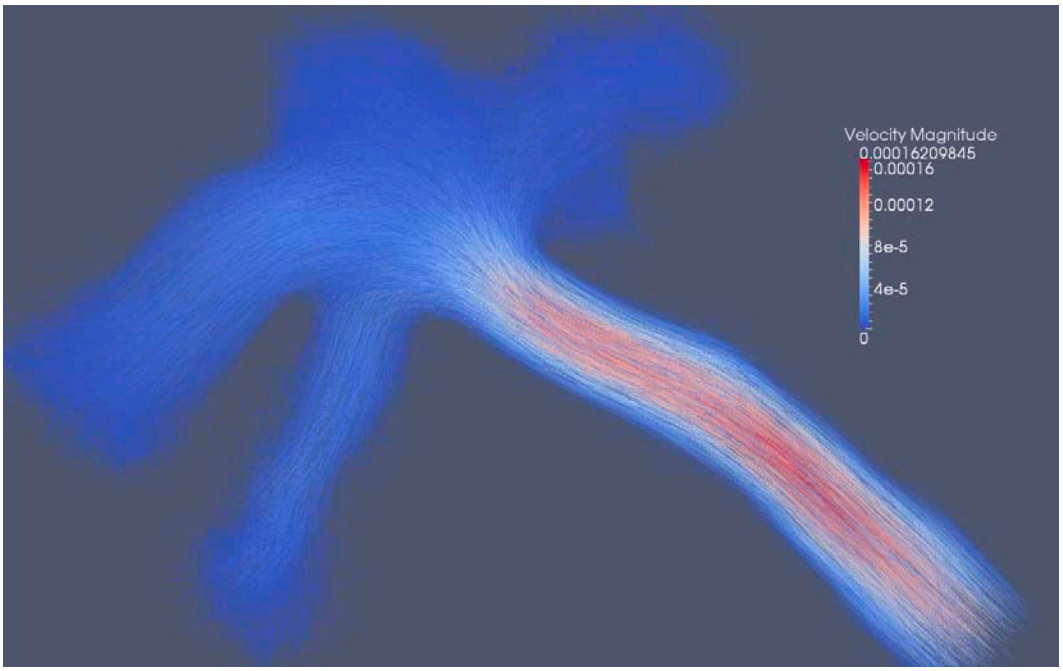

B

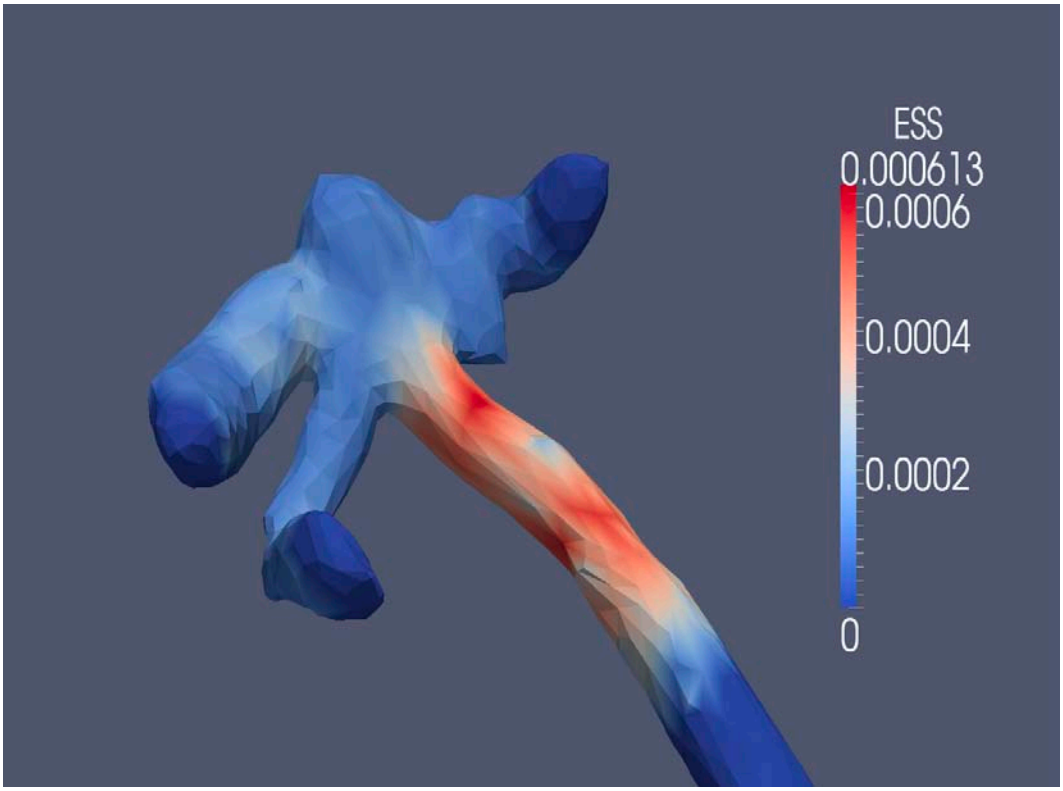

Figure 6.2: 3D (A) velocity and (B) shear stress data for patient 1.

A

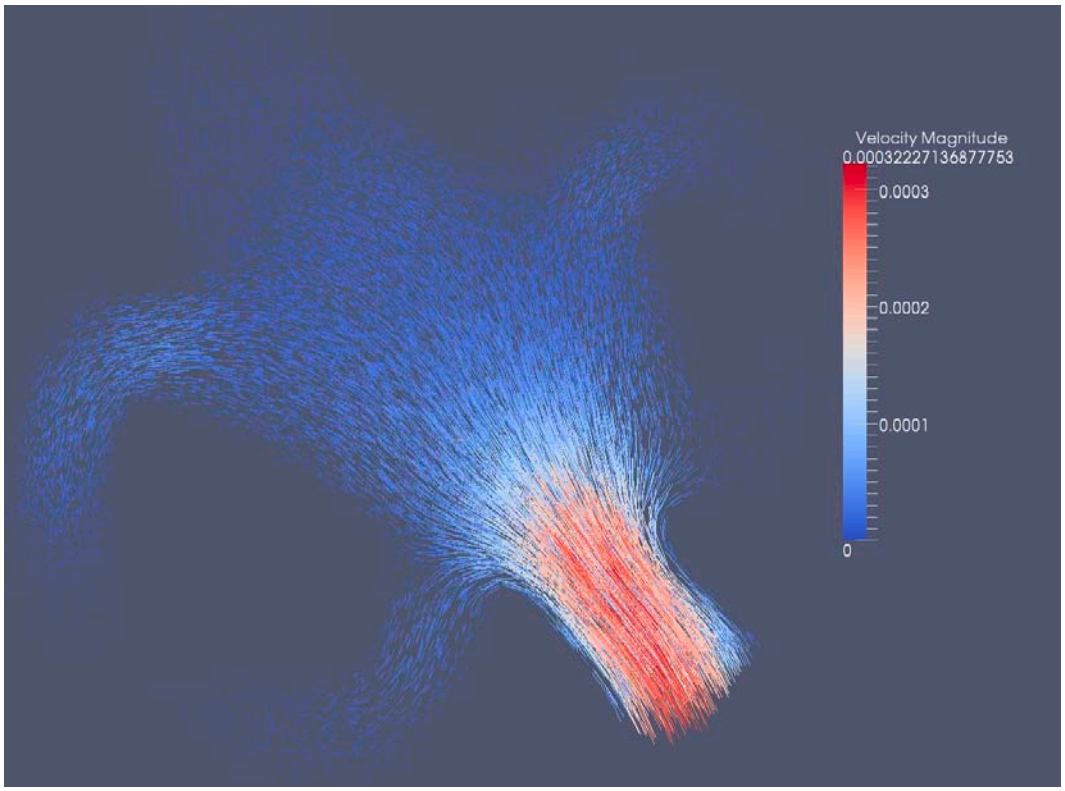

B

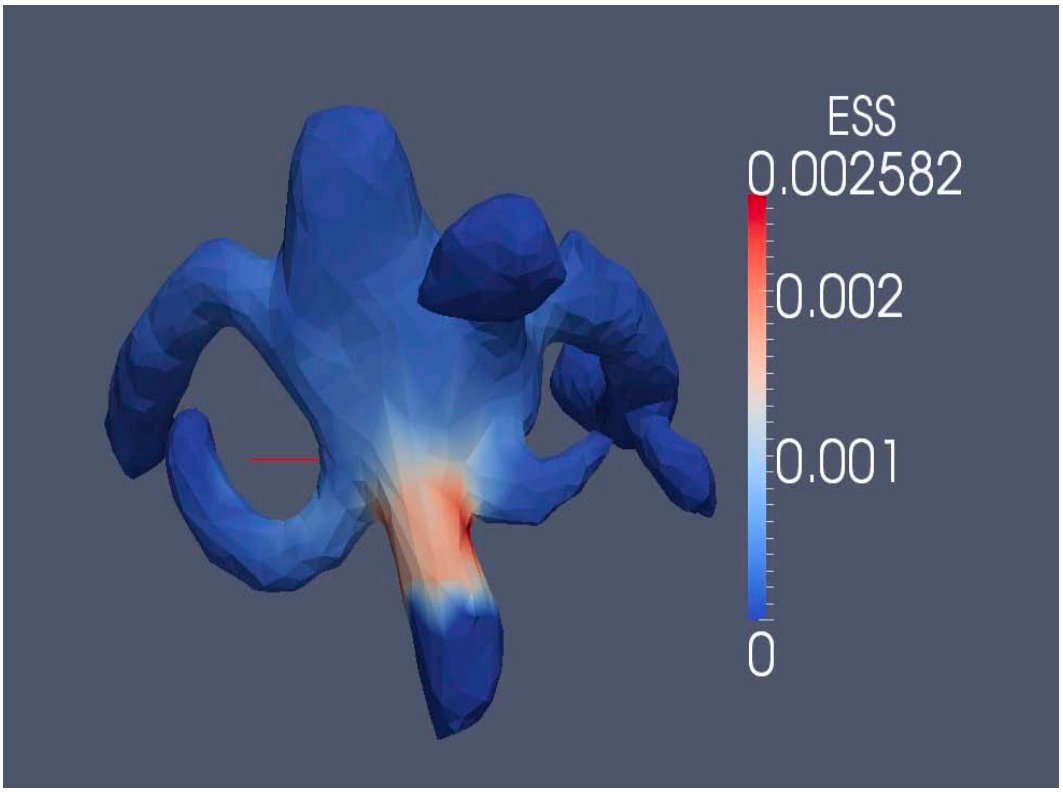

Figure 6.3: 3D (A) velocity and (B) shear stress data for patient 2.

A

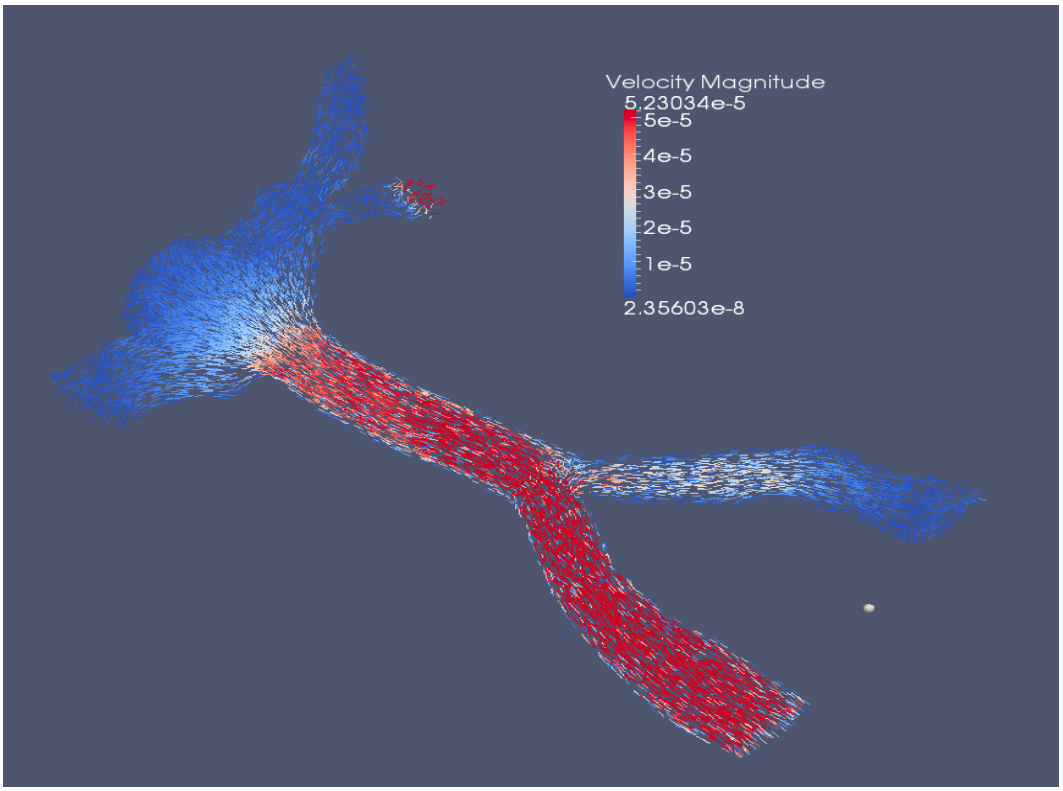

B

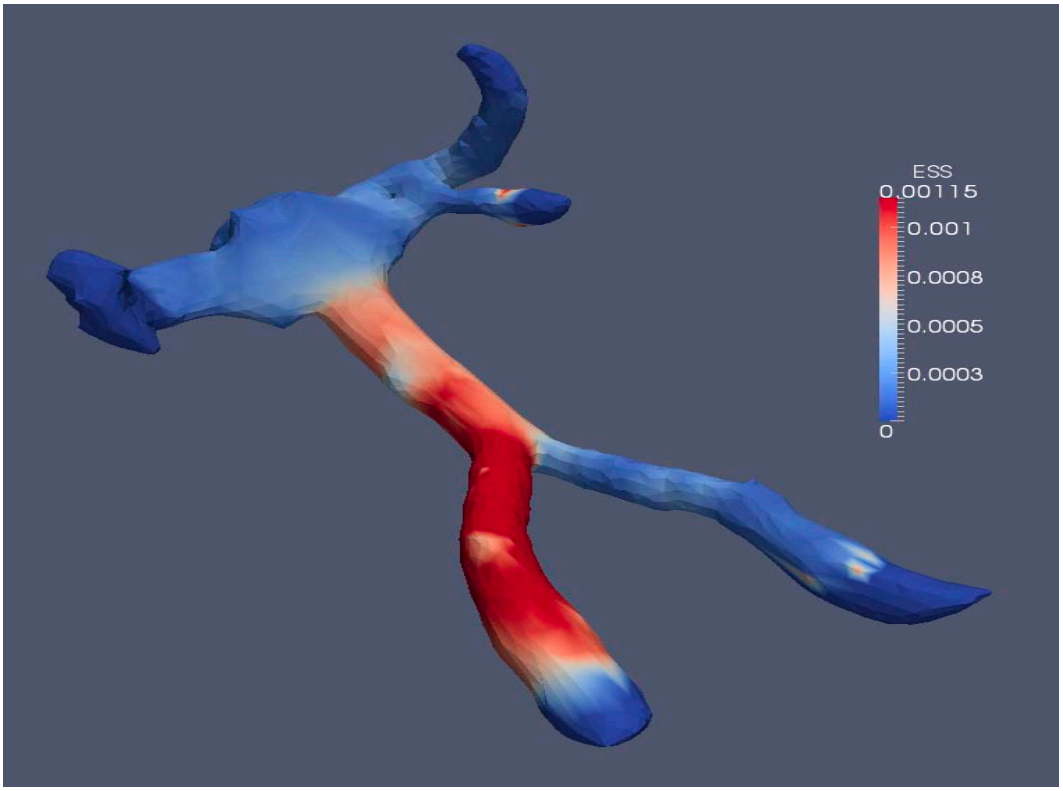

Figure 6.4: 3D (A) velocity and (B) shear stress data for patient 3.

Radiopacity

An important issue in designing an embolic agent is to include radiopaque properties since a potential treatment must be monitored *in vivo*. As such, contrast agents such as tantalum or bismuth trioxide are commonly used in the clinic [204]. To avoid the possibility of cytotoxic effects of the agent leaking out into the surrounding vasculature, iodine can be covalently bound to the modified PVA. This process has been shown previously not to interfere with hydrogel formation [205]. Dry PVA can be mixed with dry pyridine and stirred for 2 h. The pyridine is removed with a rotary evaporator. The residue is dissolved in dry DMSO at 60^{o}C free from moisture. The solution is then cooled to 45^{o}C. In dichloromethane, 4-iodobenzoyl chloride (11.5 mmol) is added dropwise. Triethylamine is added in excess. After cooling to room temperature and stirring for 2 h, the solution can be added to an 80/20 solvent mixture of diethylether and acetone. The precipitate can be collected, washed with water, and dried under vacuum. The full chemical structure for the modified PVA is shown in **Figure 6.5** below.

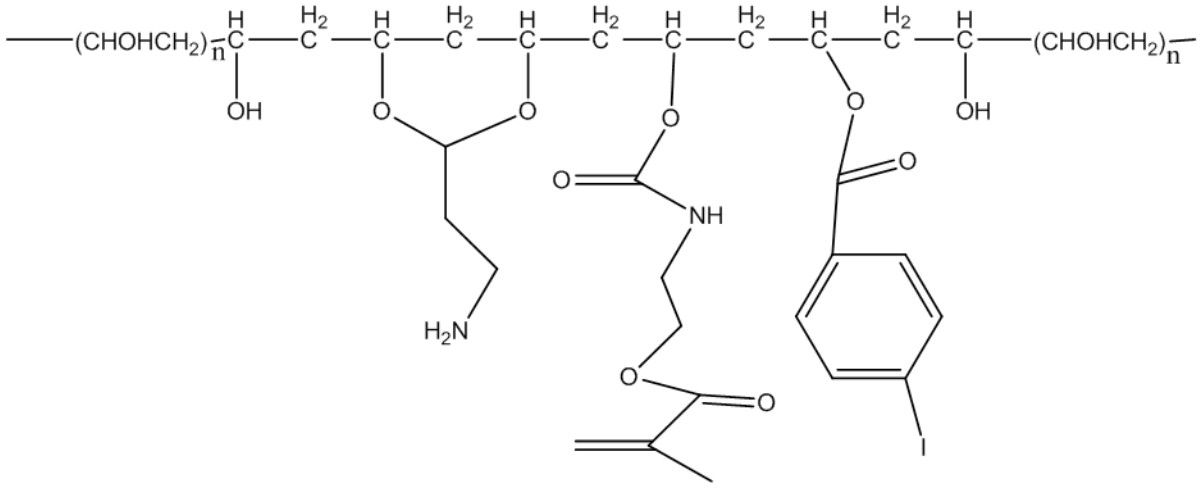

Figure 6.5: Chemical structure of PVA modification to include radiopacity. Proposed PVA gel with an amine group for bioconjugation, a photopolymerizable group, and an iodine group for radiopacity.

Examination of in situ Polymerization

A novel fluidic device can be constructed in order to examine *in situ* polymerization of PVA and alginate hydrogels as well as the ability of the hydrogels to withstand hemodynamic forces. Soft lithography can be used to create aneurysm-shaped devices from polydimethyl siloxane (PDMS) [206]. Briefly, master channels of 1.5 mm height can be machined into Delrin blocks with representative bifurcating aneurysm geometries. The length and width of the daughter vessel can match the 2D computational studies at 30 mm and 3 mm, respectively. The length and width of the parent vessel can be set to 40 mm and 4 mm, respectively. The aneurysm height and width can be variable. Initial devices have height to width ratios of 0.5 (height 1 mm, width 2 mm) and 1 (height 2 mm, width 2 mm). PDMS elastomer (Sylgard 184, Dow Corning) is made by mixing base to curing agent in a 10:1 ratio by mass. The elastomer is poured onto the master, degassed, and cured at 65^{o}C for 1 hr. The PDMS construct can then be treated with oxygen plasma and adhered to a glass slide (**Fig. 6.6**). Inlet and outlet holes of 1.5 mm can be made to allow for fluid flow. PDMS is an ideal material for biological flow experiments because of its variable elasticity, transparency, oxygen permeability, and biocompatibility [207].

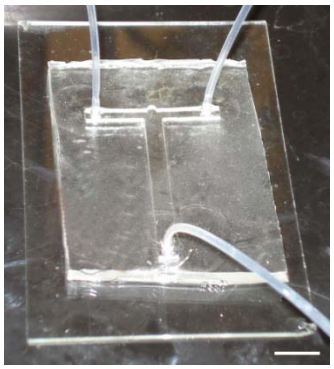

Figure 6.6: *In vitro* aneurysm device. A height to width ratio of 0.5 is shown here. Scale bar is 1.0 cm.

Quantification of Molecules on Modified Hydrogel Surfaces

Although we have extensively proven successful modification and confirmed that modification results in the same relative molecular density on hydrogel surfaces, we have not quantified the exact number of molecules present on our hydrogels. Future experiments can use radiolabeled antibodies for the determination of molecular surface density [76].

6.2 *In vivo* Experiments

The PVA and alginate hydrogels designed in this dissertation are versatile and can be used for a wide variety of space-filling applications where *in situ* polymerization is needed. Our work can be extended to determine the efficacy of these hydrogels as embolic materials for the treatment of cerebral aneurysms. Hydrogels can be modified in bulk before gelation for *in vivo* feasibility [156].

Various animal models for aneurysms have been developed in rats, mice, monkeys, and rabbits [15-20]. Because of vasculature size and ease of access, a rabbit model can be used in future *in vivo* procedures. Animal experiments can be performed as previously described [17]. New Zealand white female rabbits between 3 and 4 kg can be used. Acepromazine (1 mg/kg), ketamine (75 mg/kg), and xylazine (5 mg/kg) can be injected intramuscularly for the induction of anesthesia. The origin of the right common carotid artery (RCCA) can be exposed surgically while the surrounding tissue can be removed. The RCCA can be occluded distally using silk ligature, and a temporary clip will be placed at the RCCA origin. An angiocatheter can be used to administer porcine elastase into the lumen. Upon incubation for 20 min, the area proximal to the cannulation site can be tied so that the clip can be released. The skin of the animal can be closed with vicryl suture. 21 days after aneurysm initiation, angiography can be performed to

assess aneurysm development. Once aneurysms are developed in rabbits, the effectiveness of modified PVA or alginate hydrogels can be tested in comparison to the current treatment methods of coiling or clipping.

6.3 Dissertation Summary

We first used computational modeling to evaluate the effects of changing aneurysm geometry on flow patterns and shear stress. Based on the finding that small changes in geometry resulted in significant changes in flow patterns and shear stress, we then determined the effects of changing shear and inflammation on EC surface expression. Taken together, the results were used to fabricate biomaterials for aneurysm occlusion. Specifically, we designed PVA and alginate that could polymerize *in situ*, conform to any geometry, and adhere strongly and synergistically to activated endothelium. These results may be useful in designing new treatments for cerebral aneurysms.

Overall, this dissertation determined that the presentation of two antibodies on hydrogel surfaces resulted in synergistic, cooperative binding of endothelial cells. We established that cell adhesion onto hydrogels may be greatly enhanced by complementing activated EC surface expression of CAMs typically upregulated during inflammation. These findings may be extended to the development of therapies where firm cell adhesion is necessary, such as a vascular embolic agent that must withstand hemodynamic forces.

7 REFERENCES

[1] Lasheras JC. The Biomechanics of Arterial Aneurysms. Annu. Rev. Fluid Mech. 2007; 39: 293-319.

[2] Peters DG, Kassam AB, Feingold E, Heidrich-O'Hare E, Yonas H, Ferrell RE, Brufsky A. Molecular anatomy of an intracranial aneurysm: coordinated expression of genes involved in wound healing and tissue remodeling. Stroke 2001; 32: 1036-1042.

[3] Wiebers DO, Torner JC, Meissner I. Impact of unruptured intracranial aneurysms on public health in the United States. Stroke 1992; 23: 1416-1419.

[4] McCormick WF, Acosta-Rua GJ. The size of intracranial saccular aneurysms. An autopsy study. J Neurosurg 1970; 33: 422-427.

[5] Wiebers DO, Whisnant JP, Huston J, 3rd, Meissner I, Brown RD, Jr., Piepgras DG, Forbes GS, Thielen K, Nichols D, O'Fallon WM, Peacock J, Jaeger L, Kassell NF, Kongable-Beckman GL, Torner JC. Unruptured intracranial aneurysms: natural history, clinical outcome, and risks of surgical and endovascular treatment. Lancet 2003; 362: 103-110.

[6] Zhang B, Fugleholm K, Day LB, Ye S, Weller RO, Day IN. Molecular pathogenesis of subarachnoid haemorrhage. Int J Biochem Cell Biol 2003; 35: 1341-1360.

[7] Perktold K, Kenner T, Hilbert D, Spork B, Florian H. Numerical blood flow analysis: arterial bifurcation with a saccular aneurysm. Basic research in cardiology 1988; 83: 24-31.

[8] Zhang B, Fugleholm K, Day LB, Ye S, Weller RO, Day IN. Molecular pathogenesis of subarachnoid haemorrhage. The international journal of biochemistry & cell biology 2003; 35: 1341-1360.

[9] Imbesi SG, Kerber CW. Analysis of slipstream flow in two ruptured intracranial cerebral aneurysms. AJNR Am J Neuroradiol 1999; 20: 1703-1705.

[10] Tateshima S, Murayama Y, Villablanca JP, Morino T, Nomura K, Tanishita K, Vinuela F. In vitro measurement of fluid-induced wall shear stress in unruptured cerebral aneurysms harboring blebs. Stroke 2003; 34: 187-192.

[11] Shojima M, Oshima M, Takagi K, Torii R, Hayakawa M, Katada K, Morita A, Kirino T. Magnitude and role of wall shear stress on cerebral aneurysm: computational fluid dynamic study of 20 middle cerebral artery aneurysms. Stroke 2004; 35: 2500-2505.

[12] Cheng CP, Parker D, Taylor CA. Quantification of wall shear stress in large blood vessels using Lagrangian interpolation functions with cine phase-contrast magnetic resonance imaging. Ann Biomed Eng 2002; 30: 1020-1032.

[13] Cebral JR, Pergolizzi RS, Jr., Putman CM. Computational fluid dynamics modeling of intracranial aneurysms: qualitative comparison with cerebral angiography. Academic radiology 2007; 14: 804-813.

[14] Meng H, Wang Z, Hoi Y, Gao L, Metaxa E, Swartz DD, Kolega J. Complex Hemodynamics at the Apex of an Arterial Bifurcation Induces Vascular Remodeling Resembling Cerebral Aneurysm Initiation. Stroke; a journal of cerebral circulation 2007; 38: 1924-1931.

[15] Altes TA, Cloft HJ, Short JG, DeGast A, Do HM, Helm GA, Kallmes DF. 1999 ARRS Executive Council Award. Creation of saccular aneurysms in the rabbit: a model suitable for testing endovascular devices. American Roentgen Ray Society. Ajr 2000; 174: 349-354.

[16] Ding YH, Danielson MA, Kadirvel R, Dai D, Lewis DA, Cloft HJ, Kallmes DF. Modified technique to create morphologically reproducible elastase-induced aneurysms in rabbits. Neuroradiology 2006; 48: 528-532.

[17] Hoh BL, Rabinov JD, Pryor JC, Ogilvy CS. A modified technique for using elastase to create saccular aneurysms in animals that histologically and hemodynamically resemble aneurysms in human. Acta neurochirurgica 2004; 146: 705-711.

[18] Hashimoto N, Handa H, Hazama F. Experimentally induced cerebral aneurysms in rats. Surgical neurology 1978; 10: 3-8.

[19] Hashimoto N, Kim C, Kikuchi H, Kojima M, Kang Y, Hazama F. Experimental induction of cerebral aneurysms in monkeys. J Neurosurg 1987; 67: 903-905.

[20] Morimoto M, Miyamoto S, Mizoguchi A, Kume N, Kita T, Hashimoto N. Mouse model of cerebral aneurysm: experimental induction by renal hypertension and local hemodynamic changes. Stroke 2002; 33: 1911-1915.

[21] Meng H, Swartz DD, Wang Z, Hoi Y, Kolega J, Metaxa EM, Szymanski MP, Yamamoto J, Sauvageau E, Levy EI. A model system for mapping vascular responses to complex hemodynamics at arterial bifurcations in vivo. Neurosurgery 2006; 59: 1094-1100; discussion 1100-1091.

[22] Chatziprodromou I, Tricoli A, Poulikakos D, Ventikos Y. Haemodynamics and wall remodelling of a growing cerebral aneurysm: a computational model. Journal of biomechanics 2007; 40: 412-426.

[23] Sadamasa N, Nozaki K, Takagi Y, Moriwaki T, Kawanabe Y, Ishikawa M, Hashimoto N. Cerebral aneurysm progression suppressed by blockage of endothelin B receptor. J Neurosurg 2007; 106: 330-336.

[24] Sadamasa N, Nozaki K, Hashimoto N. Disruption of gene for inducible nitric oxide synthase reduces progression of cerebral aneurysms. Stroke 2003; 34: 2980-2984.

[25] Moriwaki T, Takagi Y, Sadamasa N, Aoki T, Nozaki K, Hashimoto N. Impaired progression of cerebral aneurysms in interleukin-1beta-deficient mice. Stroke 2006; 37: 900-905.

[26] Aoki T, Kataoka H, Morimoto M, Nozaki K, Hashimoto N. Macrophage-derived matrix metalloproteinase-2 and -9 promote the progression of cerebral aneurysms in rats. Stroke 2007; 38: 162-169.

[27] Tulamo R, Frosen J, Junnikkala S, Paetau A, Pitkaniemi J, Kangasniemi M, Niemela M, Jaaskelainen J, Jokitalo E, Karatas A, Hernesniemi J, Meri S. Complement activation associates with saccular cerebral artery aneurysm wall degeneration and rupture. Neurosurgery 2006; 59: 1069-1076; discussion 1076-1067.

[28] Malek A, Izumo S. Physiological fluid shear stress causes downregulation of endothelin-1 mRNA in bovine aortic endothelium. Am J Physiol 1992; 263: C389-396.

[29] Malek AM, Gibbons GH, Dzau VJ, Izumo S. Fluid shear stress differentially modulates expression of genes encoding basic fibroblast growth factor and platelet-derived growth factor B chain in vascular endothelium. J Clin Invest 1993; 92: 2013-2021.

[30] Malek AM, Izumo S. Control of endothelial cell gene expression by flow. Journal of biomechanics 1995; 28: 1515-1528.

[31] Malek AM, Izumo S, Alper SL. Modulation by pathophysiological stimuli of the shear stress-induced up-regulation of endothelial nitric oxide synthase expression in endothelial cells. Neurosurgery 1999; 45: 334-344; discussion 344-335.

[32] Malek AM, Jackman R, Rosenberg RD, Izumo S. Endothelial expression of thrombomodulin is reversibly regulated by fluid shear stress. Circulation research 1994; 74: 852-860.

[33] Qureshi AI, Janardhan V, Hanel RA, Lanzino G. Comparison of endovascular and surgical treatments for intracranial aneurysms: an evidence-based review. Lancet Neurol 2007; 6: 816-825.

[34] Brilstra EH, Rinkel GJ, van der Graaf Y, van Rooij WJ, Algra A. Treatment of intracranial aneurysms by embolization with coils: a systematic review. Stroke 1999; 30: 470-476.

[35] Alshekhlee A, Mehta S, Edgell RC, Vora N, Feen E, Mohammadi A, Kale SP, Cruz-Flores S. Hospital mortality and complications of electively clipped or coiled unruptured intracranial aneurysm. Stroke 2010; 41: 1471-1476.

[36] Regli L, Dehdashti AR, Uske A, de Tribolet N. Endovascular coiling compared with surgical clipping for the treatment of unruptured middle cerebral artery aneurysms: an update. Acta Neurochir Suppl 2002; 82: 41-46.

[37] Lanzino G, Kanaan Y, Perrini P, Dayoub H, Fraser K. Emerging concepts in the treatment of intracranial aneurysms: stents, coated coils, and liquid embolic agents. Neurosurgery 2005; 57: 449-459; discussion 449-459.

[38] Cloft HJ, Kallmes DF. Aneurysm packing with HydroCoil Embolic System versus platinum coils: initial clinical experience. AJNR Am J Neuroradiol 2004; 25: 60-62.

[39] Rossitti S. Endovascular coiling of intracranial aneurysms using bioactive coils: a single-center study. Acta Radiol 2007; 48: 565-576.

[40] Liebig T, Henkes H, Fischer S, Weber W, Miloslavski E, Mariushi W, Brew S, Kuhne D. Fibered electrolytically detachable platinum coils used for the endovascular treatment of intracranial aneurysms. Initial experiences and mid-term results in 474 aneurysms. Interv Neuroradiol 2004; 10: 5-26.

[41] Butteriss D, Gholkar A, Mitra D, Birchall D, Jayakrishnan V. Single-center experience of cerecyte coils in the treatment of intracranial aneurysms: initial experience and early follow-up results. AJNR Am J Neuroradiol 2008; 29: 53-56.

[42] White PM, Raymond J. Endovascular coiling of cerebral aneurysms using "bioactive" or coated-coil technologies: a systematic review of the literature. AJNR Am J Neuroradiol 2009; 30: 219-226.

[43] Matsumoto H, Terada T, Tsuura M, Itakura T, Ogawa A. Basic fibroblast growth factor released from a platinum coil with a polyvinyl alcohol core enhances cellular proliferation and vascular wall thickness: an in vitro and in vivo study. Neurosurgery 2003; 53: 402-407; discussion 407-408.

[44] Marx WE, Cloft HJ, Helm GA, Short JG, Do HM, Jensen ME, Kallmes DE. Endovascular treatment of experimental aneurysms by use of biologically modified embolic devices: coil-

mediated intraaneurysmal delivery of fibroblast tissue allografts. AJNR Am J Neuroradiol 2001; 22: 323-333.

[45] Fiorella D, Albuquerque FC, Han P, McDougall CG. Preliminary experience using the Neuroform stent for the treatment of cerebral aneurysms. Neurosurgery 2004; 54: 6-16; discussion 16-17.

[46] Yahia AM, Gordon V, Whapham J, Malek A, Steel J, Fessler RD. Complications of Neuroform stent in endovascular treatment of intracranial aneurysms. Neurocrit Care 2008; 8: 19-30.

[47] Higashida RT, Halbach VV, Dowd CF, Juravsky L, Meagher S. Initial clinical experience with a new self-expanding nitinol stent for the treatment of intracranial cerebral aneurysms: the Cordis Enterprise stent. AJNR Am J Neuroradiol 2005; 26: 1751-1756.

[48] Marotta TR, Gunnarsson T, Penn I, Ricci DR, McDougall I, Marko A, Bourne G, Da Costa L. A novel endovascular clip system for the treatment of intracranial aneurysms: technology, concept, and initial experimental results. Laboratory investigation. J Neurosurg 2008; 108: 1230-1240.

[49] Struffert T, Roth C, Romeike B, Grunwald IO, Reith W. Onyx in an experimental aneurysm model: histological and angiographic results. J Neurosurg 2008; 109: 77-82.

[50] Molyneux AJ, Kerr RS, Yu LM, Clarke M, Sneade M, Yarnold JA, Sandercock P. International subarachnoid aneurysm trial (ISAT) of neurosurgical clipping versus endovascular coiling in 2143 patients with ruptured intracranial aneurysms: a randomised comparison of effects on survival, dependency, seizures, rebleeding, subgroups, and aneurysm occlusion. Lancet 2005; 366: 809-817.

[51] Johnston SC, Dowd CF, Higashida RT, Lawton MT, Duckwiler GR, Gress DR. Predictors of rehemorrhage after treatment of ruptured intracranial aneurysms: the Cerebral Aneurysm Rerupture After Treatment (CARAT) study. Stroke 2008; 39: 120-125.

[52] Bevilacqua MP, Nelson RM. Endothelial-leukocyte adhesion molecules in inflammation and metastasis. Thromb Haemost 1993; 70: 152-154.

[53] Butcher EC. Leukocyte-endothelial cell recognition: three (or more) steps to specificity and diversity. Cell 1991; 67: 1033-1036.

[54] Springer TA. Traffic signals for lymphocyte recirculation and leukocyte emigration: the multistep paradigm. Cell 1994; 76: 301-314.

[55] Carlos TM, Harlan JM. Leukocyte-endothelial adhesion molecules. Blood 1994; 84: 2068-2101.

[56] Muller WA. Leukocyte-endothelial-cell interactions in leukocyte transmigration and the inflammatory response. Trends Immunol 2003; 24: 327-334.

[57] Schenkel AR, Mamdouh Z, Muller WA. Locomotion of monocytes on endothelium is a critical step during extravasation. Nat Immunol 2004; 5: 393-400.

[58] van Buul JD, Hordijk PL. Signaling in leukocyte transendothelial migration. Arterioscler Thromb Vasc Biol 2004; 24: 824-833.

[59] Rao RM, Shaw SK, Kim M, Luscinskas FW. Emerging topics in the regulation of leukocyte transendothelial migration. Microcirculation 2005; 12: 83-89.

[60] Pober JS, Cotran RS. Cytokines and endothelial cell biology. Physiol Rev 1990; 70: 427-451.

[61] Collins T, Read MA, Neish AS, Whitley MZ, Thanos D, Maniatis T. Transcriptional regulation of endothelial cell adhesion molecules: NF-kappa B and cytokine-inducible enhancers. FASEB J 1995; 9: 899-909.

[62] Garton KJ, Gough PJ, Raines EW. Emerging roles for ectodomain shedding in the regulation of inflammatory responses. J Leukoc Biol 2006; 79: 1105-1116.

[63] Poston RN, Haskard DO, Coucher JR, Gall NP, Johnson-Tidey RR. Expression of intercellular adhesion molecule-1 in atherosclerotic plaques. Am J Pathol 1992; 140: 665-673.

[64] van der Wal AC, Das PK, Tigges AJ, Becker AE. Adhesion molecules on the endothelium and mononuclear cells in human atherosclerotic lesions. Am J Pathol 1992; 141: 1427-1433.

[65] Printseva O, Peclo MM, Gown AM. Various cell types in human atherosclerotic lesions express ICAM-1. Further immunocytochemical and immunochemical studies employing monoclonal antibody 10F3. Am J Pathol 1992; 140: 889-896.

[66] Shreeniwas R, Koga S, Karakurum M, Pinsky D, Kaiser E, Brett J, Wolitzky BA, Norton C, Plocinski J, Benjamin W, et al. Hypoxia-mediated induction of endothelial cell interleukin-1 alpha. An autocrine mechanism promoting expression of leukocyte adhesion molecules on the vessel surface. J Clin Invest 1992; 90: 2333-2339.

[67] Palluy O, Morliere L, Gris JC, Bonne C, Modat G. Hypoxia/reoxygenation stimulates endothelium to promote neutrophil adhesion. Free Radic Biol Med 1992; 13: 21-30.

[68] Arnould T, Michiels C, Remacle J. Increased PMN adherence on endothelial cells after hypoxia: involvement of PAF, CD18/CD11b, and ICAM-1. Am J Physiol 1993; 264: C1102-1110.

[69] Chyatte D, Bruno G, Desai S, Todor DR. Inflammation and intracranial aneurysms. Neurosurgery 1999; 45: 1137-1146; discussion 1146-1137.

[70] Ross R. Cell biology of atherosclerosis. Annu Rev Physiol 1995; 57: 791-804.

[71] Kipshidze N, Dangas G, Tsapenko M, Moses J, Leon MB, Kutryk M, Serruys P. Role of the endothelium in modulating neointimal formation: vasculoprotective approaches to attenuate restenosis after percutaneous coronary interventions. J Am Coll Cardiol 2004; 44: 733-739.

[72] Galkina E, Ley K. Immune and inflammatory mechanisms of atherosclerosis (*). Annu Rev Immunol 2009; 27: 165-197.

[73] Ruoslahti E, Pierschbacher MD. New perspectives in cell adhesion: RGD and integrins. Science 1987; 238: 491-497.

[74] Griffith LG, Naughton G. Tissue engineering--current challenges and expanding opportunities. Science 2002; 295: 1009-1014.

[75] Palecek SP, Loftus JC, Ginsberg MH, Lauffenburger DA, Horwitz AF. Integrin-ligand binding properties govern cell migration speed through cell-substratum adhesiveness. Nature 1997; 385: 537-540.

[76] Rowley JA, Madlambayan G, Mooney DJ. Alginate hydrogels as synthetic extracellular matrix materials. Biomaterials 1999; 20: 45-53.

[77] Lutolf MP, Hubbell JA. Synthetic biomaterials as instructive extracellular microenvironments for morphogenesis in tissue engineering. Nat Biotechnol 2005; 23: 47-55.

[78] Hynes RO. Integrins: versatility, modulation, and signaling in cell adhesion. Cell 1992; 69: 11-25.

[79] Lu Z-R, Kopeckova P, Kopecek J. Antigen Responsive Hydrogels Based on Polymerizable Antibody Fab' Fragment. Macromol Biosci 2003; 3: 296-300.

[80] Bevilacqua MP, Nelson RM, Mannori G, Cecconi O. Endothelial-leukocyte adhesion molecules in human disease. Annu Rev Med 1994; 45: 361-378.

[81] Tees DFJ, Chang, K.C., Rodgers, S.D., Hammer, A. . Simulation of Cell Adhesion to Bioreactive Surfaces in Shear: The Effect of Cell Size. Ind. Eng. Chem. Res. 2002; 41: 486-493.

[82] Whitty A. Cooperativity and biological complexity. Nat Chem Biol 2008; 4: 435-439.

[83] Perlmutter-Hayman B. Cooperative Binding to Macromolecules. A Formal Approach. Acc. Chem. Res. 1986; 19: 90-96.

[84] Nugent MA, Edelman ER. Kinetics of basic fibroblast growth factor binding to its receptor and heparan sulfate proteoglycan: a mechanism for cooperactivity. Biochemistry 1992; 31: 8876-8883.

[85] Gunawan RC, Almeda D, Auguste DT. Complementary targeting of liposomes to IL-1alpha and TNF-alpha activated endothelial cells via the transient expression of VCAM1 and E-selectin. Biomaterials 2011; 32: 9848-9853.

[86] Gunawan RC, Auguste DT. The role of antibody synergy and membrane fluidity in the vascular targeting of immunoliposomes. Biomaterials 2010; 31: 900-907.

[87] Gunawan RC, Auguste DT. Immunoliposomes That Target Endothelium In Vitro Are Dependent on Lipid Raft Formation. Mol Pharm 2010; 7: 1569-1575.

[88] Chen A, Moy VT. Cross-linking of cell surface receptors enhances cooperativity of molecular adhesion. Biophys J 2000; 78: 2814-2820.

[89] Hoh BL, Sistrom CL, Firment CS, Fautheree GL, Velat GJ, Whiting JH, Reavey-Cantwell JF, Lewis SB. Bottleneck factor and height-width ratio: association with ruptured aneurysms in patients with multiple cerebral aneurysms. Neurosurgery 2007; 61: 716-722; discussion 722-713.

[90] Burleson AC, Strother CM, Turitto VT. Computer modeling of intracranial saccular and lateral aneurysms for the study of their hemodynamics. Neurosurgery 1995; 37: 774-782; discussion 782-774.

[91] Cebral JR, Castro MA, Burgess JE, Pergolizzi RS, Sheridan MJ, Putman CM. Characterization of cerebral aneurysms for assessing risk of rupture by using patient-specific computational hemodynamics models. AJNR Am J Neuroradiol 2005; 26: 2550-2559.

[92] Utter B, Rossmann JS. Numerical simulation of saccular aneurysm hemodynamics: influence of morphology on rupture risk. Journal of biomechanics 2007; 40: 2716-2722.

[93] Meng H, Wang Z, Hoi Y, Gao L, Metaxa E, Swartz DD, Kolega J. Complex hemodynamics at the apex of an arterial bifurcation induces vascular remodeling resembling cerebral aneurysm initiation. Stroke 2007; 38: 1924-1931.

[94] Gobin YP, Counord JL, Flaud P, Duffaux J. In vitro study of haemodynamics in a giant saccular aneurysm model: influence of flow dynamics in the parent vessel and effects of coil embolisation. Neuroradiology 1994; 36: 530-536.

[95] DeGroff CG, Thornburg BL, Pentecost JO, Thornburg KL, Gharib M, Sahn DJ, Baptista A. Flow in the early embryonic human heart: a numerical study. Pediatric cardiology 2003; 24: 375-380.

[96] Sakai H, Yuasa M, Onuma H, Takeoka S, Tsuchida E. Synthesis and physicochemical characterization of a series of hemoglobin-based oxygen carriers: objective comparison between cellular and acellular types. Bioconjug Chem 2000; 11: 56-64.

[97] Steiger HJ, Poll A, Liepsch D, Reulen HJ. Basic flow structure in saccular aneurysms: a flow visualization study. Heart and vessels 1987; 3: 55-65.

[98] Mantha AR, Benndorf G, Hernandez A, Metcalfe RW. Stability of pulsatile blood flow at the ostium of cerebral aneurysms. Journal of biomechanics 2009; 42: 1081-1087.

[99] Rayz VL, Boussel L, Lawton MT, Acevedo-Bolton G, Ge L, Young WL, Higashida RT, Saloner D. Numerical modeling of the flow in intracranial aneurysms: prediction of regions prone to thrombus formation. Ann Biomed Eng 2008; 36: 1793-1804.

[100] Paal G, Ugron A, Szikora I, Bojtar I. Flow in simplified and real models of intracranial aneurysms. International Journal of Heat and Fluid Flow 2007; 28: 653-664.

[101] Steiger HJ. Pathophysiology of development and rupture of cerebral aneurysms. Acta Neurochir Suppl (Wien) 1990; 48: 1-57.

[102] Ujiie H, Tachibana H, Hiramatsu O, Hazel AL, Matsumoto T, Ogasawara Y, Nakajima H, Hori T, Takakura K, Kajiya F. Effects of size and shape (aspect ratio) on the hemodynamics of saccular aneurysms: a possible index for surgical treatment of intracranial aneurysms. Neurosurgery 1999; 45: 119-129; discussion 129-130.

[103] Steiger HJ, Liepsch DW, Poll A, Reulen HJ. Hemodynamic stress in terminal saccular aneurysms: a laser-Doppler study. Heart and vessels 1988; 4: 162-169.

[104] Liepsch DW, Steiger HJ, Poll A, Reulen HJ. Hemodynamic stress in lateral saccular aneurysms. Biorheology 1987; 24: 689-710.

[105] Chen BP, Li YS, Zhao Y, Chen KD, Li S, Lao J, Yuan S, Shyy JY, Chien S. DNA microarray analysis of gene expression in endothelial cells in response to 24-h shear stress. Physiol Genomics 2001; 7: 55-63.

[106] Chien S. Effects of disturbed flow on endothelial cells. Ann Biomed Eng 2008; 36: 554-562.

[107] Hoi Y, Meng H, Woodward SH, Bendok BR, Hanel RA, Guterman LR, Hopkins LN. Effects of arterial geometry on aneurysm growth: three-dimensional computational fluid dynamics study. J Neurosurg 2004; 101: 676-681.

[108] Boussel L, Rayz V, McCulloch C, Martin A, Acevedo-Bolton G, Lawton M, Higashida R, Smith WS, Young WL, Saloner D. Aneurysm growth occurs at region of low wall shear stress: patient-specific correlation of hemodynamics and growth in a longitudinal study. Stroke 2008; 39: 2997-3002.

[109] Jou LD, Lee DH, Morsi H, Mawad ME. Wall shear stress on ruptured and unruptured intracranial aneurysms at the internal carotid artery. AJNR Am J Neuroradiol 2008; 29: 1761-1767.

[110] Hassan T, Timofeev EV, Saito T, Shimizu H, Ezura M, Matsumoto Y, Takayama K, Tominaga T, Takahashi A. A proposed parent vessel geometry-based categorization of saccular intracranial aneurysms: computational flow dynamics analysis of the risk factors for lesion rupture. J Neurosurg 2005; 103: 662-680.

[111] Cebral JR, Hendrickson S, Putman CM. Hemodynamics in a lethal basilar artery aneurysm just before its rupture. AJNR Am J Neuroradiol 2009; 30: 95-98.

[112] White CR, Frangos JA. The shear stress of it all: the cell membrane and mechanochemical transduction. Philos Trans R Soc Lond B Biol Sci 2007; 362: 1459-1467.

[113] Nerem RM. Hemodynamics and the vascular endothelium. J Biomech Eng 1993; 115: 510-514.

[114] Hahn C, Schwartz MA. Mechanotransduction in vascular physiology and atherogenesis. Nat Rev Mol Cell Biol 2009; 10: 53-62.

[115] Zhu CH, Ying DJ, Mi JH, Zhu XH, Sun JS, Cui XP. Low shear stress regulates monocyte adhesion to oxidized lipid-induced endothelial cells via an IkappaBalpha dependent pathway. Biorheology 2004; 41: 127-137.

[116] Traub O, Berk BC. Laminar shear stress: mechanisms by which endothelial cells transduce an atheroprotective force. Arterioscler Thromb Vasc Biol 1998; 18: 677-685.

[117] Bevilacqua MP. Endothelial-leukocyte adhesion molecules. Annu Rev Immunol 1993; 11: 767-804.

[118] Kline MA, O'Connor Butler ES, Hinzey A, Sliman S, Kotha SR, Marsh CB, Uppu RM, Parinandi NL. A simple method for effective and safe removal of membrane cholesterol from lipid rafts in vascular endothelial cells: implications in oxidant-mediated lipid signaling. Methods Mol Biol 2010; 610: 201-211.

[119] Spragg DD, Alford DR, Greferath R, Larsen CE, Lee KD, Gurtner GC, Cybulsky MI, Tosi PF, Nicolau C, Gimbrone MA, Jr. Immunotargeting of liposomes to activated vascular endothelial cells: a strategy for site-selective delivery in the cardiovascular system. Proc Natl Acad Sci U S A 1997; 94: 8795-8800.

[120] Muro S, Gajewski C, Koval M, Muzykantov VR. ICAM-1 recycling in endothelial cells: a novel pathway for sustained intracellular delivery and prolonged effects of drugs. Blood 2005; 105: 650-658.

[121] Rafat M, Heller M, Rabinov J, Stone H, Auguste D. Hemodynamic Transitions Defined by Saccular Aneurysm Geometry and Reynolds Number. Biophys J 2010; Submitted.

[122] Sampath R, Kukielka GL, Smith CW, Eskin SG, McIntire LV. Shear stress-mediated changes in the expression of leukocyte adhesion receptors on human umbilical vein endothelial cells in vitro. Ann Biomed Eng 1995; 23: 247-256.

[123] Thoumine O, Nerem RM, Girard PR. Changes in organization and composition of the extracellular matrix underlying cultured endothelial cells exposed to laminar steady shear stress. Lab Invest 1995; 73: 565-576.

[124] Gibbons GH, Dzau VJ. The emerging concept of vascular remodeling. N Engl J Med 1994; 330: 1431-1438.

[125] Kim SC, Singh M, Huang J, Prestigiacomo CJ, Winfree CJ, Solomon RA, Connolly ES, Jr. Matrix metalloproteinase-9 in cerebral aneurysms. Neurosurgery 1997; 41: 642-666; discussion 646-647.

[126] Yin WH, Chen JW, Young MS, Lin SJ. Increased endothelial monocyte adhesiveness is related to clinical outcomes in chronic heart failure. Int J Cardiol 2007; 121: 276-283.

[127] VandenBerg E, Reid MD, Edwards JD, Davis HW. The role of the cytoskeleton in cellular adhesion molecule expression in tumor necrosis factor-stimulated endothelial cells. J Cell Biochem 2004; 91: 926-937.

[128] Larsen CG, Anderson AO, Oppenheim JJ, Matsushima K. Production of interleukin-8 by human dermal fibroblasts and keratinocytes in response to interleukin-1 or tumour necrosis factor. Immunology 1989; 68: 31-36.

[129] Kim HJ, Park KG, Yoo EK, Kim YH, Kim YN, Kim HS, Kim HT, Park JY, Lee KU, Jang WG, Kim JG, Kim BW, Lee IK. Effects of PGC-1alpha on TNF-alpha-induced MCP-1 and VCAM-1 expression and NF-kappaB activation in human aortic smooth muscle and endothelial cells. Antioxid Redox Signal 2007; 9: 301-307.

[130] Chien S. Molecular and mechanical bases of focal lipid accumulation in arterial wall. Prog Biophys Mol Biol 2003; 83: 131-151.

[131] Hashimoto T, Meng H, Young WL. Intracranial aneurysms: links among inflammation, hemodynamics and vascular remodeling. Neurol Res 2006; 28: 372-380.

[132] Kataoka K, Taneda M, Asai T, Kinoshita A, Ito M, Kuroda R. Structural fragility and inflammatory response of ruptured cerebral aneurysms. A comparative study between ruptured and unruptured cerebral aneurysms. Stroke; a journal of cerebral circulation 1999; 30: 1396-1401.

[133] Bruno G, Todor R, Lewis I, Chyatte D. Vascular extracellular matrix remodeling in cerebral aneurysms. J Neurosurg 1998; 89: 431-440.

[134] Polin RS, Bavbek M, Shaffrey ME, Billups K, Bogaev CA, Kassell NF, Lee KS. Detection of soluble E-selectin, ICAM-1, VCAM-1, and L-selectin in the cerebrospinal fluid of patients after subarachnoid hemorrhage. J Neurosurg 1998; 89: 559-567.

[135] Aoki T, Kataoka H, Ishibashi R, Nozaki K, Morishita R, Hashimoto N. Reduced collagen biosynthesis is the hallmark of cerebral aneurysm: contribution of interleukin-1beta and nuclear factor-kappaB. Arterioscler Thromb Vasc Biol 2009; 29: 1080-1086.

[136] Smith RR, Clower BR, Grotendorst GM, Yabuno N, Cruse JM. Arterial wall changes in early human vasospasm. Neurosurgery 1985; 16: 171-176.

[137] Newell DW, Eskridge JM, Mayberg MR, Grady MS, Winn HR. Angioplasty for the treatment of symptomatic vasospasm following subarachnoid hemorrhage. J Neurosurg 1989; 71: 654-660.

[138] Chien S. Mechanotransduction and endothelial cell homeostasis: the wisdom of the cell. Am J Physiol Heart Circ Physiol 2007; 292: H1209-1224.

[139] Liu Y, Chen BP, Lu M, Zhu Y, Stemerman MB, Chien S, Shyy JY. Shear stress activation of SREBP1 in endothelial cells is mediated by integrins. Arterioscler Thromb Vasc Biol 2002; 22: 76-81.

[140] Futami K, Yamashita J, Tachibana O, Higashi S, Ikeda K, Yamashima T. Immunohistochemical alterations of fibronectin during the formation and proliferative repair of experimental cerebral aneurysms in rats. Stroke 1995; 26: 1659-1664.

[141] Patterson CE, Clauss M, Chapter 6 Signaling and prolonged endothelial activation, in Advances in Molecular and Cell Biology, E.P. Carolyn, Editor. 2005, Elsevier. p. 165-204.

[142] Petrache I, Birukova A, Ramirez SI, Garcia JG, Verin AD. The role of the microtubules in tumor necrosis factor-alpha-induced endothelial cell permeability. Am J Respir Cell Mol Biol 2003; 28: 574-581.

[143] Fearon WF, Fearon DT. Inflammation and cardiovascular disease: role of the interleukin-1 receptor antagonist. Circulation 2008; 117: 2577-2579.

[144] Ingber D, Mechanochemical Control of Cell Fate Switching. Principles of Tissue Engineering, ed. R.P. Lanza, R. Langer, and J. Vacanti. 2007, Burlington, MA: Elsevier Academic Press.

[145] Maheshwari G, Brown G, Lauffenburger DA, Wells A, Griffith LG. Cell adhesion and motility depend on nanoscale RGD clustering. J Cell Sci 2000; 113: 1677-1686.

[146] Pelham RJ, Jr., Wang Y. Cell locomotion and focal adhesions are regulated by substrate flexibility. Proc Natl Acad Sci U S A 1997; 94: 13661-13665.

[147] Schneider A, Francius G, Obeid R, Schwinte P, Hemmerle J, Frisch B, Schaaf P, Voegel JC, Senger B, Picart C. Polyelectrolyte multilayers with a tunable Young's modulus: influence of film stiffness on cell adhesion. Langmuir 2006; 22: 1193-1200.

[148] Thompson MT, Berg MC, Tobias IS, Rubner MF, Van Vliet KJ. Tuning compliance of nanoscale polyelectrolyte multilayers to modulate cell adhesion. Biomaterials 2005; 26: 6836-6845.

[149] Engler AJ, Sen S, Sweeney HL, Discher DE. Matrix elasticity directs stem cell lineage specification. Cell 2006; 126: 677-689.

[150] Walzog B, Gaehtgens P. Adhesion Molecules: The Path to a New Understanding of Acute Inflammation. News Physiol Sci 2000; 15: 107-113.

[151] Omolola Eniola A, Hammer DA. In vitro characterization of leukocyte mimetic for targeting therapeutics to the endothelium using two receptors. Biomaterials 2005; 26: 7136-7144.

[152] Myung JH, Launiere CA, Eddington DT, Hong S. Enhanced tumor cell isolation by a biomimetic combination of E-selectin and anti-EpCAM: implications for the effective separation of circulating tumor cells (CTCs). Langmuir 2010; 26: 8589-8596.

[153] Libby P, Ridker PM, Maseri A. Inflammation and atherosclerosis. Circulation 2002; 105: 1135-1143.

[154] Frijns CJ, Kappelle LJ. Inflammatory cell adhesion molecules in ischemic cerebrovascular disease. Stroke 2002; 33: 2115-2122.

[155] Sattar N, McCarey DW, Capell H, McInnes IB. Explaining how "high-grade" systemic inflammation accelerates vascular risk in rheumatoid arthritis. Circulation 2003; 108: 2957-2963.

[156] Schmedlen RH, Masters KS, West J. Photocrosslinkable polyvinyl alcohol hydrogels that can be modified with cell adhesion peptides for use in tissue engineering. Biomaterials 2002; 23: 4325-4332.

[157] Bryant S, Davis-Arehart K, Luo N, Shoemaker R, Arthur J, Anseth K. Synthesis and Characterization of Photopolymerized Multifunctional Hydrogels: Water-Soluble Poly(Vinyl Alcohol) and Chondroitin Sulfate Macromers for Chondrocyte Encapsulation. Macromolecules 2004; 37: 6726-6733.

[158] Sanjust E, Cocco D, Curreli N, Rescigno A, Solliai F, Bannister J. Flavin-Grafted Poly(vinyl alcohol): Preparation and Properties. J Appl Polym Sci 2002; 85: 2471-2477.

[159] Maraldo D, Mutharasan R. Optimization of antibody immobilization for sensing using piezoelectrically excited-millimeter-sized cantilever (PEMC) sensors. Sensor Actuat B 2007; 123: 474-479.

[160] Hermanson G, Bioconjugate Techniques. 1996, San Diego, CA: Academic Press.

[161] Dhoot NO, Tobias CA, Fischer I, Wheatley MA. Peptide-modified alginate surfaces as a growth permissive substrate for neurite outgrowth. J Biomed Mater Res A 2004; 71: 191-200.

[162] Chu L, Tempelman L, Miller C, Hammer D. Centrifugation Assay of IgE-Mediated Cell Adhesion to Antigen-Coated Gels. AIChE Journal 1994; 40: 692-703.

[163] Harbers GM, Gamble LJ, Irwin EF, Castner DG, Healy KE. Development and characterization of a high-throughput system for assessing cell-surface receptor-ligand engagement. Langmuir 2005; 21: 8374-8384.

[164] McClay DR, Wessel GM, Marchase RB. Intercellular recognition: quantitation of initial binding events. Proc Natl Acad Sci U S A 1981; 78: 4975-4979.

[165] Burridge K, Turner CE, Romer LH. Tyrosine phosphorylation of paxillin and pp125FAK accompanies cell adhesion to extracellular matrix: a role in cytoskeletal assembly. J Cell Biol 1992; 119: 893-903.

[166] Kiely JM, Hu Y, Garcia-Cardena G, Gimbrone MA, Jr. Lipid raft localization of cell surface E-selectin is required for ligation-induced activation of phospholipase C gamma. J Immunol 2003; 171: 3216-3224.

[167] Giancotti FG, Ruoslahti E. Integrin signaling. Science 1999; 285: 1028-1032.

[168] van Wetering S, van den Berk N, van Buul JD, Mul FP, Lommerse I, Mous R, ten Klooster JP, Zwaginga JJ, Hordijk PL. VCAM-1-mediated Rac signaling controls endothelial cell-cell contacts and leukocyte transmigration. Am J Physiol Cell Physiol 2003; 285: C343-352.

[169] Hu Y, Szente B, Kiely JM, Gimbrone MA, Jr. Molecular events in transmembrane signaling via E-selectin. SHP2 association, adaptor protein complex formation and ERK1/2 activation. J Biol Chem 2001; 276: 48549-48553.

[170] Parsons JT. Focal adhesion kinase: the first ten years. J Cell Sci 2003; 116: 1409-1416.

[171] Zhang X, Kinnick RR, Fatemi M, Greenleaf JF. Noninvasive Method for Estimation of Complex Elastic Modulus of Arterial Vessels. IEEE Transactions on Ultrasonics, Ferroelectrics, and Frequency Control 2005; 52: 642-652.

[172] Armstrong CG, Mow VC. Variations in the intrinsic mechanical properties of human articular cartilage with age, degeneration, and water content. J Bone Joint Surg Am 1982; 64: 88-94.

[173] Borene ML, Barocas VH, Hubel A. Mechanical and cellular changes during compaction of a collagen-sponge-based corneal stromal equivalent. Ann Biomed Eng 2004; 32: 274-283.

[174] Boontheekul T, Hill EE, Kong HJ, Mooney DJ. Regulating myoblast phenotype through controlled gel stiffness and degradation. Tissue Eng 2007; 13: 1431-1442.

[175] You JO, Rafat M, Ye GJ, Auguste DT. Nanoengineering the heart: conductive scaffolds enhance connexin 43 expression. Nano Lett 2011; 11: 3643-3648.

[176] Martens P, Anseth KS. Characterization of hydrogels formed from acrylate modified poly(vinyl alcohol) macromers. Polymer 2000; 41: 7715-7722.

[177] Xiao Y, Truskey GA. Effect of receptor-ligand affinity on the strength of endothelial cell adhesion. Biophys J 1996; 71: 2869-2884.

[178] Steiner B, Cousot D, Trzeciak A, Gillessen D, Hadvary P. Ca2+-dependent binding of a synthetic Arg-Gly-Asp (RGD) peptide to a single site on the purified platelet glycoprotein IIb-IIIa complex. J Biol Chem 1989; 264: 13102-13108.

[179] Friguet B, Chaffotte AF, Djavadi-Ohaniance L, Goldberg ME. Measurements of the true affinity constant in solution of antigen-antibody complexes by enzyme-linked immunosorbent assay. J Immunol Methods 1985; 77: 305-319.

[180] Bader RA, Rochefort WE. Rheological characterization of photopolymerized poly(vinyl alcohol) hydrogels for potential use in nucleus pulposus replacement. J Biomed Mater Res A 2008; 86: 494-501.

[181] Becker TA, Kipke DR, Brandon T. Calcium alginate gel: a biocompatible and mechanically stable polymer for endovascular embolization. J Biomed Mater Res 2001; 54: 76-86.

[182] Becker TA, Preul MC, Bichard WD, Kipke DR, McDougall CG. Preliminary investigation of calcium alginate gel as a biocompatible material for endovascular aneurysm embolization in vivo. Neurosurgery 2007; 60: 1119-1127; discussion 1127-1118.

[183] Rafat M, Rotenstein L, You JO, Auguste DT. Dual functionalized PVA hydrogels mimic cooperative adhesion between leukocytes and endothelial cells. Biomaterials 2012; 33: 3880-3886.

[184] Garcia AJ. Get a grip: integrins in cell-biomaterial interactions. Biomaterials 2005; 26: 7525-7529.

[185] Langer R, Tirrell DA. Designing materials for biology and medicine. Nature 2004; 428: 487-492.

[186] Park YD, Tirelli N, Hubbell JA. Photopolymerized hyaluronic acid-based hydrogels and interpenetrating networks. Biomaterials 2003; 24: 893-900.

[187] Tzima E, Irani-Tehrani M, Kiosses WB, Dejana E, Schultz DA, Engelhardt B, Cao G, DeLisser H, Schwartz MA. A mechanosensory complex that mediates the endothelial cell response to fluid shear stress. Nature 2005; 437: 426-431.

[188] Pober JS, Bevilacqua MP, Mendrick DL, Lapierre LA, Fiers W, Gimbrone MA, Jr. Two distinct monokines, interleukin 1 and tumor necrosis factor, each independently induce biosynthesis and transient expression of the same antigen on the surface of cultured human vascular endothelial cells. Journal of Immunology 1986; 136: 1680-1687.

[189] Zhu C, Bao G, Wang N. Cell mechanics: Mechanical response, cell adhesion, and molecular deformation. Annual Review of Biomedical Engineering 2000; 2: 189-226.

[190] Davies MJ, Gordon JL, Gearing AJ, Pigott R, Woolf N, Katz D, Kyriakopoulos A. The expression of the adhesion molecules ICAM-1, VCAM-1, PECAM, and E-selectin in human atherosclerosis. J Pathol 1993; 171: 223-229.

[191] Ross R. Atherosclerosis--an inflammatory disease. N Engl J Med 1999; 340: 115-126.

[192] Drury JL, Dennis RG, Mooney DJ. The tensile properties of alginate hydrogels. Biomaterials 2004; 25: 3187-3199.

[193] Wagner CR, Mailenberg GE, eds. Handbook of X-ray Photoelectron Spectroscopy. 1979, Perkin-Elmer Corp.: Edenprairie, MN.

[194] Willemsen OH, Snel MM, van der Werf KO, de Grooth BG, Greve J, Hinterdorfer P, Gruber HJ, Schindler H, van Kooyk Y, Figdor CG. Simultaneous height and adhesion imaging of antibody-antigen interactions by atomic force microscopy. Biophys J 1998; 75: 2220-2228.

[195] Gallant ND, Michael KE, Garcia AJ. Cell adhesion strengthening: contributions of adhesive area, integrin binding, and focal adhesion assembly. Mol Biol Cell 2005; 16: 4329-4340.

[196] Boettiger D. Quantitative measurements of integrin-mediated adhesion to extracellular matrix. Methods Enzymol 2007; 426: 1-25.

[197] Lotz MM, Burdsal CA, Erickson HP, McClay DR. Cell adhesion to fibronectin and tenascin: quantitative measurements of initial binding and subsequent strengthening response. J Cell Biol 1989; 109: 1795-1805.

[198] Charo IF, Yuen C, Goldstein IM. Adherence of human polymorphonuclear leukocytes to endothelial monolayers: effects of temperature, divalent cations, and chemotactic factors on the strength of adherence measured with a new centrifugation assay. Blood 1985; 65: 473-479.

[199] Rafat M, Rotenstein L, Hu J, Auguste DT. Engineered endothelial cell adhesion via VCAM1 and E-selectin antibody-presenting alginate hydrogels. Acta Biomaterialia 2012; In Press.

[200] Fyta M, Melchionna S, Succi S, Kaxiras E. Hydrodynamic correlations in the translocation of a biopolymer through a nanopore: theory and multiscale simulations. Phys Rev E Stat Nonlin Soft Matter Phys 2008; 78: 036704.

[201] Peters A, Melchionna S, Kaxiras E, Latt J, Sircar J, Bernaschi M, Bisson M, Succi S. Multiscale simulation of cardiovascular flows on the IBM Blue Gene/P: full heart-circulation system at near red-blood cell resolution. 2010 ACM/IEEE International Conference for High Performance Computing, Networking, Storage and Analysis 2010; 1-10.

[202] Rybicki FJ, Melchionna S, Mitsouras D, Coskun AU, Whitmore AG, Steigner M, Nallamshetty L, Welt FG, Bernaschi M, Borkin M, Sircar J, Kaxiras E, Succi S, Stone PH, Feldman CL. Prediction of coronary artery plaque progression and potential rupture from 320-detector row prospectively ECG-gated single heart beat CT angiography: Lattice Boltzmann evaluation of endothelial shear stress. Int J Cardiovasc Imaging 2009; 25: 289-299.

[203] Ahrenholz B, Massively parallel simulations of multiphase- and multicomponent flows using lattice Boltzmann methods, in Braunschweig. 2009, University of Braunschweig - Institute of Technology: Germany.

[204] Jordan O, Doelker E, Rufenacht DA. Biomaterials used in injectable implants (liquid embolics) for percutaneous filling of vascular spaces. Cardiovasc Intervent Radiol 2005; 28: 561-569.

[205] Mawad D, Poole-Warren LA, Martens P, Koole LH, Slots TL, van Hooy-Corstjens CS. Synthesis and characterization of radiopaque iodine-containing degradable PVA hydrogels. Biomacromolecules 2008; 9: 263-268.

[206] Whitesides GM, Ostuni E, Takayama S, Jiang X, Ingber DE. Soft lithography in biology and biochemistry. Annu Rev Biomed Eng 2001; 3: 335-373.

[207] Weibel DB, Diluzio WR, Whitesides GM. Microfabrication meets microbiology. Nat Rev Microbiol 2007; 5: 209-218.

8 APPENDICES

8.1 Appendix A: List of Publications

1. **Rafat M**, Rotenstein L, Hu J, Auguste DT. Engineered endothelial cell adhesion via VCAM1 and E-selectin antibody-presenting alginate hydrogels. *Acta Biomaterialia*. In Press.
2. **Rafat M**, Rotenstein L, You JO, Auguste DT. Dual functionalized PVA hydrogels that adhere endothelial cells synergistically. *Biomaterials*. 2012; 33(15): 3880-3886.

8.2 Appendix B: Supplement to Computational Studies

MATLAB Code Used for COMSOL Simulations

```
%Marjan Rafat with assistance from Martin Heller

%Aneurysm Streamline Analysis

%1 December 2007

flclear fem

clear


% Constants

fem.const.rho = 1060;     % density of fluid [kg/m^3]

fem.const.eta = 3e-3;  % viscosity of fluid [Ns/m^2]


fem.expr = { ...

    'sigmaxx','-p+2*eta*ux' ...

    'sigmaxy','eta*(uy+vx)' ...

    'sigmayx','eta*(vx+uy)', ...

    'sigmayy','-p+2*eta*vy'};


%Geometry and mesh

% Find the boundary groups

c = geomdel(rect2(0.03,0.004)+rect2(0.003,0.03,'pos', [0.03;-
0.013])+ellip2(0.001,0.0005,'pos',[0.033;.002]));

s.objs={c};

s.name={'channel'};

fem.draw = struct('s',s);

[g,ctx] = geomcsg(fem, ...

    'Ns',{'c'}, ...

    'Sf','c', ...
```

```
    'Out',{'g','ctx'});
fem.geom = g;
fem.mesh = meshinit(fem,'hauto',1,'hnarrow',4,'report','off');
%plot geometry
figure;
geomplot(fem, 'edgelabels', 'on', 'pointmode','off');


% find boundary numbers
[i,j] = find(ctx{1});
inlet = i(find(j==1));
outlet = i(find(j==5|j==7));
noslip = i(find(j==2|j==3|j==4|j==6|j==8|j==9|j==10|j==11));
clear c s g ctx i j


fem.sdim = {{'x','y'}};
% u, v, p, lm3, lm4
fem.shape=[2 2 1 2 2];


% Equations
fem.form = 'weak';
fem.equ.dim = {'u','v','p'};
fem.equ.init = {{0;0;0}};
fem.equ.shape = [1;2;3];
fem.equ.dweak = {{'rho*ut*test(u)';'rho*vt*test(v)';0}};
fem.equ.weak = {{'-sigmaxx*test(ux)-sigmaxy*test(uy)-
rho*(u*ux+v*uy)*test(u)'; ...
                 '-sigmayx*test(vx)-sigmayy*test(vy)-
rho*(u*vx+v*vy)*test(v)'; ...
                 '-(ux+vy)*test(p)'}};
```

```
% Boundary conditions
% Boundary group 1 = inlet
% Boundary group 2 = no slip along the walls
% Boundary group 3 = outlet
fem.bnd.ind = {[inlet] [noslip] [outlet]};
fem.bnd.dim = {'u','v','p','lm3','lm4'};
fem.bnd.init = {{'0';'0';'0';'0';'0'}};
fem.bnd.shape = {[1;2;4;5], ...
                 [1;2;3;4;5],...
                 [1;2;4]};
fem.bnd.weak = {...
    {0;0;0;'-lm3_test*(4*s*(1-s)*0.7-u)+u_test*lm3';'lm4_test*v+v_test*lm4'},
...
    {0;0;0;'lm3_test*u+u_test*lm3';'lm4_test*v+v_test*lm4'},...
    {0;0;0;'lm3_test*u+u_test*lm3';0}};

% Create an extended meshstructure
fem.xmesh = meshextend(fem);
fem.sol = asseminit(fem);

% Solve
fem.sol = femtime(fem, ...
    'init',fem.sol, ...
    'tlist',linspace(0,1,11), ...
    'tout','tlist', ...
    'estrat',1);
```

```
%Plot Pressure profile, streamlines

figure;

postplot(fem, 'tridata', 'p', ...

         'trimap','jet(1024)', ...

         'arrowdata', {'u', 'v'}, ...

         'title', 'Surface: Pressure; Arrow: Velocity Field');


postplot(fem, ...

         'flowdata',{'u','v'}, ...

         'flowcolor',[1.0,0.0,0.0], ...

         'flowstart',{[zeros(1,20),.033*ones(1,10),
.0334*ones(1,10),.0336*ones(1,10),.0338*ones(1,10),
.034*ones(1,10),.0345*ones(1,10),
.035*ones(1,10),.0355*ones(1,10),.0365*ones(1,10),.037*ones(1,10)],...


[linspace(0,.004,20),linspace(.0015,.0025,10),linspace(.0015,.0025,10),linspa
ce(.0015,.0025,10),linspace(.0015,.0025,10),linspace(.0015,.0025,10),linspace
(.0015,.0025,10),linspace(.0015,.0025,10),
linspace(.0015,.0025,10),linspace(.0015,.0025,10),linspace(.0015,.0025,10)]},
...

         'title','Streamline: Velocity field [m/s]');
```

MATLAB Code for Determining Shear Stress

```
%aneurysm stream function

flclear fem

clear

close all


% Constants

fem.const.rho = 1060;     % density of fluid

fem.const.eta = 3e-3;  % viscosity of fluid

L = 0.03; W = 0.004;

h = 0.003; l = 0.015;

a = 0.006; b = 0.003;


fem.expr = { ...

    'sigmaxx','-p+2*eta*ux', ...

    'sigmaxy','eta*(uy+vx)', ...

    'sigmayx','eta*(vx+uy)', ...

    'sigmayy','-p+2*eta*vy', ...

    'Q','0.004*2/3*umax'};


%Geometry and mesh

e = ellip2(a,b,'pos',[L+h;0.002])-rect2(a,2*b,'pos',[L+h-
a/2;0.002],'base','center');

%e = ellip2(a,b,'pos',[L+h+0.00075;0.002])-rect2(0.009,0.006,'pos',[0.024,-
0.001],'base','corner');

r1 = rect2(L,W,'pos',[0;0],'base','corner');

r2 = rect2(h,l,'pos',[L; 0.002],'base','corner');

r3 = rect2(h,l,'pos',[L;-0.013],'base','corner');

s.objs={e,r1,r2,r3};
```

```
s.name={'aneurysm','channel1','channel2','channel3'};
fem.draw = struct('s',s);
[g,ctx,ptx] = geomcsg(fem, ...
    'Ns',{'e','r1','r2','r3'}, ...
    'Sf','e+r1+r2+r3', ...
    'Out',{'g','ctx','ptx'}, ...
    'edge','all');
fem.geom = g;
figure;
geomplot(fem, 'edgelabels', 'on', 'pointmode','off');

% the boundaries on the ellipse
[i,j]    = find(ctx{1});
aneurysm = i(find(j==2|j==3))';
%aneurysm = i(find(j==2|j==3|j==4|j==5))';

% the boundaries on channel1
[i,j]   = find(ctx{2});
inlet   = i(find(j==4));
up      = i(find(j==3));
down    = i(find(j==1));

% the boundaries on channel2
[i,j]   = find(ctx{3});
outlet2 = i(find(j==3));
right2  = i(find(j==2));
left2   = i(find(j==4));
```

```
% the boundaries on channel3
[i,j]   = find(ctx{4});
outlet3 = i(find(j==1));
right3  = i(find(j==2));
left3   = i(find(j==4));

% round corners near aneurysm
% node points of corners
% [i,j]   = find(ptx{1});
% corners = i(find(j==1|j==2));
% [g2,ctx] = fillet(g,'point',[corners],'radii',0.1*a,'out',{'ctx'});
% fem.geom = g2;
%
% [i,j]   = find(ctx{1});
% idx = i(find(j==aneurysm(1)|j==aneurysm(2)))';
% aneurysm = [aneurysm,idx];
inlet   = inlet;
outlet  = [outlet2,outlet3];
noslip1 = [down,left3];
noslip2 = [up,left2];
noslip3 = [aneurysm,right2,right3];


fem.mesh = meshinit(fem, ...
    'hauto',1, ...
    'hnarrow',4, ...
    'report','off', ...
```

```
    'hmaxedg',[aneurysm; repmat(5e-5,size(aneurysm))]);
% meshplot(fem)
% return
clear c s g ctx i j %g2

fem.sdim = {{'x','y'}};
fem.dim = {'u','v','p', 'psi','lm1','lm2'};
fem.shape=[2 2 1 2 2 2];

% Equations
fem.form = 'general';
fem.equ.dim = {'u','v','p','psi'};
fem.equ.init = {{0;0;0;0}};
fem.equ.shape = [1;2;3;4];

% da * ut = nabla . Ga + f
fem.form = 'general';
fem.equ.da = {{{'-rho'} ...
               {'-rho'} ...
               {'0'} ...
               {'0'}}};
fem.equ.ga = {{{'sigmaxx' 'sigmaxy'} ...
               {'sigmayx' 'sigmayy'} ...
               {'0' '0'} ...
               {'psix' 'psiy'}}};
fem.equ.f = {{{'rho*(u*ux+v*uy)'} ...
              {'rho*(u*vx+v*vy)'} ...
              {'ux+vy'} ...
```

```
              {'-(vx-uy)'}}};
fem.bnd.expr = {'K_x_ns','eta*(2*nx*ux+ny*(uy+vx))', ...
                'K_y_ns','eta*(nx*(vx+uy)+2*ny*vy)', ...
                'T_x_ns','nx*sigmaxx+ny*sigmaxy', ...
                'T_y_ns','nx*sigmayx+ny*sigmayy'};

% Boundary conditions
fem.bnd.ind = {[inlet] [noslip1] [noslip2] [noslip3] [outlet]};
fem.bnd.dim = {'u','v','p','psi','lm1','lm2'};
fem.bnd.init = {{'0';'0';'0';'0';'0';'0'}};
fem.bnd.shape = {[1:6] [1:6] [1:6] [1:6] [1:5]};
fem.bnd.weak = {{'lm1_test*(u-4*s*(1-s)*umax)+u_test*lm1'
'lm2_test*v+v_test*lm2'} ...
                {'lm1_test*u+u_test*lm1' 'lm2_test*v+v_test*lm2'} ...
                {'lm1_test*u+u_test*lm1' 'lm2_test*v+v_test*lm2'} ...
                {'lm1_test*u+u_test*lm1' 'lm2_test*v+v_test*lm2'} ...
                {'lm1_test*u+u_test*lm1'}};
fem.bnd.constr = {0 {'psi'} 0 0 0};

fem = flform(fem,'outform','weak');

fem.xmesh = meshextend(fem);
fem.sol = asseminit(fem);

% solve for different max-velocities
fem.sol = femnlin(fem, ...
    'pname','umax', ...
    'plist',[.7]);
```

```
figure;
postcrossplot(fem,1,[aneurysm], ...
              'lindata','K_x_ns*(tx)+K_y_ns*(ty)', ...
              'title','Wall Shear Stress Profile', ...
              'axislabel',{'Arc-length','Wall Shear Stress (N/m^2)'}, ...
              'refine','auto','solnum',1,'linlegend','off');
% figure;
% postcrossplot(fem,1,[aneurysm], ...
%               'lindata','K_x_ns*(tx)+K_y_ns*(ty)', ...
%               'title','Wall Shear Stress Profile', ...
%               'axislabel',{'Arc-length','Wall Shear Stress (N/m^2)'}, ...
%               'refine','auto','solnum',2,'linlegend','off');
% figure;
% postcrossplot(fem,1,[aneurysm], ...
%               'lindata','K_x_ns*(tx)+K_y_ns*(ty)', ...
%               'title','Wall Shear Stress Profile', ...
%               'axislabel',{'Arc-length','Wall Shear Stress (N/m^2)'}, ...
%               'refine','auto','solnum',3,'linlegend','off');
figure;
postplot(fem, ...
        'flowdata',{'u';'v'}, ...
        'flowcolor',[0.2,0.2,0.2],...

'flowstart',{[repmat(0.033,1,21),linspace(0,a,21)+0.033,linspace(0,a,21)+0.03
3]; ...

[linspace(0,0.004,21),zeros(1,21)+0.1*b+0.002,zeros(1,21)-0.1*b+0.002]}, ...
        'axis',[0.03+0.5*0.003 0.033+1.05*a -0.002 0.006],'solnum',1);
% figure;
```

```
% postplot(fem, ...
%         'flowdata',{'u';'v'}, ...
%         'flowcolor',[0.2,0.2,0.2],...
%
'flowstart',{[repmat(.033,1,21),linspace(0,a,21)+.033,linspace(0,a,21)+.033];
...
%
[linspace(0,.004,21),zeros(1,21)+0.1*b+.002,zeros(1,21)-0.1*b+.002]}, ...
%         'axis',[.03+0.5*.003 .033+1.05*a -.002 .006],'solnum',2);
% figure;
% postplot(fem, ...
%         'flowdata',{'u';'v'}, ...
%         'flowcolor',[0.2,0.2,0.2],...
%
'flowstart',{[repmat(.033,1,21),linspace(0,a,21)+.033,linspace(0,a,21)+.033];
...
%
[linspace(0,.004,21),zeros(1,21)+0.1*b+.002,zeros(1,21)-0.1*b+.002]}, ...
%         'axis',[.03+0.5*.003 .033+1.05*a -.002 .006],'solnum',3);
% figure;
% postcrossplot(fem,1,[aneurysm], ...
%               'lindata','K_x_ns*(tx)+K_y_ns*(ty)', ...
%               'title','Wall Shear Stress Profile', ...
%               'axislabel',{'Arc-length','Wall Shear Stress (N/m^2)'}, ...
%               'refine','auto','solnum','end','linlegend','off');
% figure;
% postcrossplot(fem,1,[noslip3], ...
%               'lindata','K_x_ns*(tx)+K_y_ns*(ty)', ...
%               'title','Wall Shear Stress Profile (tx,ty)', ...
%               'axislabel',{'Arc-length','Wall Shear Stress (N/m^2)'}, ...
%               'refine','auto','solnum','all','linlegend','on');
```

```
% figure;
% postcrossplot(fem,1,[noslip3], ...
%               'lindata','K_x_ns*(-ny)+K_y_ns*(nx)', ...
%               'title','Wall Shear Stress Profile (-ny,nx)', ...
%               'axislabel',{'Arc-length','Wall Shear Stress (N/m^2)'}, ...
%               'refine','auto','solnum','all','linlegend','on');
%{
figure;
postcrossplot(fem,1,[aneurysm], ...
              'lindata','T_x_ns', ...
              'title','Total stress x-direction', ...
              'axislabel',{'Arc-length','x-Stress (N/m^2)'}, ...
              'refine','auto','solnum','all','linlegend','on');

figure;
postcrossplot(fem,1,[aneurysm], ...
              'lindata','T_y_ns', ...
              'title','Total stress y-direction', ...
              'axislabel',{'Arc-length','y-Stress (N/m^2)'}, ...
              'refine','auto','solnum','all','linlegend','on');

figure;
postcrossplot(fem,1,[aneurysm], ...
              'lindata','-lm1', ...
              'title','Total stress x-direction (lagrange multiplier)', ...
              'axislabel',{'Arc-length','x-Stress (N/m^2)'}, ...
              'refine','auto','solnum','all','linlegend','on');
figure;
```

```
postcrossplot(fem,1,[aneurysm], ...
              'lindata','-lm2', ...
              'title','Total stress y-direction (lagrange multiplier)', ...
              'axislabel',{'Arc-length','y-Stress (N/m^2)'}, ...
              'refine','auto','solnum','all','linlegend','on');
figure;
postsurf(fem, ...
    'sqrt(u*u+v*v)', ...
    'contdata','psi', ...
    'contlevels',11, ...
    'contbar','off');
%}
%figure;
% fig = 0;
% for s = fem.sol.plist,
%     fig = fig + 1;
%     subplot(3,3,fig);
%     postplot(fem, ...
%         'flowdata',{'u';'v'}, ...
%
'flowstart',{[repmat(L+h,1,21),linspace(0,a,21)+L+h,linspace(0,a,21)+L+h];
...
%                       [linspace(-W/2,W/2,21),zeros(1,21)+0.1*b,zeros(1,21)-
0.1*b]}, ...
%         'axis',[L+0.5*h L+h+1.05*a -W W],'solnum',fig);
%     subplot(3,3,fig);
%     title(['u_{max} = ' num2str(s)]);
%     box on
% end
```

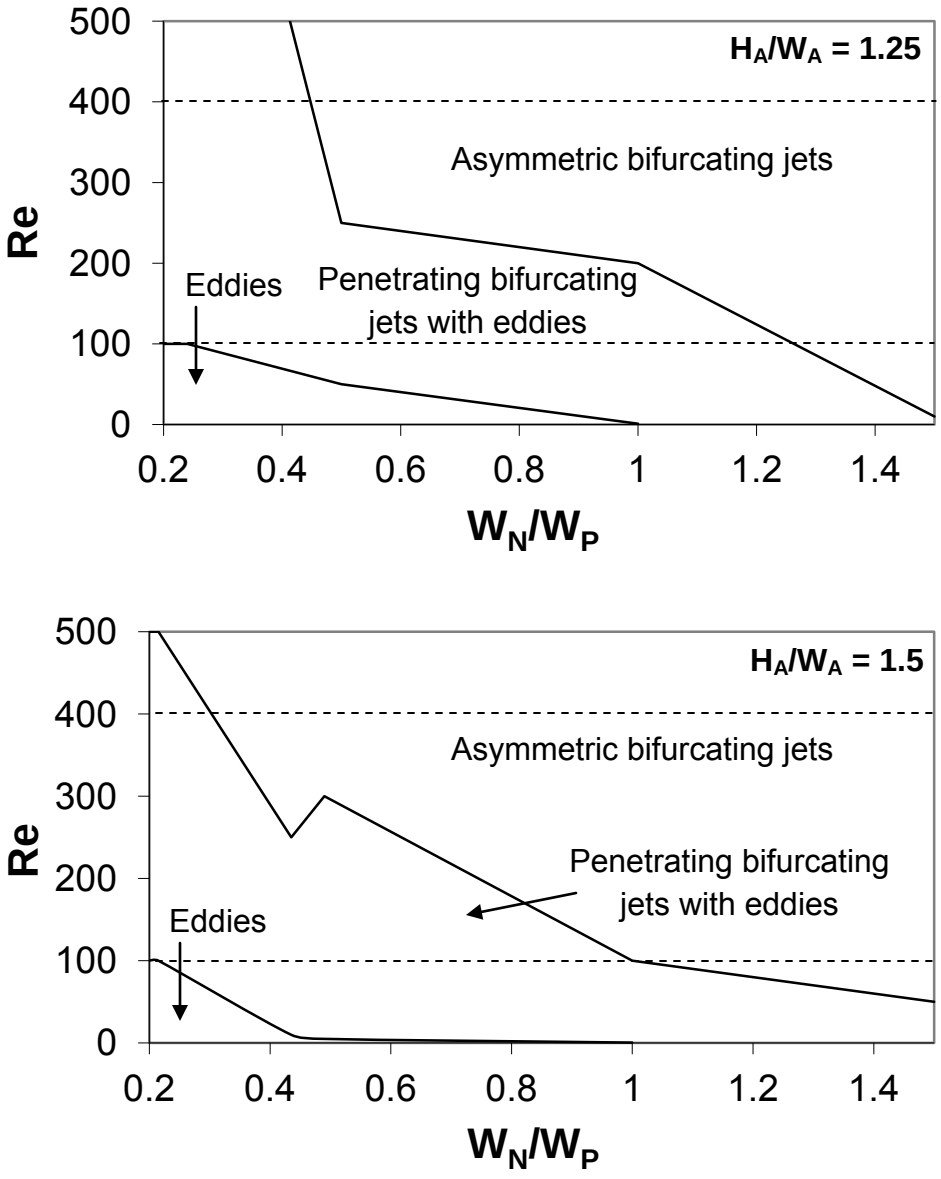

Figure 8.1: Additional mapping of flow patterns for symmetric aneurysms. Flow maps are shown in terms of various aneurysm height to width (H_A/W_A) ratios, Reynolds numbers (Re), and neck to parent width (W_N/W_P) ratios for symmetric aneurysms: (A) H_A/W_A=1.25 and (B) H_A/W_A=1.5. Dashed lines indicate physiological Re.

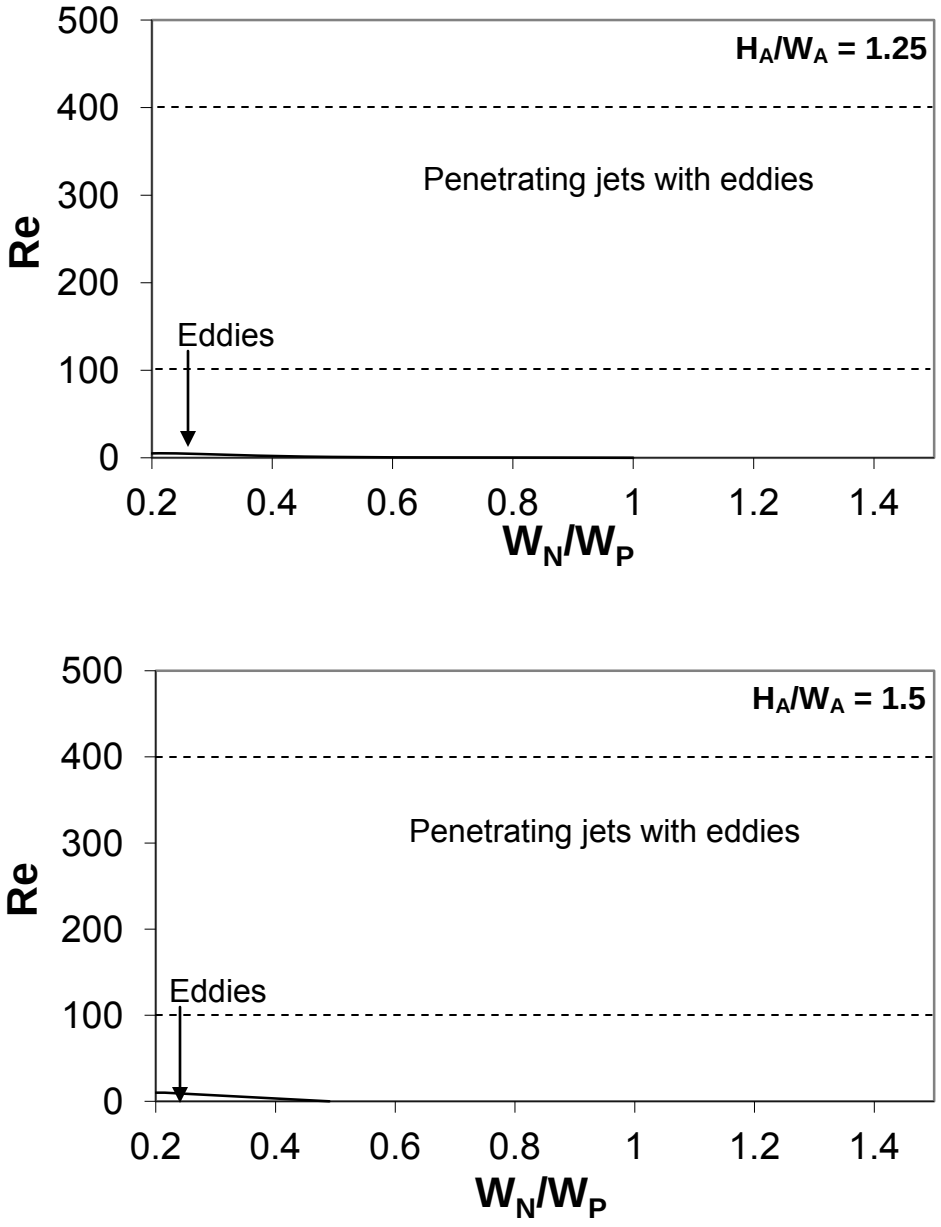

Figure 8.2: Additional mapping of flow patterns for offset aneurysms. Flow maps are shown in terms of various aneurysm height to width (H_A/W_A) ratios, Reynolds numbers (Re), and neck to parent width (W_N/W_P) ratios for offset aneurysms: (A) H_A/W_A=1.25 and (B) H_A/W_A=1.5. Dashed lines indicate physiological Re.

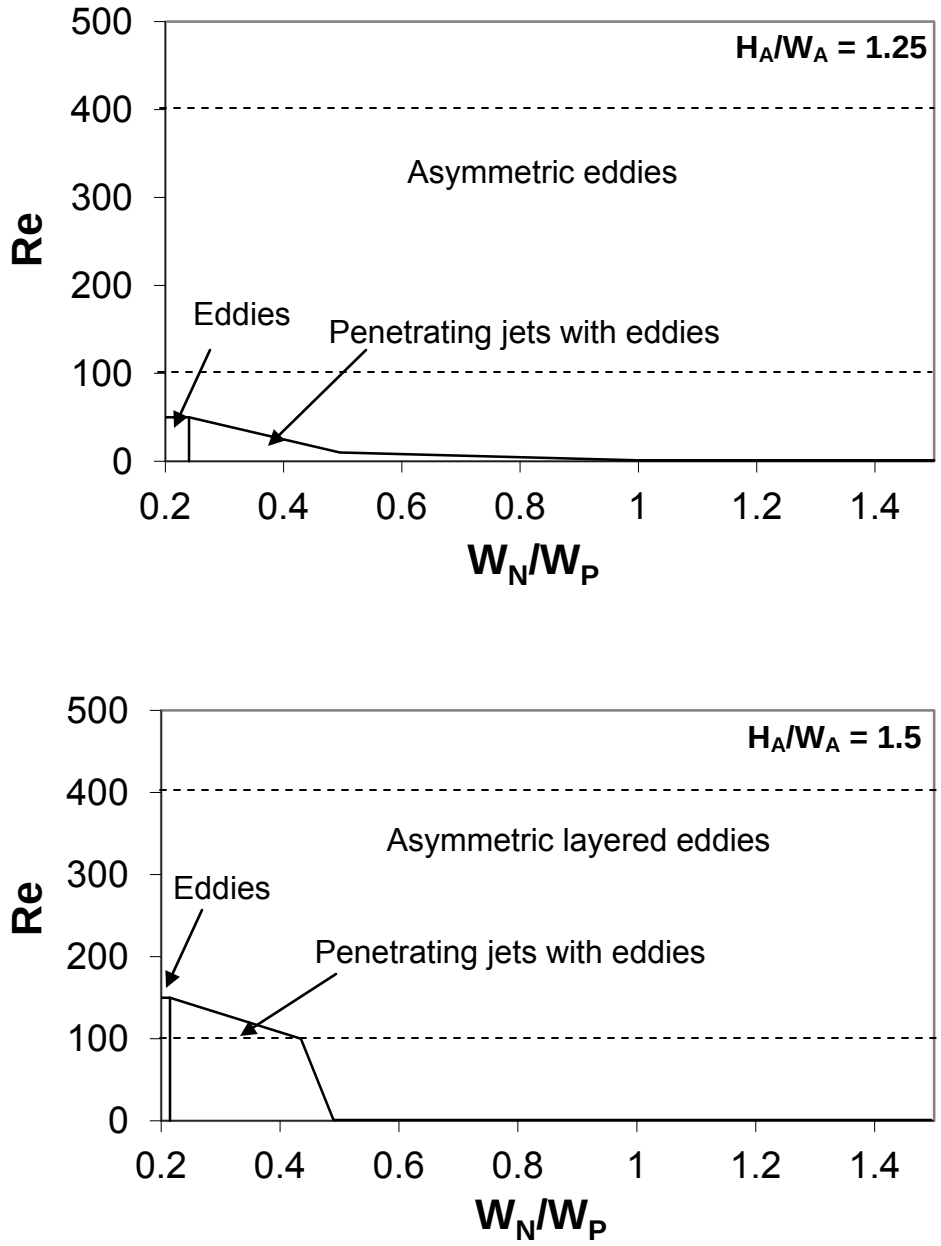

Figure 8.3: Additional mapping of flow patterns for sidewall aneurysms. Flow maps are shown in terms of various aneurysm height to width (H_A/W_A) ratios, Reynolds numbers (Re), and neck to parent width (W_N/W_P) ratios for sidewall aneurysms: (A) H_A/W_A=1.25 and (B) H_A/W_A=1.5. Dashed lines indicate physiological Re.